UNIVERSITÁ DEGLI STUDI DI MODENA E REGGIO EMILIA

Dipartimento di Scienze Fisiche, Informatiche e Matematiche
School of Graduate Studies in Physics and Nanosciences

TESI PER IL CONSEGUIMENTO DEL TITOLO DI DOTTORE DI RICERCA

Cerium and niobium oxides for ultrafast dynamic studies of photoexcited states

Supervisor:
Dr. Paola Luches

Submitted by:
Samuele Pelatti

Co-supervisors:
Dr. Stefania Benedetti,
Prof. Sergio D'Addato

PhD Program Coordinator:
Prof. Marco Affronte

Academic Year 2023/2024

XXXVII ciclo

Abstract

The growing concern about the consequences of climate change is pushing the scientific community to look for alternative ways to produce energy that does not release huge amounts of greenhouse gasses into the atmosphere. Solar energy can be transformed into chemical energy through the use of some compounds, such as cerium oxide, which allow some reactions, such as the electrolysis of water, to be catalyzed using solar energy by photoelectrochemical processes. The reactions are catalyzed by the excited charges in the photocatalyst when it is illuminated by solar light. These charges have a lifetime of the order of hundreds of picoseconds in which they must be able to interact with the surrounding environment to make catalysis occur. It is therefore important to study the temporal evolution of the charges in order to understand the processes that lead to an effective functionality of photocatalysts. Studies of this kind require ultrafast techniques based on free electron lasers, in conjunction with ultrafast visible lasers, to study the evolution of the excited states on timescales from a few tens of femtosecond to hundreds of picoseconds. In the first part of this thesis, the growth and characterization of cerium oxide samples will be described, and the results obtained at the European XFEL in Hamburg, by means of pump-probe X-ray absorption and emission spectroscopy techniques are discussed. In the second part of this thesis, the procedures for the stabilization of niobium oxides in different stoichiometries, namely Nb_2O_5, NbO_2 and NbO, will be described. In particular, Nb_2O_5 is an interesting photocatalytic material, while NbO_2 presents a phase transition from semiconductor to metal at the critical temperature of 800°C, which can also be triggered using visible laser pulses. The samples were also measured by XAS spectroscopy at the European XFEL.

Sommario

La crescente preoccupazione per le conseguenze del cambiamento climatico sta spingendo la comunità scientifica a cercare modi alternativi per produrre energia che non rilascino enormi quantità di gas serra nell'atmosfera. L'energia solare può essere trasformata in energia chimica attraverso l'uso di alcuni composti, come l'ossido di cerio, che consentono di catalizzare alcune reazioni, come l'elettrolisi dell'acqua, utilizzando l'energia solare tramite processi fotoelettrochimici. Le reazioni sono catalizzate dalle cariche eccitate nel fotocatalizzatore quando viene illuminato dalla luce solare. Queste cariche hanno una durata di vita dell'ordine di centinaia di picosecondi in cui devono essere in grado di interagire con l'ambiente circostante per far avvenire la catalisi. È quindi importante studiare l'evoluzione temporale delle cariche per comprendere i processi che portano a un efficace funzionamento dei fotocatalizzatori. Studi di questo tipo richiedono tecniche ultraveloci basate su laser a elettroni liberi, in combinazione con laser visibili ultraveloci, per studiare l'evoluzione degli stati eccitati su scale temporali da poche decine di femtosecondi a centinaia di picosecondi. Nella prima parte di questa tesi, verranno descritti la crescita e la caratterizzazione di campioni di ossido di cerio e verranno discussi i risultati ottenuti presso l'European XFEL di Amburgo, mediante tecniche di spettroscopia di assorbimento ed emissione di raggi X pump-probe. Nella seconda parte di questa tesi, verranno descritte le procedure per la stabilizzazione di ossidi di niobio in diverse stechiometrie, ovvero Nb_2O_5, NbO_2 e NbO. In particolare, Nb_2O_5 è un interessante materiale fotocatalitico, mentre NbO_2 presenta una transizione di fase da semiconduttore a metallo alla temperatura critica di 800°C, che può essere attivata anche utilizzando impulsi laser visibili. I campioni sono stati inoltre misurati mediante spettroscopia XAS presso l'European XFEL.

Contents

1 State of the Art **9**
- 1.1 Water splitting . . . 9
  - 1.1.1 Materials for photocatalytic water splitting . . . 10
- 1.2 Cerium Oxide . . . 12
  - 1.2.1 Crystal Structure . . . 13
  - 1.2.2 Electronic structure . . . 14
  - 1.2.3 Tuning photocatalytic properties of CeO_2 with metals . . . 16
  - 1.2.4 Polarons in Cerium Oxide . . . 20
- 1.3 Niobium Oxide . . . 23
  - 1.3.1 NbO . . . 23
  - 1.3.2 NbO_2 . . . 24
  - 1.3.3 Nb_2O_5 . . . 25

2 Experimental Techniques **27**
- 2.1 Sputtering . . . 27
  - 2.1.1 Magnetron Sputtering . . . 29
- 2.2 SESAMo Laboratories . . . 33
- 2.3 Free Electron Laser . . . 35
  - 2.3.1 European XFEL . . . 37
- 2.4 Pump-probe ultrafast spectroscopy . . . 39
- 2.5 APE beamline at Elettra Synchrotron . . . 41
  - 2.5.1 Reaction cell for ambient pressure XAS . . . 41

3 Results **45**
- 3.1 Optimization of magnetron sputtering grown ceria films . . . 45
  - 3.1.1 XPS measurements . . . 46
  - 3.1.2 UV-Visible absorption measurements . . . 52
  - 3.1.3 X-ray Diffraction Measurements . . . 57
- 3.2 Ultrafast dynamics of photoexcitations in cerium oxide films . . . 57
  - 3.2.1 Pump-probe RXES . . . 59
  - 3.2.2 Pump-probe XANES . . . 61
  - 3.2.3 Pump-probe EXAFS . . . 63
- 3.3 Study of Cu-doped cerium oxide films in water and under light exposure 67
- 3.4 A procedure to obtain niobium oxide films with variable stoichiometry 73
  - 3.4.1 XPS measurements . . . 74
  - 3.4.2 XRD measurements . . . 75
  - 3.4.3 UV-Visible absorption spectroscopy . . . 76
  - 3.4.4 SEM images . . . 77
  - 3.4.5 XANES measurements at EuXFEL . . . 78

Conclusions **81**

Acknowledgements **85**

A Activity report **101**

B List of publications **103**

Chapter 1

State of the Art

1.1 Water splitting

The increasing concerns of global warming effects, the consequences of which become more extreme as time passes, urged the scientific community to look for viable alternatives to the use of fossil fuels in order to cut the emission of greenhouse gases (GHG).
The energy sector is the one which produces more greenhouse gases, with a 34% of the total GHG produced by human activity in 2021 [1, 2]. 80% of energy was produced by fossil fuel sources in 2019 (oil, coal and natural gas), which accounted almost all of the GHG produced in the energy sector [3, 4]. For these reasons, a lot of efforts have been concentrated in the past years in order to reduce the share of energy produced by fossil fuels and to produce electricity mostly by renewable energies and low carbon emission energy sources[5].
Between all renewable energy sources, solar energy by photovoltaics (PV) represents the most available one, not requiring to build dams on height differences in rivers as hydroelectric power, or the presence of continuous high-speed wind and the need to construct tall wind turbines as in the case of wind power. However PV, compared to other renewable energy sources is highly influenced by the weather condition and the night-day cycle, resulting in a low capacity factor of about 20%, where the capacity factor for a power source is the ratio between the actual electrical energy output and the theoretical maximum electrical energy obtainable over a period of time [6, 7]. This means that direct production of electricity from sunlight is not sufficiently stable to be used as the primary energy source for the future and it needs a complementary renewable source that can substitute PV when its energy output is low. A promising candidate is the generation of fuel by sunlight, which then can act as an energy storage medium, releasing energy when necessary. The fuel must not release GHG, so a lot of attention has been focused on water splitting photoelectrolysis, a reaction in which energy is used to break the bonds in the water molecule between O and H atoms, obtaining H_2 and O_2. These two gases can then be recombined to generate electricity, with water as the only reaction product [8, 9].
Water splitting is an endothermic reaction that requires an energy of $\Delta G^0 = 237\ kJ/mol$, which corresponds to a potential of $\Delta E^0 = 1.23\ V$ for each electron [10, 11]. The production of O_2 and H_2 from water is mediated by charge carriers: two electrons are needed to produce a H_2 molecule and four holes to produce an O_2 molecule as

shown in the reactions below :

$$\begin{aligned} &\text{Absorption of light: catalyst} + h\nu \longrightarrow e^- + h^+ \\ &\text{Water Oxidation: } 2H_2O + 4h^+ \longrightarrow O_2 + 4H^+ \\ &\text{Proton reduction: } 2H + 2e^- \longrightarrow H_2 \end{aligned} \tag{1.1}$$

where h^+ are the holes and e^- are the electrons [12]. Therefore, photocatalytic water splitting requires a catalyst material capable of releasing charges when illuminated by light. The most straightforward choice is a semiconductor with a band gap energy $E_g > 1.23\ eV$. Light with an energy $h\nu > E_g$ is absorbed by the material and electrons are excited in the conduction band, leaving holes behind in the valence band. The charge carriers are then available for the reactions shown in equation (1.1). The process is schematized in Figure 1.1 a).

1.1.1 Materials for photocatalytic water splitting

As stated before, semiconductors for photocatalytic water splitting require a band gap energy $E_g > 1.23\ eV$, so the reaction is activated when a photon with a wavelength $\lambda \leq 1008\ nm$ illuminates the semiconductor. Furthermore, the bottom level of the conduction band requires a potential less than the redox potential of H^2/H_2 (0 V vs. Normal Hydrogen Electrode), while the top level of the valence band needs a potential greater than $1.23\ eV$, as shown in Figure 1.1 b)[13]. Moreover, the produced e^- and h^+ must be efficiently separated and have a low recombination rate in order to be available to catalyze the redox reactions with water [14].
In order to commercialize a photocatalytic system, it must have an energy conversion efficiency of at least 10% if illuminated by sunlight and so far this efficiency has not yet been achieved, although it has been calculated as achievable from theoretical calculations [15, 16].

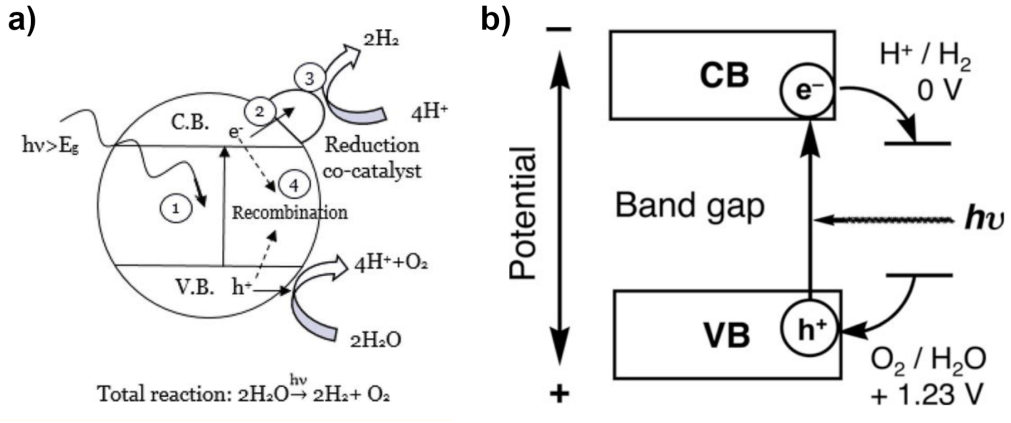

Figure 1.1: *a): Photocatalytic water splitting in a semiconductor[17] and b) Band gap level requirements in the semiconductor for water splitting [13].*

As shown in Figure 1.2, most of the solar energy striking the Earth surface consist of light in the visible ($400\ nm < \lambda < 700\ nm$) and infrared ($\lambda > 700\ nm$) ranges, which respectively account for 52% and 43% of the total solar energy flux[18, 19].

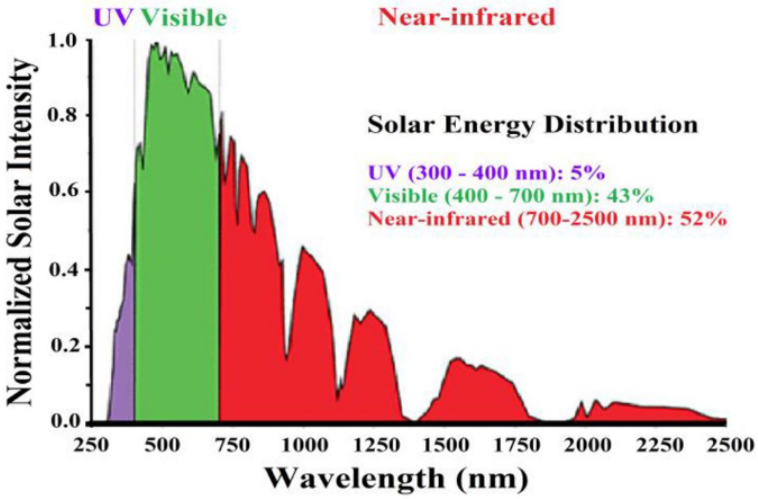

Figure 1.2: *Spectrum of the solar light illuminating Earth surface [20].*

Metal oxides are usually employed as catalysts for water splitting due to their band gap with the suitable energy for water splitting, stability and reusability [21]. Semiconductors for photocatalysis are divided into two main categories: narrow band gap semiconductors, that have a band gap energy in the visible range ($\simeq 2\ eV$) and wide band gap semiconductors, that have a band gap energy in the UV range ($\simeq 3-4\ eV$). Figure 1.3 shows the band gap energies and potential levels required for water splitting for a collection of photocatalytic semiconductors. Narrow band gap semiconductors absorb light in the visible range, however in many cases their conversion efficiency is limited[22, 23]. For example cuprous oxide Cu_2O is very cheap, has conduction and valence band position favorable for photocatalysis and a band gap energy of 2.2 eV, but suffers from photodegradation in water solutions [24]. Cadmium sulfide CdS has a band gap energy of 2.4 eV, that leads to a strong visible light absorption, band gap edges at the correct energies for water splitting and excellent electronic charge transfer, however fast charge recombination hinders its efficiency as a photocatalyst [25]. Finally, haematite (α-Fe_2O_3) is very abundant in the Earth crust, has a band gap energy of 2 eV, therefore a strong absorption in the visible range, furthermore, it is photostable under light illumination [26]. However, its low electron mobility and trapping of the photoexcited states limit the lifetime of e^- and h^+, which is of the order of picoseconds, an insufficient time to catalyze water splitting reactions [27].

On the other hand, wide band gap semiconductors are stable under light illumination in water solutions, but due to their band gap energy they cannot absorb light in the visible and infrared range, meaning that a large portion of the solar light striking the Earth surface will not interact with the semiconductor. Titanium dioxide TiO_2 was the first material to be ever reported as a catalyst in water splitting reactions in an article by Fujishima et al. in 1972 [28]. Then, in 1980 Kawai et al. examined the photocatalytic activity of TiO_2 powders and it was found that the anatase phase gave better results than rutile, due to the fact that the conduction band of anatase has an energy 0.1 eV more negative than the one of rutile [29, 30]. TiO_2 is cheap, has a band gap of 3.0 eV in its anatase form and has a high electron mobility, however it has a low charge separation efficiency and absorbed oxygen molecules can act as electron scavengers [31, 32]. Finally Cerium Oxide CeO_2, which will be described in more detail in the following sections, has a band gap between 3.2 and 4 eV [33], an

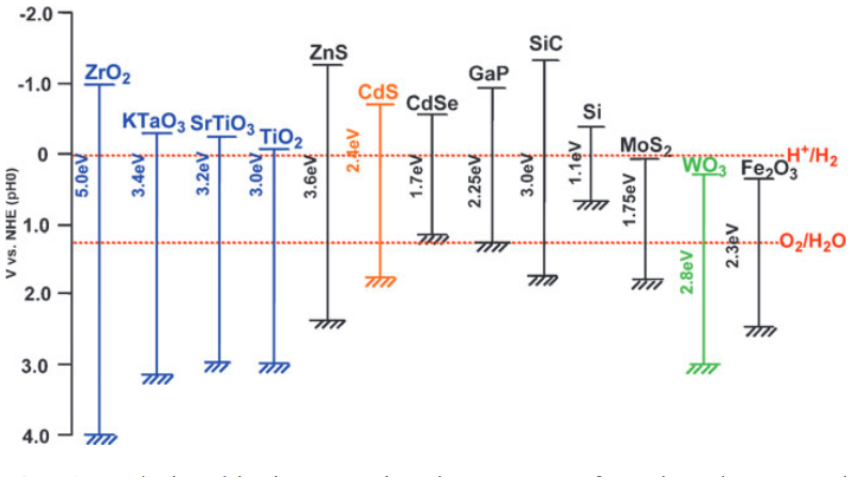

Figure 1.3: *Band gap energies and potential levels required for water splitting of a collection of photocatalytic semiconductors[18].*

high reducibility [34] and oxygen storage capacity [35].
As mentioned before, the main disadvantage in using wide band semiconductor for photocatalysis is the fact that these materials do not absorb light in the visible and infrared range. Various approaches to enhance the absorption wavelength range have been analyzed during the years. For example nanostructuration [36, 37], defect engineering [38, 39], doping with metals such as Fe, Mn, Ti, Sn, Cu and Ag [40, 41, 42, 43].

1.2 Cerium Oxide

Cerium (Ce) is the 58^{th} element of the periodic table and it belongs to the Lanthanides group. Despite the fact that Lanthanides are also called "rare earths", Ce is quite common on the Earth's crust and constitutes 0.0046% of its weight, with a higher abundance than major industrial metals such as Cu and Pb [44].
Lanthanides are characterized by the occupation of the $4f$ orbitals, shielded from the atom's environment by the $4d$ and $5p$ electrons, that gives them unique catalytic, magnetic and electronic properties [45, 46]. Being the second element in the Lanthanides group, the 4f orbital of Ce is occupied by only one electron. Ce electronic configuration is [Xe] $4f^1$ $5d^1$ $6s^2$ [47].
In ambient environment Ce binds with oxygen to create oxides and the two main compounds are CeO_2, also known as ceria, and Ce_2O_3. In the former, Ce has a tetravalent state Ce^{4+}, while in the latter it has a trivalent state Ce^{3+}. The ability of cerium to form oxides in both tetra- and tri- valent states is caused by its relatively low fourth ionization potential compared with other Lanthanides[48, 49]. This means that, even if CeO_2 is the most stable phase, cerium can switch easily between Ce^{4+} and Ce^{3+} states if placed in a reducing or oxidizing environment. This property also causes cerium oxide to have an high Oxygen Storage Capacity (OSC), which is the ability to store, transport and release oxygen. In fact, when a cerium oxide sample is placed in a reducing environment, an O atom can be removed from the material, creating a vacancy. As a consequence the excess electrons are re-localized on the Ce atoms by reducing two Ce^{4+} ions into the Ce^{3+} state. The Ce atoms can then revert back to their original state if the sample is placed in an oxidizing environment [35]. The release of O can favour redox reactions, so CeO_2 is

widely used in technological application as a catalyst[50].

1.2.1 Crystal Structure

CeO_2 has a cubic fluorite-type structure (space group $Fm\bar{3}m$), as shown in Figure 1.4 a). Each Ce atom is surrounded by eight oxygen atoms, placed in tetrahedral positions, as shown in Figure 1.4 b). As shown in Figure 1.4 c), the structure can also be depicted as "CeO_8" cubes with a Ce atoms at the center and eight O atoms in the corners. The CeO_2 unit cell parameter at RT is a= 5.41 Å, but it increases with temperature together with O and Ce atomic displacement. O atomic displacement increases more than the one of Ce atoms, causing a higher mobility for O atoms with respect to Ce ones[51].

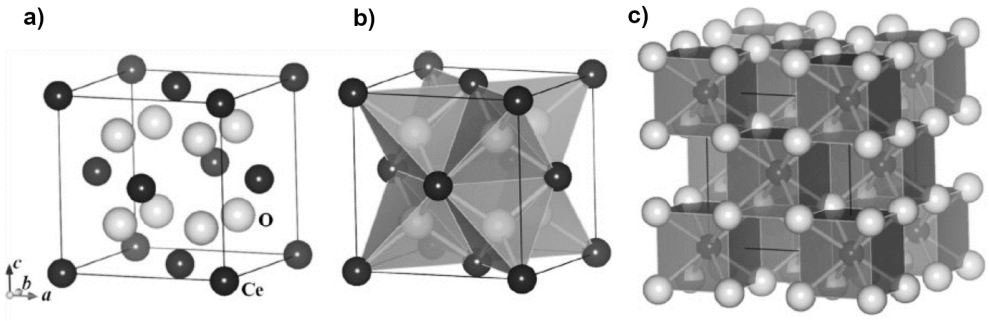

Figure 1.4: *a) Fluorite-type crystal structure of CeO_2.b) Cerium atoms placed in tetraedral positions around O atoms. c) Crystal structure of CeO_2 with CeO_8 cubes [52].*

The most thermodynamically stable surface is the {111} one, it is characterized by an hexagonal symmetry and has a surface lattice parameter of 3.83 Å [53]. As shown in Figure 1.5 a), the {111} surface terminates with three-fold coordinated O atoms in the first layer, followed by seven-fold coordinated Ce atoms in the second layer.

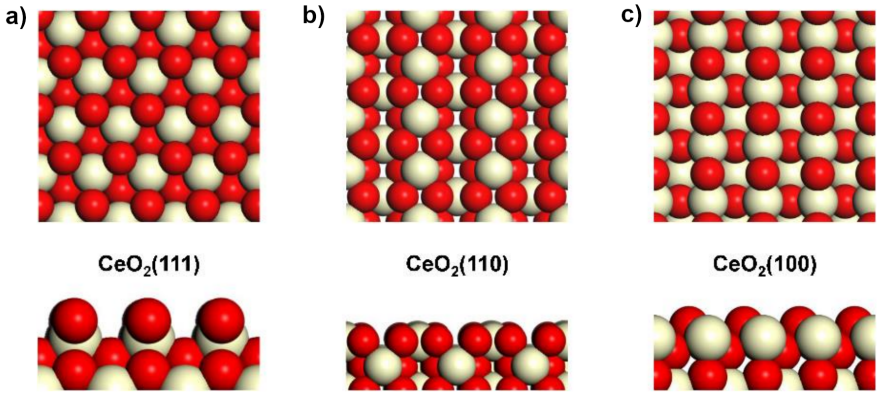

Figure 1.5: *Top (up) and cross-sectional (bottom) view of the a) {111}, b) {110} and {100} surfaces of ceria [54].*

This surface is non polar with non net dipole moment perpendicular to the surface. Along the direction normal to the (111) plane, a repetition of the three-layer O-Ce-O unit can be identified. This means that a ceria monolayer can be defined by the thickness of the O-Ce-O unit, measuring 3.12 Å [55]. Even if {111}

is the most stable surface, also the {110} and {100} ones can be exposed. Their top and side view are shown in Figure 1.5 b) and c).

Ceria lattice parameter of the {111} surface is larger by 30-40 % than the one of most 3d and 4d metals, however epitaxial ceria films with the {111} surface exposed have been grown on hexagonal surface symmetry metal substrates. Some examples are Pt{111} [56], Cu{111} [57], Rh{111} [58] and Au{111} [59]. This behaviour is due to the formation of a supercell n:m, where n ceria surface unit cells match m substrate surface unit cells [53].

Ce_2O_3 has an A-type hexagonal structure (space group $P\bar{3}m1$) with two Ce atoms and three O atoms in the unit cell. The Ce atoms are seven-fold coordinated while two of the oxygen atoms are four-fold coordinated, whereas the third oxygen atom is six-fold coordinated [60]. Figure 1.6 a) shows the crystal structure of Ce_2O_3. The lattice parameters for Ce_2O_3 are a=b= 3.89 Å and c= 6.06 Å.
The most stable surface for Ce_2O_3 is the {0001} one. The top and side view of the surface is shown in Figure 1.6 b). In this case, the repetition unit is the five layer O–Ce–O–Ce–O. The surface has three-fold coordinated O atoms, while in the bulk they are four- or six- fold coordinated.

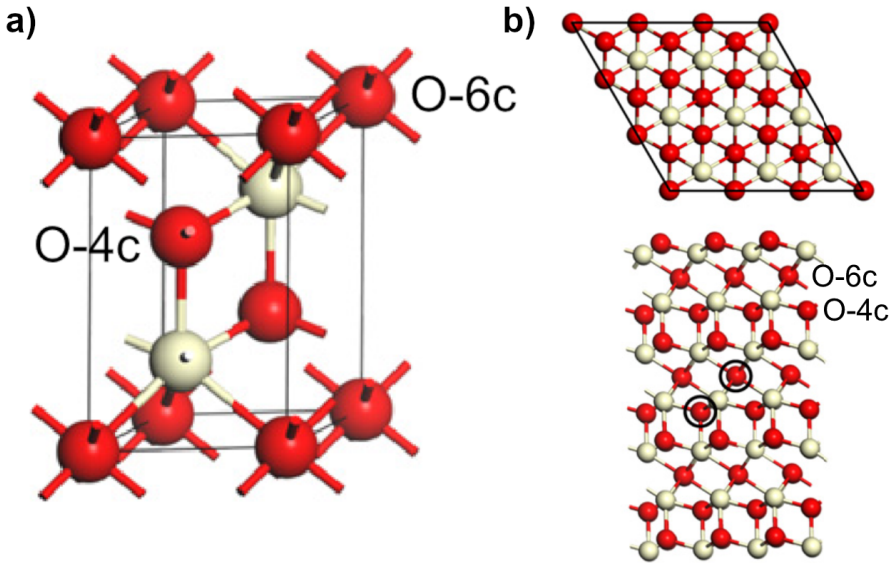

Figure 1.6: *a) Ce_2O_3 crystal structure, the four- and six-fold coordination of oxygen atoms is also shown. b) Top and cross sectional view of Ce_2O_3 {0001} surface [60].*

1.2.2 Electronic structure

Ce^{3+} and Ce^{4+} ions have a different occupation of the 4f levels: they are empty in the 4+ state, while in the 3+ state an electron occupies them.
The high oxygen storage capacity in ceria is related to the oxygen-vacancy formation process in CeO_2, this process is schematized in Figure 1.7. Starting from a CeO_2 lattice, which contains only Ce^{4+} ions, an O atom is removed. The excess of charge from the O atom removal can be balanced by the reduction of two Ce atoms, that switch from a Ce^{4+} to a Ce^{3+} state.

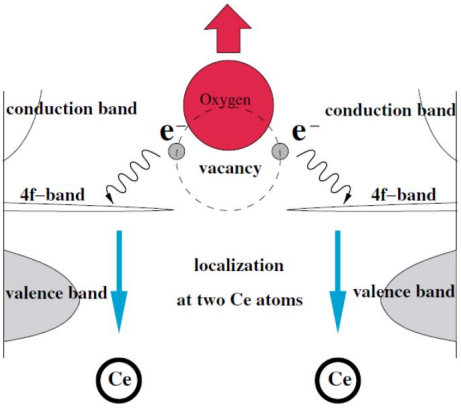

Figure 1.7: *Ce^{4+} ions reduction to Ce^{3+} following an oxygen vacation formation[61].*

In order to better comprehend the reduction of CeO_2 samples, it is needed to understand if the additional electrons occupy the 4f orbitals of the neighbouring Ce atoms [35], or if they locate on other Ce atoms [62]. It was initially believed that the former hypothesis was the correct one, but recent studies from Ganduglia-Pirovano et al. [63] and Li et al. [64] showed very similar stabilities of different Ce^{3+} configurations in terms of coordination shell around the vacancy.

In the oxygen vacancy three points in the structure have to be considered: the ab-

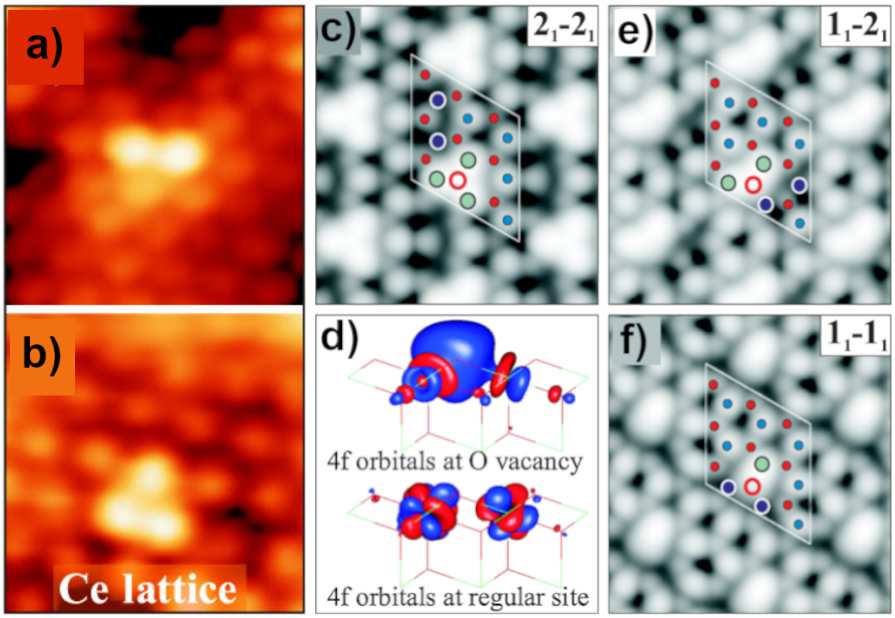

Figure 1.8: *a) and b): STM images showing an O vacancy in ceria surrounded by three and two Ce^{4+} ions respectively. c), e) and f) show DFT study results for STM empty-state imaging of the atoms surrounding an O vacancy. The green circles represent Ce^{4+} atoms, that appear brighter than Ce^{3+} ions in the STM images. d) The difference in brightness for the two ions is caused by the expansion of the 4f orbital of Ce^{4+} atoms when they are close to an O vacancy. Adapted from [65].*

sent oxygen site and the two neighbouring Ce^{3+} sites. The relocalization of electron charge caused by the O vacancy has been studied by Jerratsch et al. by scanning tunneling microscopy (STM) and Density Functional Theory (DFT)[65]. As it can be seen in Figure 1.8, the experiment concluded that both Ce^{3+} sites (Figure 1.8 a)) or at least one (Figure 1.8 b)) are not adjacent to the O vacancy. Ce^{4+} ions

appear brighter on STM, as demonstrated by DFT studies of empty-state STM images shown in Figure 1.8 c), e) and f). The brightness difference between Ce^{3+} and Ce^{4+} ions when near to an O defect is due to the expansion of the 4f orbital of Ce^{4+} atoms, as shown in Figure 1.8 d). If a vacancy is surrounded by three Ce^{4+} atoms, a triple bump STM image is measured as in Figure 1.8 a). However, such feature is very uncommon: a two-bump image, as seen in Figure 1.8 b), appears much more often. The two-bump feature is related to the presence of two Ce^{4+} ions placed near the O vacancy and corresponds to the situation shown in Figure 1.8 d).

1.2.3 Tuning photocatalytic properties of CeO_2 with metals

CeO_2 doped with metals

CeO_2 photocatalytic behaviour can be modified by doping with cations, this normally causes a decrease in the oxygen vacancy formation energy. This effect is also related to the valence of the dopant ion which, if different from the one of Ce^{4+}, produces a change in the electronic structure of CeO_2, reducing the oxygen vacancy formation energy and in general enhancing the photocatalytic activity[66].
The energy of O vacancy formation E_V is defined as:

$$E_V = E_r + \frac{1}{2}E\left[O_2(g)\right] - E_s$$

where E_r is the energy of the semiconductor layer with one oxygen vacancy in the top layer, $E\left[O_2(g)\right]$ is the energy of an O_2 molecule in the gas phase, and E_s is the energy of the layer without an oxygen vacancy [67]. A dopant material is called low valence dopant (LVD) when it has a lower valence than the positive ion that it replaces (in this case, Ce^{4+} atoms), while instead it is called high valence dopant (HVD) if it has a higher valence. The valence of a dopant is defined according to the stable oxides that it produces. For example Fe can create oxides with II or III valence and is a LVD, instead Ta can create only Ta_2O_5 as a stable oxide, so Ta has a V valence and is a HVD dopant for Ce [68].
DFT studies [67, 69] suggest that transition metal dopants belonging to the first groups in the periodic table interact to modify the reducibility of Ce atoms, while instead late transition metals act as a reduction center. LVDs reduce the E_V because they create an hole at the top of the valence band. When an O atom is removed from the lattice, one of the two excess electrons can fill the hole in the valence band, thus reducing its energy [67]. HVDs reduce the E_V all by a similar amount. This effect can be due to two different mechanisms:

- Through theoretical studies of the projected density of states it has been found that dopants with more than 4 electrons to create bonds give the excess electrons to ceria to reduce Ce atoms. This means that when they substitute a Ce atom in the lattice they all have 4 electrons to create bonds even if some of these dopants, such as W and Mo start with 6 electrons to create bonds and Ta and Nb start with 5.

- In their respective oxides, the dopant bonds with oxygen are shorter than the Ce-O bond in CeO_2. When these dopants substitute Ce, they pull the O atoms on the surface towards the inside of the material, weakening O bond to the surface.

Yang et al. studied through DFT the effects of doping ceria samples with Zr [70] and Pd [71].
In the first case, it was found that Zr caused the E_V to be lowered from 3.03 to 2.38 eV when the O vacancy is formed near the Zr dopant. Structurally, it has been observed that the displacement caused by the vacancy for the oxygen anions are much larger in the Zr-doped ceria sample (0.38 Å) than undoped ceria (0.28 Å), meaning that the O atoms close to Zr atoms have a higher mobility than in the undoped CeO_2 sample. Furthermore, the Ce-O distances in undoped ceria are shorter than the Ce-O distances in Zr-doped samples, while Zr-O distances are shorter than the Ce-O distances in both samples. For both the doped and undoped samples, the surplus electrons reduce two Ce^{4+} neighbouring the vacancy to the Ce^{3+} state.
In the case of Pd, the E_V was lowered much more than in the Zr case: from 3.0 to 0.6 eV. In this case the enhancement of reducibility through doping has not a structural origin as with Zr, but an electronic one. In fact, it was found that the reduction of E_V in Pd doped ceria was mainly due to emerging Pd-induced gap states above the valence band and below the empty Ce 4f states.
Fe-doped ceria shows an even lower E_V of 0.15 eV for the O atoms neighbouring the dopant atom. In this case the lowering of E_V through doping was caused both by a structural distortion in the lattice and the addition of new metal-induced gap states at the Fermi level [72].

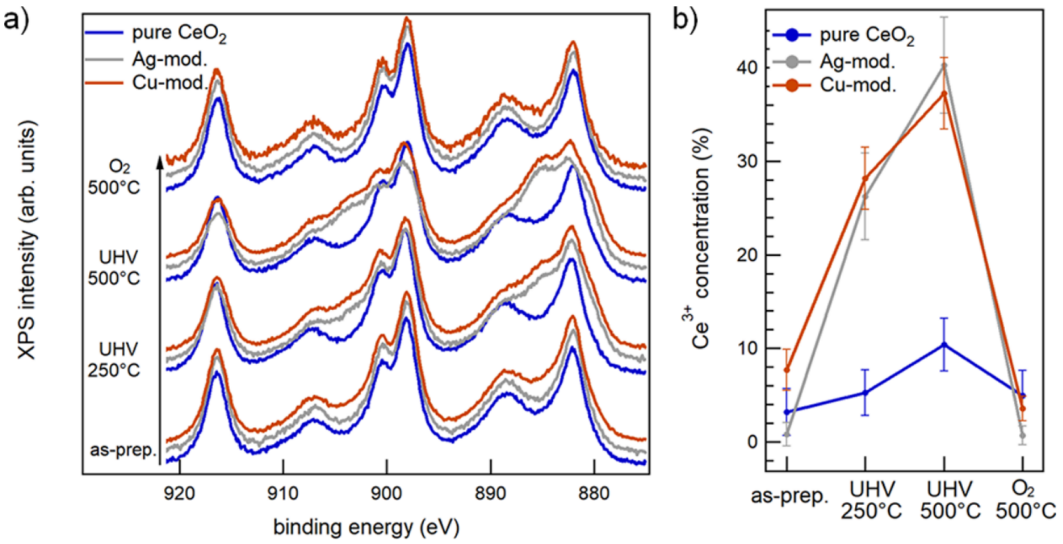

Figure 1.9: *a): Ce 3d XPS spectra of undoped, Ag-doped and Cu-doped taken at RT after the different stages of the reducing and oxidizing procedure. b) Change of the Ce^{3+} concentration in the three samples during the reduction/oxidation cycle. The concentration are obtained by fitting the Ce 3d spectra in a). Taken from [73].*

Gasperi et al. studied epitaxial films of pristine and Cu- and Ag-doped ceria both expirementally and theoretically by using DFT calculations [73]. The samples, consisting of 2 monolayers of ceria doped or undoped, were deposited on a Pt(111) single crystal. The doping percentage for Cu- and Ag doped samples has been estimated at 12-13 %. The samples underwent reduction cycles in Ultra-High Vacuum condition while increasing the temperature and the evolution of the oxidation state was followed by X-ray photoemission spectroscopy, as shown in Figure 1.9. DFT calculations obtained negative E_V for the doped samples: -1.40 eV for Cu and -1.36 eV

for Ag, meaning that an oxygen vacancy is formed spontaneously near the dopant. The decrease in E_V between undoped and doped ceria is 3.32 eV and 3.27 eV for Cu and Ag, respectively. Furthermore, the creation of an O vacancy cause the Ag ion to be reduced from the Ag^{2+} to the Ag^{1+} state, together with the Ce atom that shifts from Ce^{4+} to Ce^{3+}. Cu-doped samples also exhibit a similar behaviour. As shown by other DFT studies, Cu-doped samples introduce lattice distortion, which is not present in Ag-doped samples [74, 75].

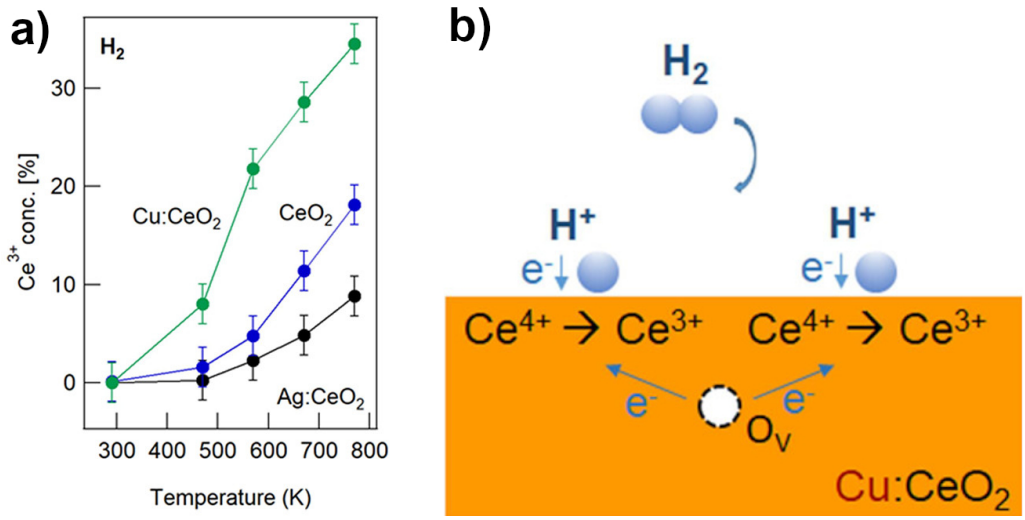

Figure 1.10: *a): Ce^{3+} concentration calculated by XPS in ceria samples with different metal dopants in function of temperature during the heating in H_2 and b): reduction of two Ce atoms in the Cu:CeO_{2-x} samples caused by H_2 adsorption or O vacancy formation. Adapted from [76].*

A more recent work by Vikatakavi et al. studied the reducibility of undoped and Ag and Cu-doped ceria samples in both UHV and H_2 environments by also describing the dynamics of reduction [76]. Theoretical calculations found that dopant Cu atoms are more likely to replace Ce atoms than O atoms or be placed in interstitial positions[77].The introduction of copper as a dopant greatly enhances the reducibility of CeO_2. Figure 1.10 a) shows the Ce^{3+} concentration measured by XPS in function of temperature in the heating cycle in H_2 in pristine ceria and 2% Cu-doped ceria samples, the latter shows a greater Ce^{3+} concentration compared with the former[76]. In the same work, Cu:CeO_2 properties were investigated theoretically via density functional theory calculations using the Quantum Espresso package. In particular, the Cu:CeO_{2-x} surface was studied during reduction. The computations found a barrier for H_2 dissociation on Cu:CeO_{2-x} of 0.8 eV, which is not much lower than the one for pristine CeO_2 of 0.99 eV[78]. However, the adsorption of hydrogen on the surface of Cu-doped ceria causes the Ce atoms to be reduced from 4+ to 3+ and Cu atoms from 2+ to 1+. Since Cu^{1+} is very reactive, it reduces the dissociation energy potential barrier for a subsequent H_2 to 0.33 eV, which is much lower than the one for undoped CeO_2. This process is schematized in Figure 1.10 b) and explains the net increase in Ce^{3+} concentration during the heating cycle in Figure 1.10 a).

Plasmon Resonance on metal nanoparticles coupled with CeO_2

As mentioned before, CeO_2 has the band gap energy in the UV range, while most of the incoming radiation on the Earth surface is in the visible and infrared range. This factor limits the use of CeO_2 in photocatalysis.
However, it is possible to sensitize CeO_2 to absorb light at lower wavelengths by coupling it with noble metal nanoparticles (NPs), such as Ag, Au and Cu. This is due to a process called Localized Surface Plasmon Resonance (LSPR), that occurs at the interface between a dielectric (such as CeO_2) and noble metal NPs with a dimension lower than the wavelength of the incoming radiation[79].

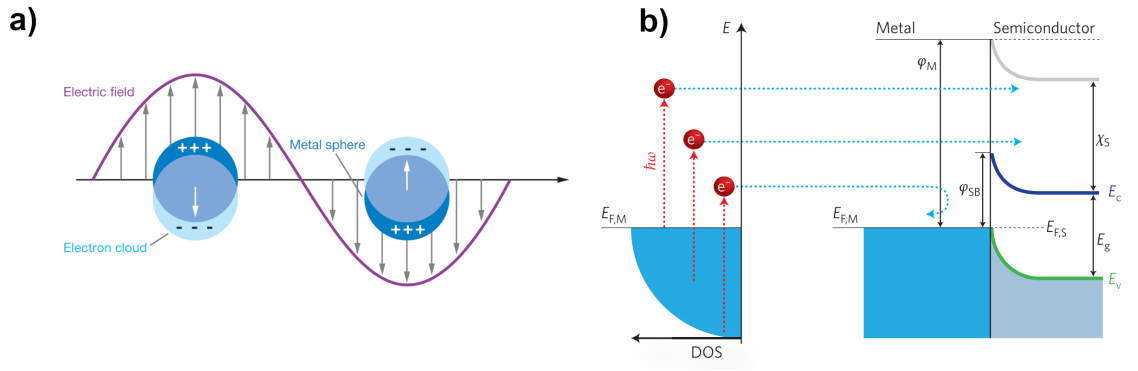

Figure 1.11: *a) Formation of a LSPR caused by an incoming electromagnetic wave on metal spheres which are smaller than the λ of the radiation [80]. b) On the left, electrons are excited above the Fermi energy ($E_{F,M}$) in the metal by the incoming e-m wave photon energy. On the right, the Schottky barrier $\varphi_{SB} = \varphi_M - \chi_S$ on the interface between the metal and semiconductor is shown (φ_M is the work function of the metal and χ_S is the electron affinity of the semiconductor). Electrons travel to the conduction band (E_C) of the semiconductor[81].*

The interface between a metal and dielectric can be modeled as made by a conduction electron negative cloud and fixed positive ions (the nucleus of the atoms). A plasmon is formed in the material when the electrons start oscillating with the electric field of an incoming electromagnetic wave[82]. For a macroscopic metal surface, the plasmon propagates on the plane in the x and y-directions for distances of the order of tens to hundreds μm and is called Surface Plasmon[83]. However, if the metal is part of a NP smaller or comparable with the wavelength of the incoming radiation, the plasmon remains confined on the NP and it is called Localized Surface Plasmon, as shown in Figure 1.11[84]. The absorption of the incoming electromagnetic wave from the NP has a maximum called LSPR, which is found in the visible range for noble metal (Ag, Cu and Au) NPs, which makes these elements the most appealing to create metal NPs/dielectric interface for solar light harvesting[85]. The frequency of LSPR depends on the material, shape, size, population density of the NPs and dielectric environment, which means that the energy of LSPR can be tuned by changing these parameters of the NPs[86].
By embedding plasmonic NPs within wide band gap semiconductors, the metal NPs can act as antennas, absorbing light in the visible range and then releasing its energy to the surrounding dielectric medium through charge or energy transfer[87]. The charge separation is also facilitated by the presence of a Schottky barrier between the metal and semiconductor, that avoids the charges to go back to the metal and recombine, as shown in Figure 1.11 b).

Various processes have been suggested as a cause of the photoactivity increase of wide band gap semiconductors when plasmonic nanoparticles are embedded in them. The most prevalent of these methods include light trapping[88, 89], hot electrons injection[90, 91], and direct electron transfer[92].

- **Light Trapping:** The metal NPs scatter the incoming light into the semiconductor. The distance traveled by the light in the semiconductor is increased and hence the overall light absorption is improved. This phenomenon does not make lower energies accessible for absorption by the semiconductor, but simply increases the intensity of light absorbed by the semiconductor in its absorption range (for CeO_2 in the UV range). Light trapping is effective for NPs with a diameter larger than 50 nm.

- **Hot electrons injection:** Light interacts with the NPs and electrons are generated through Landau damping or interband transitions. The electrons that have an energy higher than the Schottky barrier at the metal–semiconductor interface can be injected into the conduction band of the semiconductor.

- **direct electron transfer:** After light is absorbed by the NPs, electrons are directly excited into empty states of the semiconductor conduction band

1.2.4 Polarons in Cerium Oxide

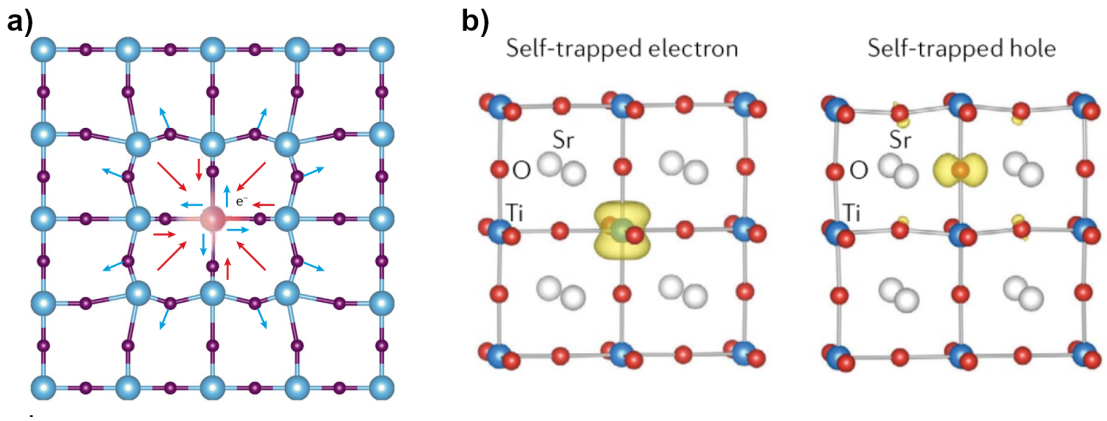

Figure 1.12: *a) Small polaron formed by the polarization caused by the self-trapping of an electron at a lattice site and b) electron and hole polaron in $SrTiO_3$[93].*

Polarons are quasi-particles originated from the coupling between charge carriers and lattice distortions. In particular, polarons are formed when the charge moves slowly enough to distort the surrounding lattice in response to its influence. The charge carrier is then confined by the potential well caused by the lattice distortion, as shown in Figure 1.12 [94]. This phenomenon causes the charge to be trapped by the potential created by itself and so it is called "self-trapped". Polarons can be divided in two types depending on the size of the confinement as a function of the number of lattice unit cells. Large polarons extends over more unit cells, while small polarons are confined inside a single unit cell[95].
The study and understanding of small polarons formation and evolution in catalytic metal oxides such as TiO_2 and CeO_2 is crucial, as the formation of small polarons can negatively modify their photocatalytic activity[96].
The short lifetime and dynamic behaviour of polarons in materials require the use

of ultrafast experimental techniques that are capable to characterize the electronic states in a material few picoseconds after the excitation that causes the polarons. For this reason, ultrafast pump-probe spectroscopies are used in these studies. The metal oxide is excited with a visible or UV pump laser and then UV-Visible or X-ray absorption spectroscopy is performed with a probe laser. The time delay between the pump and the probe can be scanned from few hundreds of femtoseconds to hundreds of picoseconds. By computing the difference between the obtained spectrum when the pump laser is switched on and when is switched off, the time evolution of a small polaron formed by the excitation with the pump laser can be studied. Previous studies have investigated the polaron formation in metal oxides such as TiO_2 or hematite[97, 98]. A pump probe experiment to detect the polaron formation in ceria is described by Pelli Cresi et al[99]. In this experiment, a 6 nm thick film of CeO_2 grown by MBE on quartz substrates was studied with ultrafast spectroscopy. In particular, Femtosecond Transient Absorption Spectroscopy (FTAS) has been used to characterize the dynamics of the ceria thin film optical response after the excitation with a laser pump with a photon energy above ceria energy gap. As a pump, a 275 nm (4.5 eV) laser pulse has been used, while the probe was scanned in a visible (2.0-3.5 eV) or a UV (3.5-4.3 eV) supercontinuum. The probe has been used to measure the light absorption of the system when excited (laser pump on) and unexcited (laser pump off), then the absorption difference pump on-pump off ΔA is calculated. ΔA is measured as a function of the time delay between the pump and the probe.

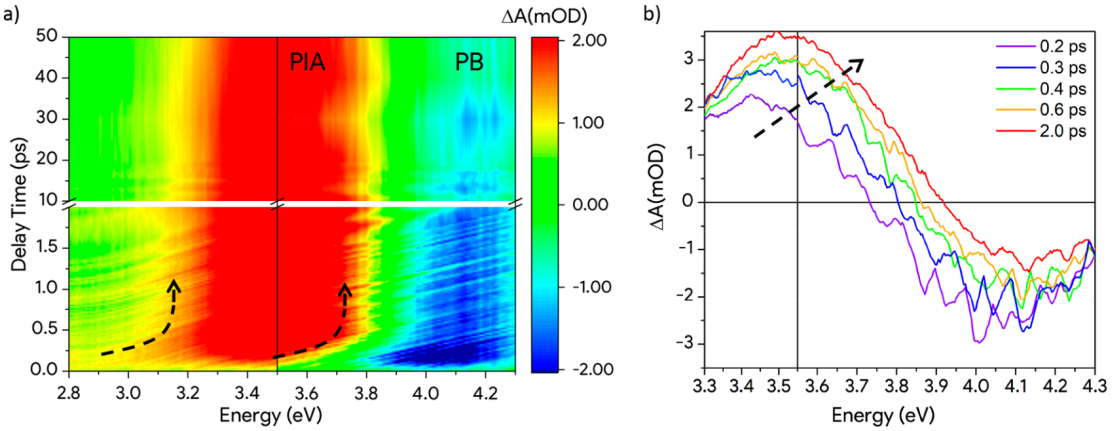

Figure 1.13: *a) False color transient absorbance map relative to the photoexcitation of the sample. The black arrows highlight the shift of the PIA band during the first picosecond. b) Transient absorbance spectra of CeO_2 in the UV region. In both figures the continuous line at 3.55 eV represents the energy where the visible supercontinuum has been joined with the UV supercontinuum[99].*

Figure 1.13 a) shows a false color transient absorbance map relative to the photoexcitation of the sample. The colour in the map represents the intensity of ΔA expressed as a function of the probe photon energy on the horizontal axis and pump-probe delay time on the vertical axis. Figure 1.13 b) shows ΔA as a function of the probe photon energy for different pump-probe time delays. In both figures, the continuous black line at 3.5 eV represents where the visible supercontinuum has been joined with the UV supercontinuum. FTAS spectra show two main signals in the UV range: a Photobleaching (PB) one at 4 eV and a photoinduced absorption (PIA) at 3.55 eV. PIA and PB signals show a change in their energy position on the first

picosecond, while they simply undergo an intensity decay at longer pump-probe delay times. The spectral change of PIA and PB on the first picosecond is shown for PIA in Figure 1.13 a) and b) by a dotted black arrow.

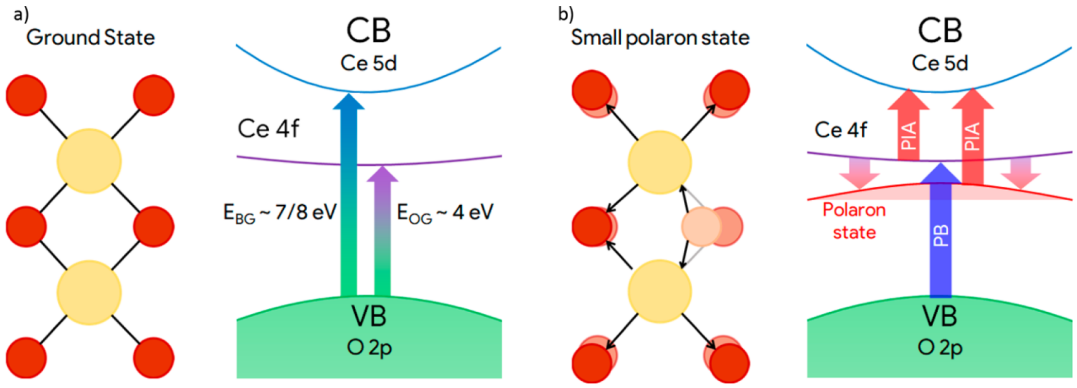

Figure 1.14: *a) Ground state of CeO_2, showing a simplified scheme of the crystal structure, with Ce atoms (yellow) surroinded by O atoms (red). The band gap and conduction and valence band are also shown. b) CeO_2 after the photoexcitation: The Ce 4f states are filled and this cause a lattice distortion that modifies the band structure. A small polaron state is formed below the Ce 4f state. The photobleaching (PB) and photoinduced absorption (PIA) are also shown as blue and red arrow respectively[99].*

In order to further describe the FTAS spectra, it is necessary to consider CeO_2 electronic states before and after the pump laser excitation. Figure 1.14 a) shows the ground state of CeO_2 where Ce atoms are surrounded by 8 O atoms. CeO_2 has a valence band (VB) with mainly oxygen 2p states, a conduction band (CB) with a 7-8 eV energy gap and empty Ce 4f states in the middle of the band gap[100]. The energy difference between the 4f states and the VB is about 4 eV. Figure 1.14 b) shows the distorted ceria lattice caused by the pump excitation, which leads to the formation of a small polaron state. The 4f states are partially filled by the pump excitation and this transition partially depletes the valence band and it induces the appearance of the negative PB signal. The PIA signal is instead assigned to the transition from the the photoexcited 4f states to the CB.
The blue shift related to the PIA signal after the first picosecond can be explained by the lowering of the 4f electrons energy, that thus require a higher energy to be excited into the CB. This new state at a lower energy than the Ce 4f states, where the 4f electrons are transferred is compatible with the creation of a small polaron state, according also to experimental results for donor-modified ceria and theoretical predictions [101, 102]. From the FTAS spectra two components are extracted: one related to the first 2 picoseconds after the excitation in which the PIA blue shift occurs, and the other after the first two picoseconds. By analyzing these two components as a function of the pump-probe time delay, it is found that the second component has a rise time of 330 fs and a decay time of 310 ps. Since the second component is related to the appearance of a small polaron state, it can be concluded that the polaron state is formed after 330 fs and has a lifetime of 310 ps.

1.3 Niobium Oxide

Niobium (Nb) is the 41^{st} element of the periodic table and it belongs to the Transition Metals group. Niobium has an abundance of 8 ppm in the Earth's crust and it's usually found together with Tantalum to form the mineral of Tantalite or Columbite[103, 104].
Niobium can form stable carbides, nitrides, borides and silicides since it possesses a high interatomic bonding energy[105]. For these reasons niobium found its application in the stabilization of stainless steel in order to shield the alloy from granular corrosion, lowering the necessary amount of carbon in steel. A small amount of niobium is necessary to be added in the alloy, from 100 to 5000 ppm, in order to prevent the steel degradation and thus creating a tougher and stronger alloy[106]. Nb based alloys also present high melting points, refractory properties and low densities[107]. Given its good biocompatibility, Nb is also used in medical applications to build implants, protheses and hard tissue replacement[108]. Finally, Niobium is the element with the highest superconductivity critical temperature and some of its compounds, such as $Nb_{0.75}(GeAl)_{0.25}$, have the highest temperature for superconductivity (T_C=20.7 K)[109].
Niobium can also bond with oxygen to create three main oxides: Nb_2O_5, NbO_2 and NbO, where Nb shows an oxidation state of 5+,4+ and 2+ respectively[110]. The most thermodynamically stable niobium oxide is Niobium pentoxide (Nb_2O_5) and in fact a small Nb_2O_5 layer is formed on top of metallic Nb[111]. However, niobium oxides systems present different stoichiometric and non-stoichiometric phases, with some polymorphs and metastable systems. Figure 1.15 depicts the three major Niobium oxides in function of their O/Nb ratio, showing that metastable oxides between Nb and NbO and NbO_2 and Nb_2O_5 exist.

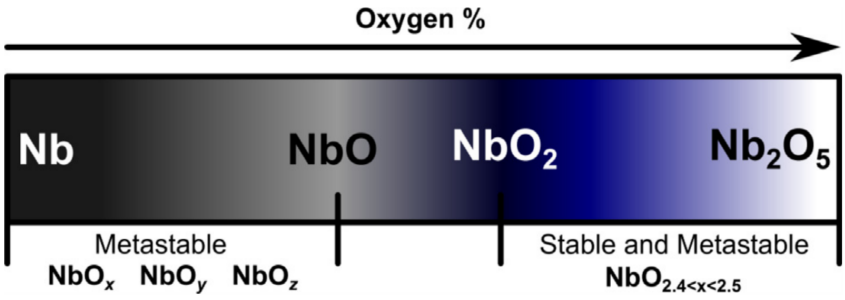

Figure 1.15: *Scheme of the different oxidation states of niobium with its three major oxides[110].*

This leads to the difficulty in synthesizing a specific niobium oxide without obtaining a combination of phases or Nb/O ratios.

1.3.1 NbO

NbO lattice is a FCC structure of O_h^1 space group, with 3 Nb atoms in positions (0½½; ½0½; ½½0) and 3 O atoms in positions (½00; 0½0; 00½)[112]. As shown in Figure 1.16, each Nb atom is coordinated to four O atoms in a square flat array. Furthermore, NbO structure is quite unusual, since it presents 25% ordered vacancies in Nb and O sublattices, Nb atoms are arranged in octahedral shape.
Niobium monoxide is a superconductor at a temperature below $T_c = 1.38\ K$, by increasing the Oxygen ratio the resistivity increases, while by increasing the Nb

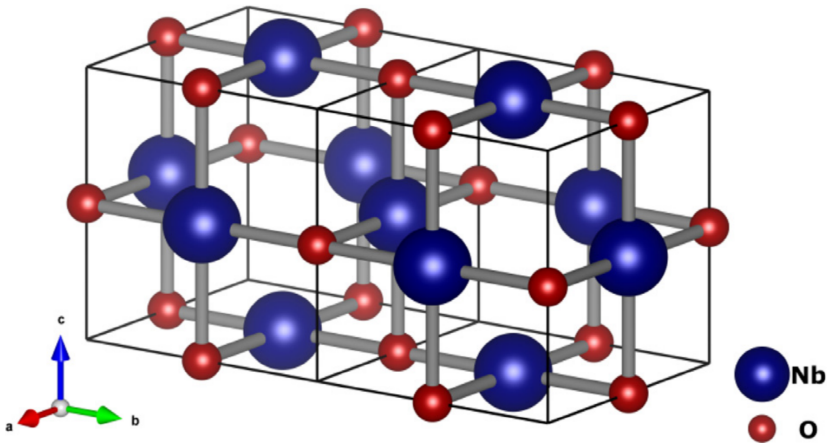

Figure 1.16: *NbO crystal structure[113].*

ratio, T_c increases[114]. This behaviour was explained in [114] as the fact that the sample was a mixture between Nb, NbO and NbO_2, with the Nb phase contributing to the increase of T_c and NbO_2 phase contributing to the resistivity increase.
Due to its higher oxygen diffusion with respect to Nb, NbO is a promising candidate for solid electrolyte capacitors in combination with Nb_2O_5 as a dielectric[115, 116].

1.3.2 NbO_2

NbO_2 crystal structure is a distorted tetragonal superstructure with a rutile sublattice, its space group is C^6_{4h} [117]. NbO_2 crystal structure is shown in Figure 1.17 a). As it can be seen from the figure, NbO_2 structure presents chains of edge-sharing octahedrons. Each octahedron is made by one Nb atom in the center surrounded by six O atoms placed on the edges, the NbO_6 octahedron shares the O atom edges with other six octahedrons.

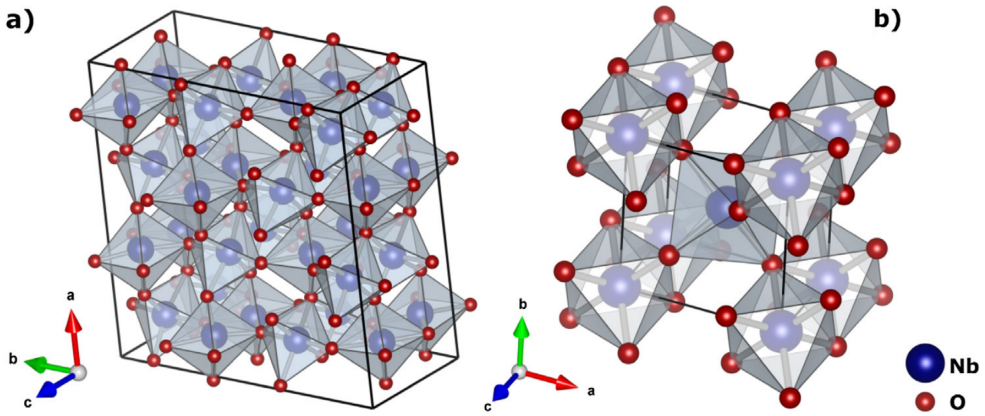

Figure 1.17: *a) Tetragonal and b) Rutile structure of NbO_2[113].*

NbO_2 suffers a second order phase transition around 800°C, where the crystal structure changes from a distorted rutile as in Figure 1.17 a) to a regular rutile lattice, shown in Figure 1.17 b)[118]. The transition is similar to the one observed on vanadium dioxide at significantly lower temperatures (20°C)[119, 120]. The transition modifies the electrical conductivity of the material from a value typical of a semiconductor to one comparable with that of a metal, so this temperature-driven modification is identified as a semiconductor-metal transition[121]. This abrupt change in

conductivity has interesting applications in memresistive devices, ultrafast electrical switches and thermal sensors[122]. As pointed out before, the transition occurs in VO_2 at lower temperature, which is however very close to room temperature, so it could be beneficial to develop these devices by using NbO_2 instead of VO_2 in order to isolate the electronic properties from temperature effects. In NbO_2, in analogy with the case of vanadium dioxide[123], it was shown that the thermally-induced phase transition can also be triggered by light absorption[124], a very appealing aspect in view for example of application in ultrafast switches. However, in the case of NbO_2 the detailed atomic scale mechanisms that drive the transition are still largely unknown. In particular, the role of electronic correlations and the interaction with the lattice in the transition are still largely debated[125]. A detailed understanding of the transition mechanism, besides being interesting for basic science, may lead to a design-driven optimization of the material for application in devices.
Other applications of NbO_2 include its use as an electrocatalyst for N_2 fixation [126] or, by employing its good chemical stability, as a highly efficient electrocatalysts for oxygen-reduction reactions [127].

1.3.3 Nb_2O_5

Nb_2O_5 is the most thermodynamically stable between the oxides of Niobium. Niobium pentoxide can be found in the amorphous state or in many crystalline polymorphs, which differs in their physical properties also depending on synthesis technique used.
The nomenclature of Nb_2O_5 polymorphs can be misleading, as some of them were classified by using greek letters before all of them have been discovered. The nomenclature that will be used here to describe Nb_2O_5 polymorphs is the one used in [128], which follows and extends the one used by Brauer et al.[129], the first one to study the niobium oxides. In this nomenclature, some polymorphs were classified by their formation temperature: TT, T, M and H (from Tief–Tief, Tief, Medium and Hoch, which means low–low, low, medium and high in german), while others by the shape of their particles: B, N and R (from Blätter, Nadeln and Prismen, which means leaves/plates, needles and prisms in german). The main polymorphs in which Nb_2O_5 can crystallize, together with their crystal system and space group, are shown in Table 1.1.

Phase	Crystal System	Space Group
T-Nb_2O_5	orthorhombic	D_{2h}^9
B-Nb_2O_5	monoclinic	C_{2h}^6
H-Nb_2O_5	monoclinic	C_{2h}^1
N-Nb_2O_5	monoclinic	C_{2h}^3
Z-Nb_2O_5	monoclinic	C_2^1
R-Nb_2O_5	monoclinic	C_{2h}^3
M-Nb_2O_5	Tetragonal	D_{4h}^{17}
P-Nb_2O_5	Tetragonal	D_4^{10}
TT-Nb_2O_5	Pseudohexagonal or Monoclinic	-

Table 1.1: *Nb_2O_5 polymorph phases together with their crystal system and space group[110].*

For what concerns the crystal structure, most phases are based on the NbO_6 octahedra already identified in the NbO_2 crystal structures. The differences between

Nb_2O_5 phases depend on the linkage between the octahedra. H-Nb_2O_5 is the most stable phase and can be obtained simply by heating in air at T>1000°C any Nb_2O_5 polymorphs or even NbO or NbO_2[130]. H-Nb_2O_5 crystal structure is shown in Figure 1.18 a), as it can be seen from the figure, the NbO_6 octahedra share edges. Figure 1.18 b) shows the crystal structure of N-Nb_2O_5.

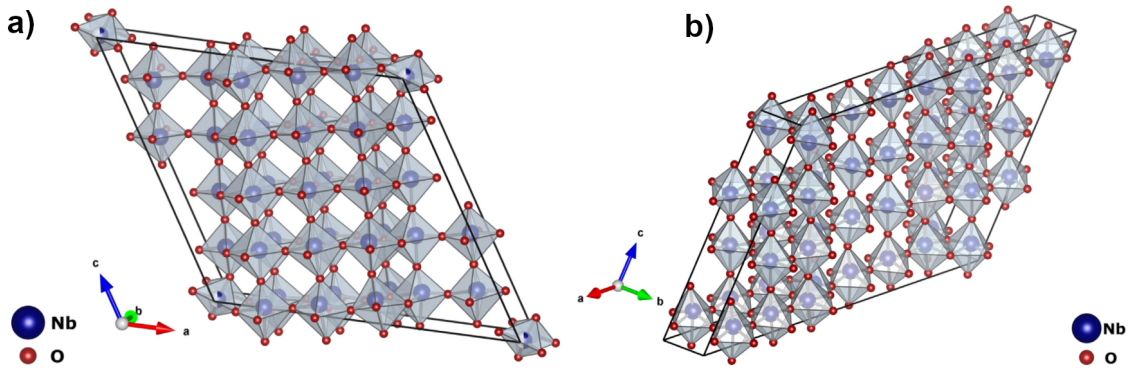

Figure 1.18: *a) Monoclinic structure of H-Nb_2O_5 and b) N-Nb_2O_5[113].*

Nb_2O_5 is used in different applications such as electrolytic capacitors, CMOS devices or MIM capacitors[131]. Nb_2O_5 also possess electrochromic properties, which means the possibility to change colour of a material's thin film by applying a voltage[132]. Another field of interest for Nb_2O_5 is its application in catalysis, in fact its use as a catalyst has been employed to catalyze hydrolysis or alkylation and also for hydrogen storage[133, 134].

Chapter 2

Experimental Techniques

In this chapter, the instrumentation and techniques for growth and characterization of CeO_2 and Nb oxide films will be described.

2.1 Sputtering

Sputtering is a class of deposition techniques and equipments based on the concept of triggering a glow discharge in a chamber filled with ionizable gas[135]. Glow discharge is a plasma created by the current that originates between the anode and the cathode. The two electrodes are placed at an electric potential between each other of hundreds of Volts and the whole chamber environment is filled with a gas at low pressure.

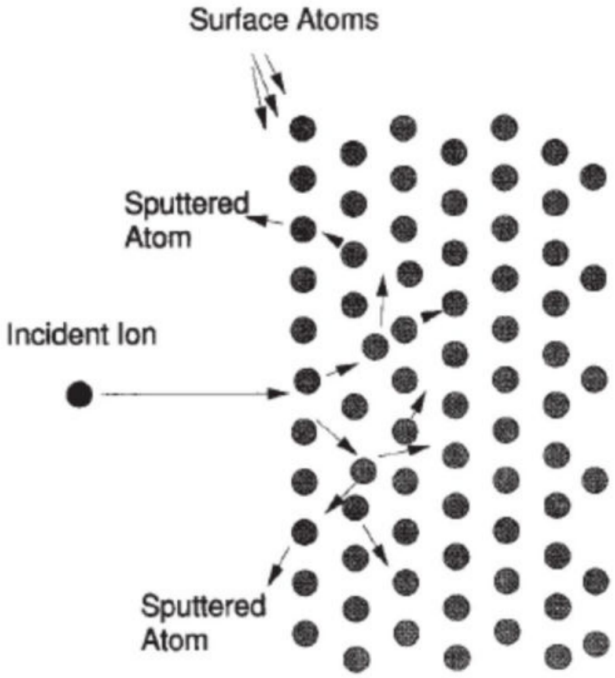

Figure 2.1: *Scheme of the sputtering process happening in the cathode. The gas atom ions collide with the cathode, causing the emission of atoms, that will form the sputtered material[135].*

Few atoms are positively ionized from the beginning by stochastic processes, such

as thermal collisions, and then accelerated by the electric bias towards the cathode, which is called target and is made of the material to be deposited. The collision of the positively charged ions with the target creates secondary electrons which, negatively charged, are accelerated towards the anode, where the substrate for the thin film is placed.
While electrons are travelling towards the anode, they collide with the gas atoms, which are positively ionized and fly towards the cathode, generating other secondary electrons. This cause an avalanche self sustaining process: gas atoms become ionized and generate more secondary electrons in the cathode, which in turn ionize more gas atoms while they fly towards the anode[136]. When the ionized gas atoms collide with the target, together with secondary electrons they cause the emission of negative ions, neutral atoms and molecules, which constitute the sputtering material which will be deposited on the substrate. Figure 2.1 shows a scheme of the sputtering process in the cathode.
The glow discharge avalanche process can be started by using a Direct Current (DC) voltage or a RadioFrequency (RF) one (13.56 MHz). DC is used for metal and conducting targets, while RF is used for insulating ceramic targets. When RF is used, the anode and cathode switch for a short time, in order to avoid charge accumulation on the insulating target.
The gas used to trigger the plasma formation is inert, but a reactive gas, such as oxygen, can be injected in the chamber. The addition of a reactive gas is used to cause chemical reactions in the sputtered material, for example when a metal oxide has to be deposited. This type of deposition is called reactive RF-glow discharge sputtering and it has to be carried on with RF voltage, because oxygen interacts with the metallic targets creating an insulating oxide layer, which can cause the accumulation of charge if instead DC voltage is used.

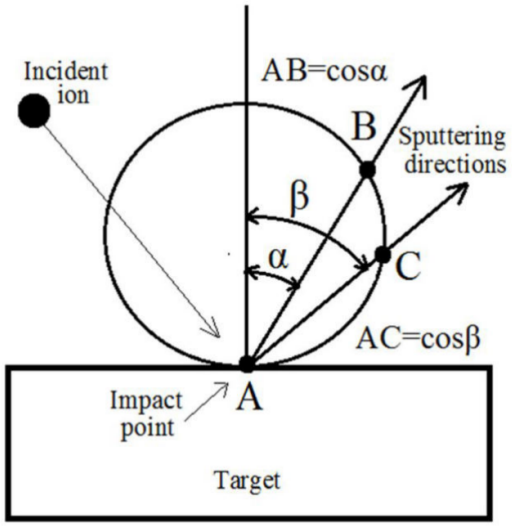

Figure 2.2: *The emission distribution of the sputtered material follows roughly the cosine of the angle of the emission direction[135].*

The amount of sputtered material produced is quantified by the sputtering yield, which is the number of emitted atoms for every incident ion. As shown in Figure 2.2, the emission distribution goes approximately as the cosine of the emission angle. The deposition rate measures the thickness of sputtered material that is deposited

in the unit of time and is measured in Å/s. The deposition time determines how much time is needed, for a set target and sputtering setup, to deposit a defined thickness of sputtered material on the substrate.

2.1.1 Magnetron Sputtering

The need to improve the sputtering process efficiency lead to the birth of modern magnetron sputtering in the 70's[137]. In a magnetron sputtering equipment, a static magnetic field is placed in correspondence to the target, with the $\vec{B}$ lines parallel to the cathode surface and thus perpendicular to $\vec{E}$ between anode and cathode. The secondary electrons generated when the ions impact with the target, suffer the Lorentz Force from the magnetic field and their trajectory is bent. Since the Lorentz force has a direction given by $F_L = \vec{v} \times \vec{B}$ and the velocity of emitted secondary electrons is perpendicular to the target, they are accelerated by $\vec{E}$ towards the anode. This means that the resulting Lorentz Force makes the electrons to move on a trajectory that is confined near the target. This process is schematized in Figure 2.3.

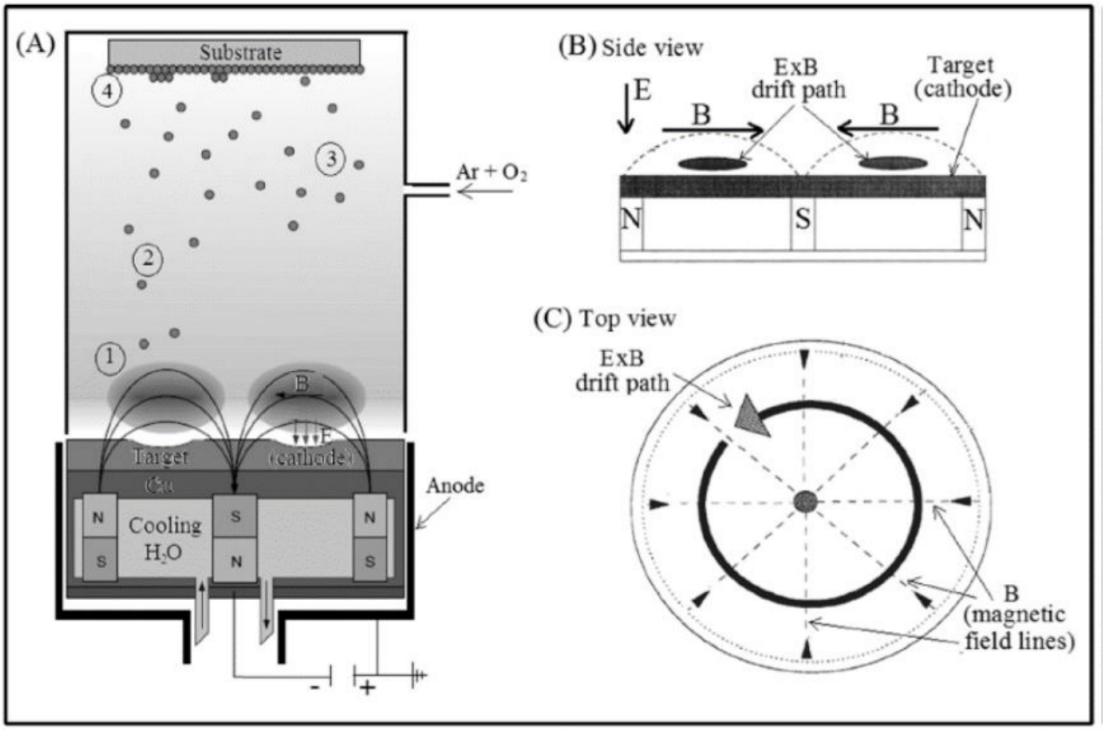

Figure 2.3: *(A) Magnetron sputtering chamber filled with Ar and O_2 gases. The static magnetic field on the target is shown, together with the sputtering material depositing on the substrate.(B) Side view of the target, showing the $\vec{E}$ and $\vec{B}$ fields and the paths followed by secondary electrons, which are affected by the Lorentz force. (C) Top view of the target[135].*

Only the secondary electrons around the target are affected by the Lorentz Force, since the gas and target atoms and ions are too heavy for their trajectory to be influenced by the magnetic field.
This setup gains efficiency compared to normal sputtering because the electron confinement near the target increases the probability for a gas atom near the target to be ionized, thus the plasma density is increased. A higher plasma density leads to more gas ions hitting the target and to more secondary electrons produced.

For the reasons listed above, magnetron sputtering equipment has a higher sputtering yield and deposition rate with respect to sputtering setups without the static magnetic field[138].
Another topic to be considered that influences the sputtering and deposition rates is the one related to the energies of all the atoms and ions involved in the process. The target potential V_T is between 200 V and 800 V, depending on the sputtering setup and target material, while the plasma potential V_P is a bit more positive than the anode potential, which in the majority of setups is close to ground potential[139]. Figure 2.4 shows a scheme of the potentials and particle trajectories inside the magnetron sputtering chamber.

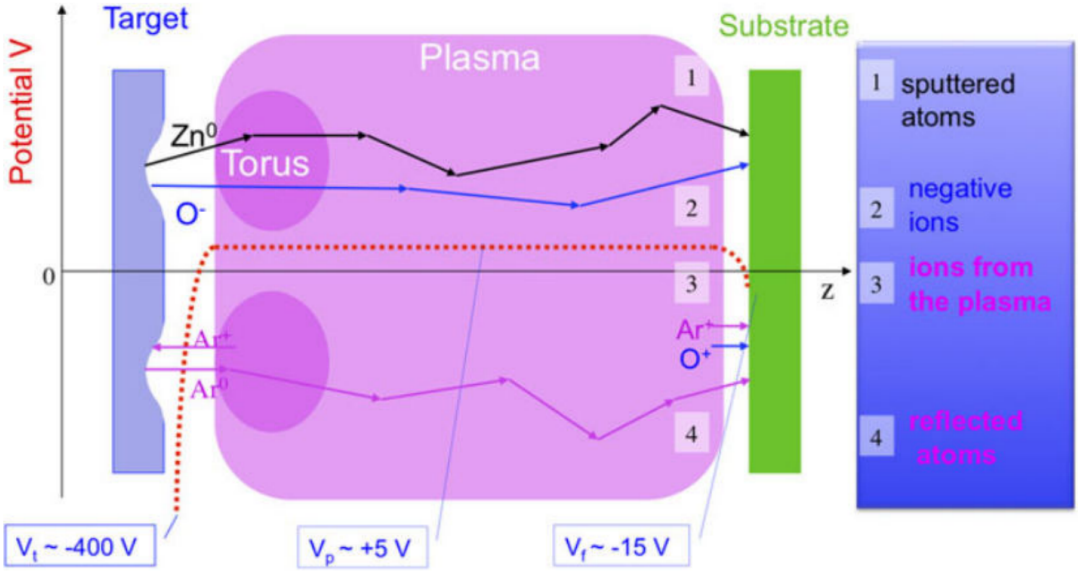

Figure 2.4: *Magnetron sputtering chamber with the potential between the two electrodes. The red dashed line shows the trend of the potential inside the chamber, while the continuous zigzag lines shows the trajectory of the particles listed on the right panel of the image[140].*

Magnetron sputtering geometries

Magnetron sputtering setups can have different geometries depending on their uses and purposes. The most employed are: planar magnetrons, sputtered S-gun and cylindrical magnetron [135].
The planar magnetron sputtering is the most common setup, the target can have a circular or rectangular shape. The circular shape is mostly used in research and for deposition over small areas, while the rectangular shape is more suitable for deposition over large area surfaces and industrial applications. Furthermore, a setup with a moving magnet can improve the utilization of the target, since the circular trajectories paths only erode a small fraction of the target.
In the S-gun configuration the cathode has a conical section. This geometry is particularly suitable to obtain a good uniformity of the deposition by a multiple etch tracks sample. High energy electrons removal and plasma potential correction is carried by the central anode[141]. In cylindrical magnetron sputtering the cathode is inside or outside a cylinder. The anode is a cylinder too, which is coaxial to the cathode. The magnetic field $\vec{B}$ lines are directed along the cylinder, this cause

the electron trajectories to be circles wrapped around the anode, along the cylinder [142]. This setup is primarily used for coating fibers with the sputtered material while they pass through the magnetron.

Sputtering gun setups

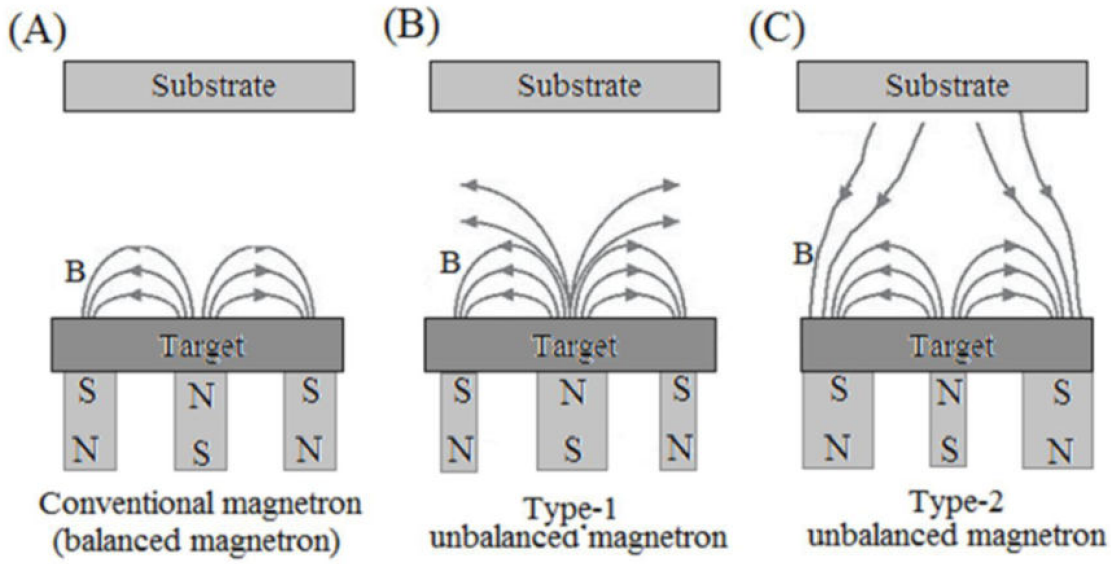

Figure 2.5: *Magnetron sputtering apparatus classified depending on the relative strengths of the central pole with respect to the outer ones.[138].*

Magnetron sputtering machines can also be divided depending on how the magnetic field is distributed inside the chamber.
In balanced magnetron sputtering, as shown in Figure 2.5 (A) the magnetic field lines are confined between the central and outer poles of the magnet and thus the plasma is concentrated in a small region near the target. If the substrate is outside this region, the plasma density around it will be low [137].
The ion flux towards the substrate can be improved in two ways: by increasing the kinetic energy of the ions, which is done by decreasing the electric potential of the anode, or by increasing the number of ions that reach the substrate. The first method is not recommended, as it often produces defects and increases the stress of the films [137], while the second method does not impact the quality of the deposited film and it is obtained by using unbalanced magnetron sputtering setups. In this kind of apparatus, some of the magnetic field lines are not closed between the central and outer poles of the magnets[137].
Unbalanced magnetron sputtering apparatus are divided into two categories.
In type-1, as shown in Figure 2.5 (B), the central magnet is stronger with respect to the external ones. This means that some of the magnetic field lines strike the chamber walls and thus the plasma produced by secondary electrons also strikes the chamber walls. This causes the plasma density near the substrate to be lower with respect to the one of the balanced sputtering apparatus. For this reason, this technique is used just to deposit low density films with a small deposition rate.
In type-2, as shown in Figure 2.5 (C), the external magnets are stronger with respect to the central one. This causes the magnetic field lines to strike the substrate and increase the plasma density in that region. Magnetron sputtering apparatuses of

this type have an ion current flow towards the substrate that is an order of magnitude greater with respect to the one measured in a conventional balanced magnetron sputtering. As a result, the deposited films are denser and more crystalline [137, 138].
Sputtering apparatuses can have more than one target, in order to deposit films or multi layer systems made of different materials. Each sputtering gun can host a target made of a different material, which can sputter at different rates. This setup is called multiple magnetron sputtering [137].

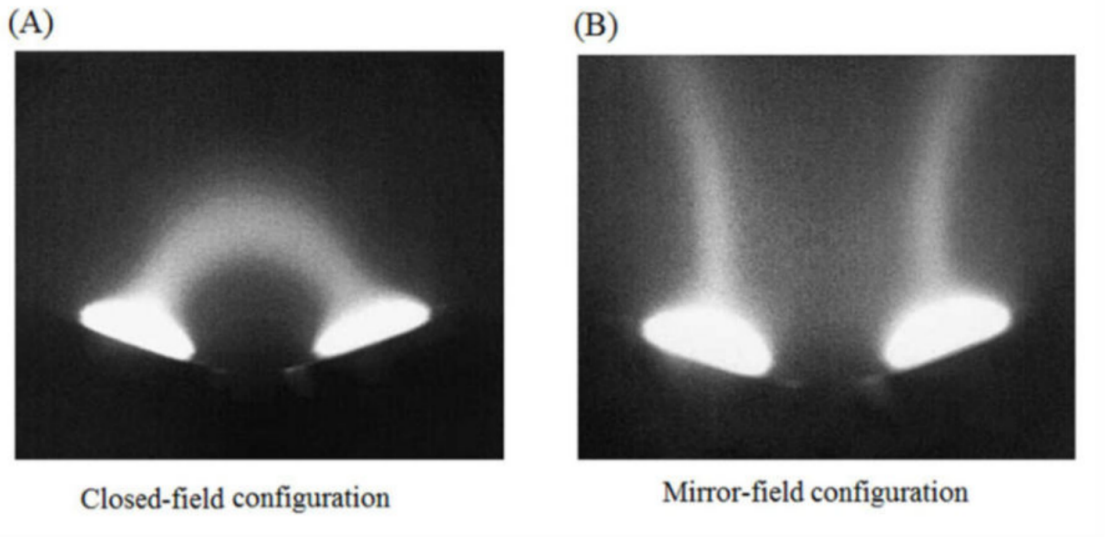

Figure 2.6: *Photos of magnetron sputtering chambers with two targets in the (A) closed and (B) mirror magnetic field configuration.[143].*

These kinds of sputtering chambers, with multiple sputtering guns placed in adjacent positions, can have their targets with identical (mirror-field unbalanced magnetron sputtering) or opposite (closed-field unbalanced magnetron sputtering) polarities of the magnets, as shown in Figure 2.6.
In the mirror configuration, some of the magnetic field lines strike the chamber walls, causing a decrease in the plasma density in the chamber. This effect is not present in the closed field configuration.

Modena magnetron sputtering apparatus

The magnetron sputtering system in Modena that has been used to deposit the samples is a Moorfield magnetron sputtering chamber. The exterior of the chamber is shown in Figure 2.7 a), while Figure 2.7 b) shows the inside of the chamber.
The apparatus has three unbalanced type-2 sputtering guns, in mirror-field configuration, suited for 3 inches targets. The bias between anode and cathode can be applied by both DC and RF power. DC is powered by two Glassman LP 600-2 DC-generators (0±600 V, 0±2 A), while RF is applied by one Seren RF-generator at 13.56 MHZ. The necessary vacuum level is obtained thanks to a turbomolecular pump and a scroll pump mounted in series and the base pressure is measured by a Pirani and a Penning pressure sensors. A base pressure of about 1×10^{-6} *mbar* is reached thanks to the pumps.
The total working gas pressure of about 7 mbar is imposed manually, measured by a low pressure gauge Baratron and kept fixed by a down-stream butterfly valve. Two

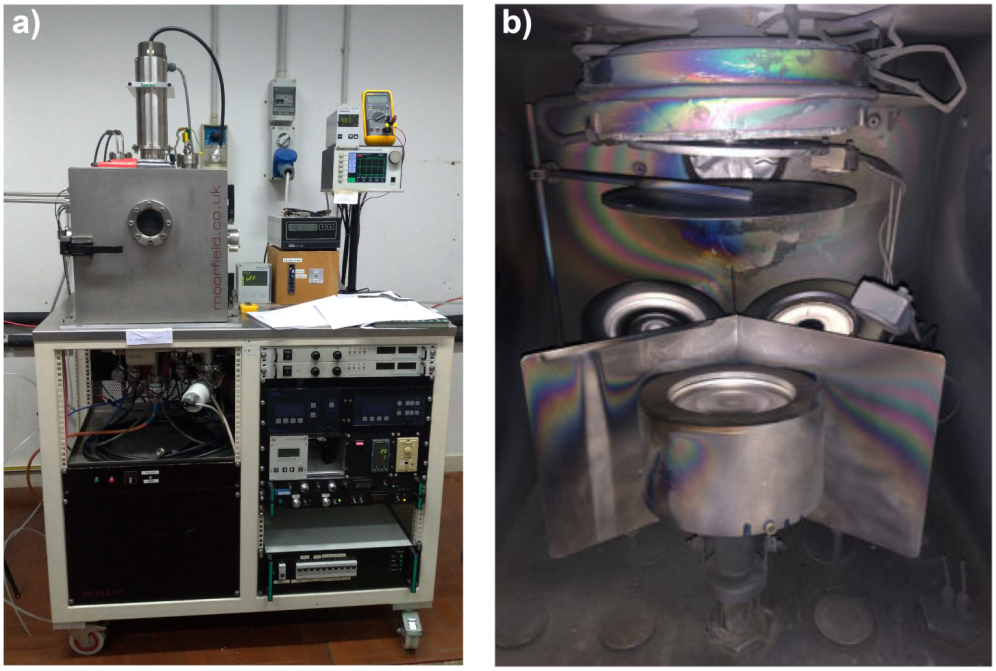

Figure 2.7: *Photo of the a) exterior and b) interior of the magnetron sputtering apparatus in Modena.*

mass flow controllers guarantee a maximum oxygen and argon flow of 20 sccm. The removable sample holder can rotate at 12 rpm to make more homogeneous the deposition. The deposition rate is monitored by a quartz microbalance. A resistive heater is placed on the backside of the sample holder to heat the substrate and the temperature of the sample stage is controlled by a calibrated thermocouple.

2.2 SESAMo Laboratories

XPS characterization and post-growth treatments of the samples described in this thesis have been performed in *Electronic Spectroscopies on Surfaces and Adsorbates laboratory in Modena* (SESAMo). The apparatus used is called RAGNO-1 and is an Ultra High Vacuum (UHV) system for the growth and characterization of thin films and nanoparticles.
RAGNO-1 is schematized in Figure 2.8 and is divided into three main UHV chambers: the Molecular Beam Epitaxy (MBE) chamber, the main chamber and the STM/AFM chamber. All these chambers are kept at a pressure of $\sim 10^{-10}$ mbar and are connected (light purple tubes in the Figure 2.8). This allows the growth and the characterization of the samples in-situ while keeping the specimen in UHV conditions. As it can be seen in Figure 2.8, the RAGNO-1 apparatus also have a fast entry minichamber. The fast entry allows to load the substrates from ambient pressure, is evacuated at $\sim 10^{-6}$ mbar by a scroll and a turbo pump and then the valve connecting it with the main chamber is opened, allowing to transfer the samples from the external into the main chamber in a short time without affecting the UHV of the main chamber.
The MBE chamber purpose is the deposition of thin films and nanoparticles through Molecular Beam Epitaxy. The chamber is equipped with many MBE evaporators, each one of them is able to effuse an element. The elements that can be deposited

include Ag, Ce, Au, and Cu. Moreover, the chamber is equipped with a quartz microbalance, to monitor the thickness of the grown samples, and with a gas line, that can modify the composition of the deposition atmosphere, allowing for example to obtain metal oxides by depositing the metal. A resistive heater is also mounted onto the sample holder, giving the possibility to vary the substrate temperature.
The main chamber is dedicated to substrate preparation and sample chemical characterization. It can perform X-Ray Photoelectron Spectroscopy (XPS), Ultraviolet Photoelectron Spectroscopy (UPS), and Low-Energy Electron Diffraction (LEED). For these purposes, the chamber is equipped with a sputtering stage (for substrate cleaning), a concentric hemispherical analyzer (OMICRON EA 125), a double-anode Leybold-Heraesus X-Ray source for XPS, and a Helium lamp for UPS. As in the case of MBE, it is possible to heat the sample with a heater in order to perform post-growth treatments, including oxydation and reduction cycles in a partial pressure of O_2 or H_2 (maximum 10^{-6} mbar).
Finally, the third chamber is dedicated to morphological characterization, and it contains a room temperature (RT) scanning probe microscope for Scanning Tunneling Microscopy (STM) and Atomic Force Microscopy (AFM).

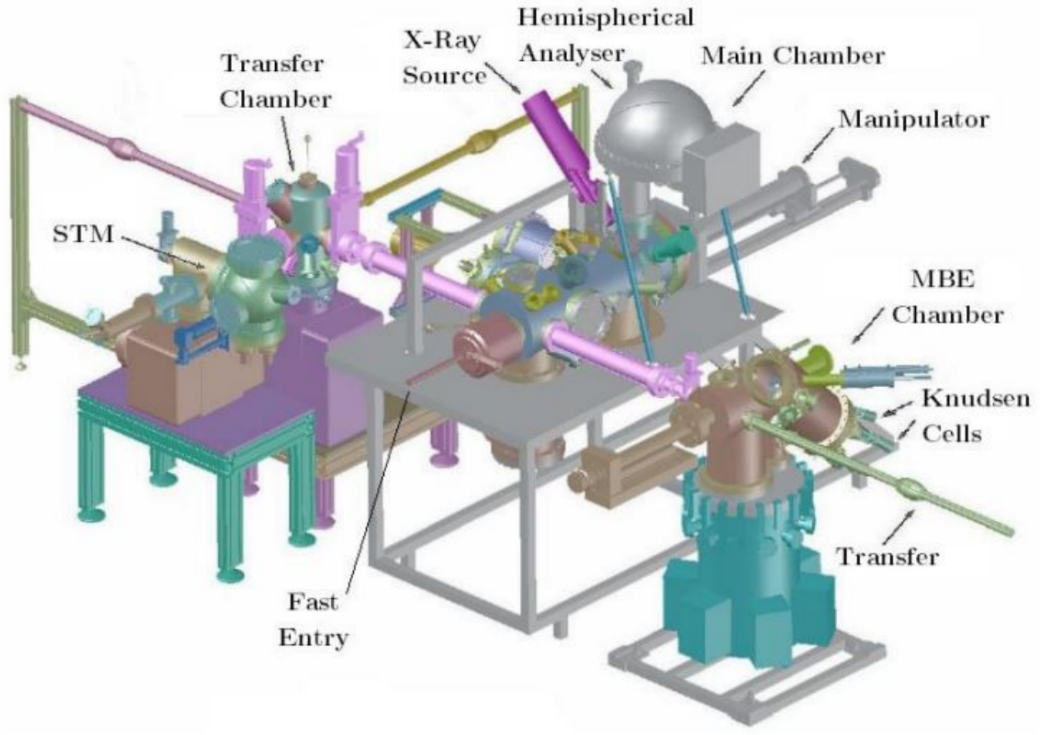

Figure 2.8: *Scheme of the RAGNO-1 apparatus showing the three main chambers and related equipment.*

2.3 Free Electron Laser

Free Electron Lasers (FELs) are new generation synchrotron radiation (SR) sources, where the light is produced by optical amplification, as a standard visible laser[144]. However, if in a standard laser the process used for optical amplification is the quantum stimulated emission[145], in a FEL the SR generation mechanism is classical with relativistic effects.

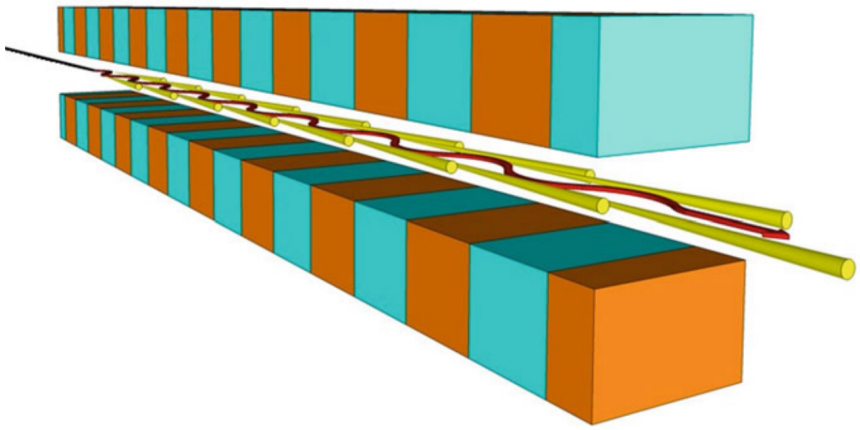

Figure 2.9: *Scheme of the undulator behaviour: the electrons (red arrow) travel in between the two arrays of magnets in the undulator and start oscillating. At each oscillation the elctrons emit SR (yellow light cones)[144].*

The main part of an FEL is the undulator. An undulator is a device constituted by an array of permanent magnets with alternating polarities, as shown in Figure 2.9. When the electrons travel between the two magnet arrays, they start oscillating and emitting SR radiation at each oscillation[146]. This principle is employed also in standard synchrotron facilities, where the SR originating from the electrons oscillation are collected and directed to a beamline[147].

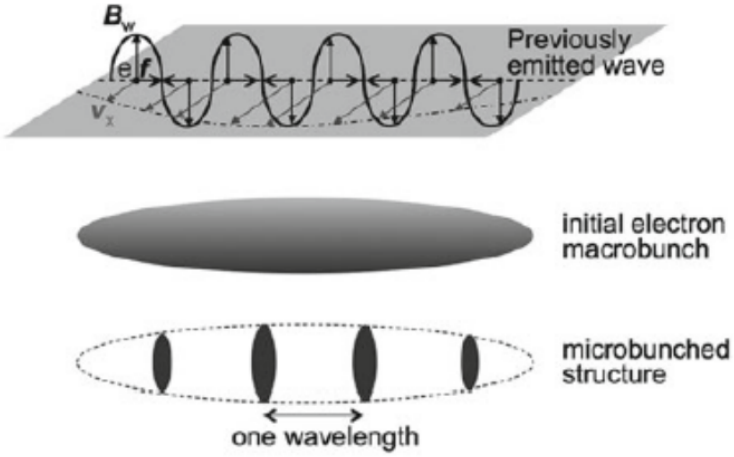

Figure 2.10: *Process of electron microbunching in an undulator, in which the initial electron macrobunch is divided in microbunches, each one of them distant one wavelength from the others[144].*

However in a FEL, another effect occurs: the SR emitted by the electrons starts to

interact with the electrons themselves. In particular, the transverse magnetic field $\vec{B}$ of the emitted SR interacts with the transverse electron velocity $\vec{v}$, causing the electrons to suffer a longitudinal Lorentz Force $\vec{F_L}$[148, 144]. Electrons in synchrotron radiation facilities are emitted and travel in bunches around the accumulation ring, as shown in the middle panel of Figure 2.10. The Lorentz force causes the electrons in the macrobunch to shift along the longitudinal direction and, as shown in the top panel of Figure 2.10, the only position where the Lorentz force is zero is at the nodes of the emitted SR and that causes the electrons to accumulate in the nodes of the wave[148, 144]. The final result is that, as shown in the bottom panel of Figure 2.10, the initial electron macrobunch is divided in microbunches, with a distance between each other of one wavelength[148, 144].

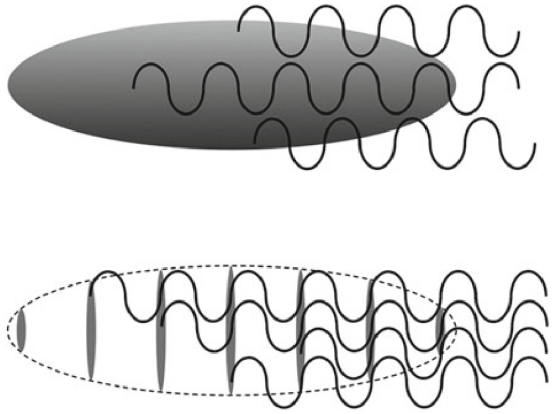

Figure 2.11: *Top: electrons in a macrobunch emit uncorrelated waves, bottom: if microbunching occurs the emitted waves are in phase and the SR intensity is amplified [144].*

In a normal undulator without microbunching, as shown in the top panel of Figure 2.11, SR waves are not emitted in phase and thus the intensities of the waves emitted by each electron are summed. If there are N electrons, the intensity I in an undulator is proportional to the number of electrons $I \propto N$. Instead, if microbunching occurs, all the SR waves emitted by each electron in the microbunches are in phase, as shown in the bottom panel of Figure 2.11. The waves themselves are combined together and, since for each wave $|\vec{E}|$ and $|\vec{B}|$ are proportional to N, then the intensity of the wave, which is proportional to $|\vec{E}|^2$, is also proportional to N^2 or $I \propto N^2$.
This causes the intensity of SR generated by FELs to be up to seven orders of magnitude greater than storage ring SR sources, as it can be seen in Figure 2.12, where the peak brilliance of storage rings such as ESRF or PETRA is compared with the one of FEL facilities such as XFEL, LCLS or FLASH.
The other main advantage in FELs, is that they produce ultrashort pulses of SR, with a duration from few tens to hundreds of femtoseconds[150]. The production of ultrashort intense SR pulses is crucial for ultrafast spectroscopies, which rely on short light pulses in order to study photoinduced dynamic processes in matter[151]. Infrared FELs were the first to be designed and constructed, as an optical cavity can be used to amplify the emitted waves until saturation is reached. However, this is not possible for X-rays, since the normal incidence reflectivity at X-rays wavelength is extremely low. This means that the optical amplification must occur in

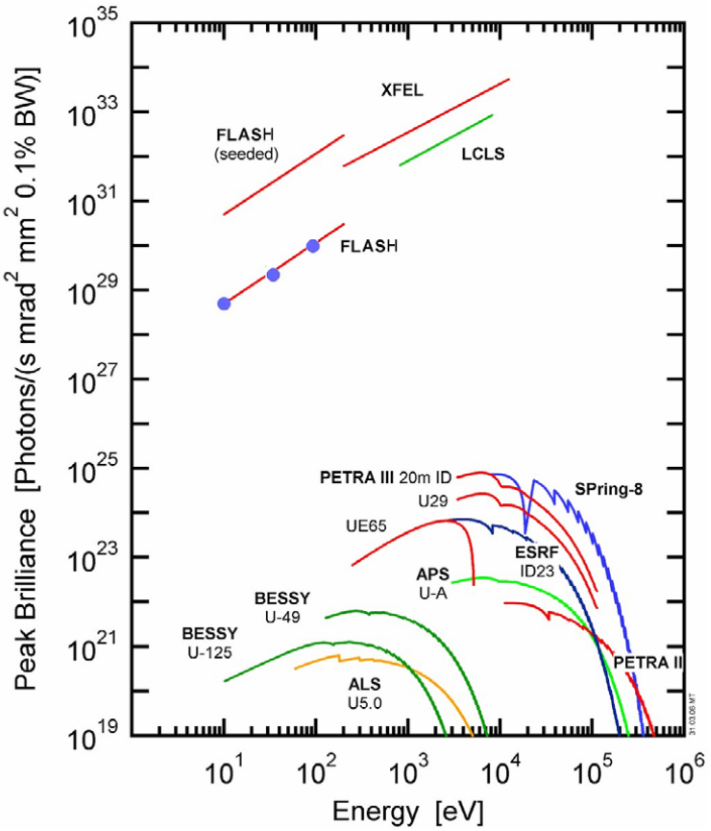

Figure 2.12: *Peak SR brilliance obtained from storage rings and FEL facilities is compared. Peak brilliance of FELs is order of magnitude greater than storage rings[149].*

one passage. However, these obstacles has been overcome, as now X-ray Free Electron Lasers (XFELs) such as the European XFEL in Hamburg, Germany or LCLS in Stanford, US are realities[144].

2.3.1 European XFEL

The European XFEL (EuXFEL) is an international center of excellence for X-ray Free Electron Lasers experiments. The first X-ray pulses were produced in May 2017 and the facility started user operation in September 2017[152].

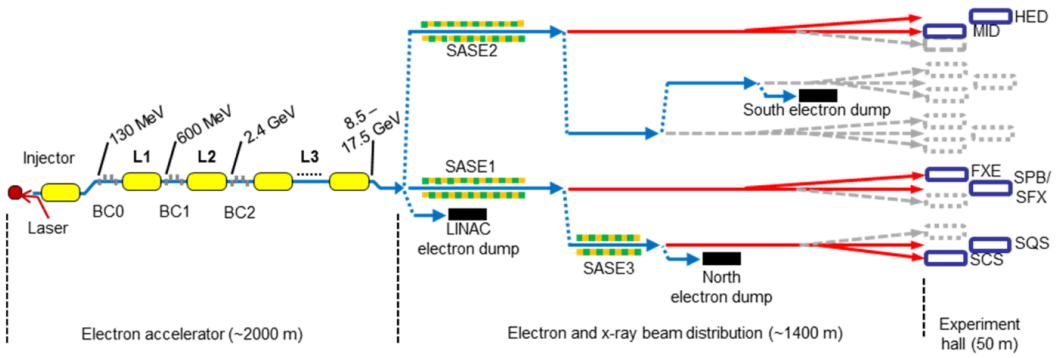

Figure 2.13: *Scheme of the European XFEL showing the linear accelerators, the three SASEs and the experimental halls where the X-ray pulses are directed[153].*

The electron beam is accelerated to a final energy of up to 17.5 GeV [154] and then, when it arrives to the experimental area it is split in branches in order to be fed to three SASEs undulators that generate the X-rays[155]. The three SASEs serve a total of 8 beamlines, each one with different equipment specialized in a different type of experiments. The final X-ray pulses are ultrashort (< 100 fs) and with a frequency of up to 27000 pulses/s (2700 pulses in 10 Hz burst) [156, 157]. Figure 2.13 shows a scheme of the European XFEL SASE undulators and the eight experiment halls where the X-ray pulses are collected and employed. Each experimental hall take the name of "scientific instrument", even if they are equipped with more than one kind of apparatus.

The FXE scientific instrument

The pump-probe measurements described in this thesis have been performed at the Femtosecond X-ray Experiments (FXE) beamline at the EuXFEL.
X-ray pulses are provided to FXE by the SASE1 undulator, as shown in Figure 2.13. The photon energy available for experiments range from 5 to 20 KeV, enabling the study of wide range of dynamic processes in liquid and solid materials[158]. While the X-ray beam acts as a probe, an ultrafast optical laser acts as a pump to generate excited states in the sample and is synchronized with the X-ray pulse time structure[159]. The optical laser can emit photons from the UV-Visible up to the near-IR range[158].
The following spectroscopies and measurements can be performed at FXE[160]:

- X-ray diffraction (XRD)
- X-ray diffuse scattering (XDS) or wide-angle X-ray scattering (WAXS)
- X-ray emission spectroscopies (XES): non-resonant, or resonant inelastic X-ray scattering (RIXS)
- X-ray absorption spectroscopies: X-ray absorption near-edge structure (XANES), or extended X-ray absorption fine structure (EXAFS)

In order to perform these kind of measurements different instruments are available in the experimental hutch. In order to perform XES experiment, two X-ray emission spectrometers are available: a dispersive X-ray emission spectrometer, based on a von Hamos design[161], and a scanning spectrometer, based on the Johann geometry[162]. These two spectrometers can be utilized in combination with the following detectors: CCD cameras, a Jungfrau 2D [163] or a Gotthard 1D strip [164]. The Large Pixel Detector (LPD) is instead used for X-ray solution scattering (XSS) or XRD. Large area Photodiodes are available for measuring the fluorescence in XAS measurements. In the experiments described in this thesis, the Von Hamos Spectrometer and a photodiode have been used.

The area in the experimental hutch where the sample is placed is showed in Figure 2.14: on top there's an orange robotic arm that can hold various detectors and is needed to align them to the emission energy dispersed by the spectrometer, under the arm lies the stage where the sample is placed. The Johann and Von Hamos Spectrometers can be seen in the figure on the left and on the right with respect to the sample stage respectively. Behind the stage, the LPD detector can be found. The sample stage setup shown in Figure 2.14 is the one for liquid samples.

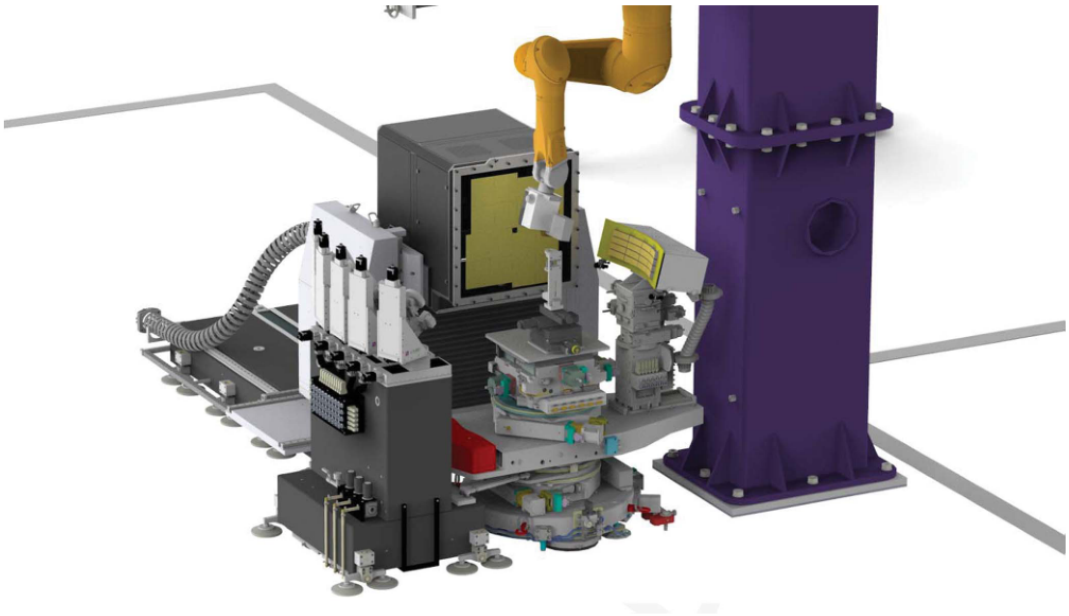

Figure 2.14: *3D render of the sample interaction area at FXE. The Von Hamos (right) and Johann(left) spectrometers are visible, together with the robotic arm (top) and LPD (behind the sample stage). [158].*

The X-ray beam in the FXE beamline passes through the air and no vacuum tube is employed to transport the beam in the experimental hutch. However, Helium purging can be used in case of oxidation-sensitive samples. In the experiment described in this thesis, helium purging has been used to minimize X-ray absorption from air. Solid samples are mounted on a Kappa goniometer: it allows to set incidence angle and sample translation on a 50×50 mm range to reduce beam damage during the measurement acquisition[158]. When a solid sample is mounted, the volume in which pump (optical laser) and probe (X-ray FEL pulse) interact must stay on the sample surface.

2.4 Pump-probe ultrafast spectroscopy

Pump-probe technique, which was born in 1899 thanks to Abraham and Lemoine [165], uses two synchronous light pulses with the same time structure: a "pump" pulse which generates a photoinduced transition in the sample and a "probe" pulse, which performs a measurement or a spectroscopy on the sample, usually absorption or reflection spectroscopies[166]. Figure 2.15 shows the scheme of a pump-probe experiment.

These experimental techniques are used to study molecular and atomic processes in real time, which require a time resolution of tens of femtoseconds [168]. Electronic processes in atoms require an even higher resolution, with light pulses in the attosecond range [169]. Lasers capable of producing pulses with a femtosecond resolution are available since the beginning of 2000's [170] and the attoseconds barrier has been recently shattered [169].
Femtosecond transient absorption spectroscopy (FTAS) is a time-resolved pump-probe technique used to study ultrafast processes in atoms and with sensitivity to local atomic structure (if the probe pulse performs EXAFS measurements)[171]. In

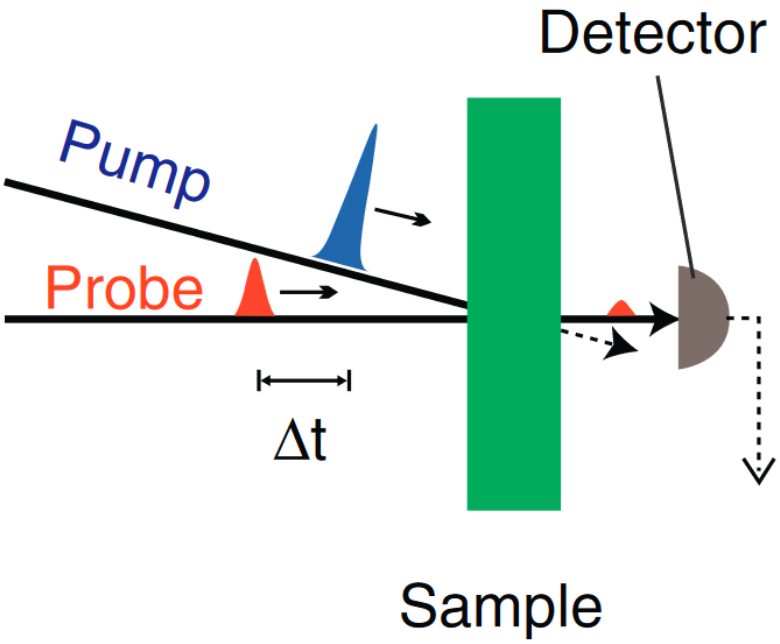

Figure 2.15: *Scheme of a pump-probe experiment, showing the two light pulses that interact with the sample [167].*

this experimental technique, the probe pulse measure the absorbance of the sample after a time delay τ between the pump and the probe. The absorption measured by the probe signal is acquired in presence (A_{on}) and in absence (A_{off}) of the pump pulse, in this way it is possible to evaluate the samples' response modification after the pump excitation. The absorption difference ΔA is then calculated:

$$\Delta A = A_{on} - A_{off} \tag{2.1}$$

In FTAS both the pump and the probe pulses are UV-visible[172]. However, thanks to the recent construction of XFELs capable to generate ultrafast X-ray pulses, pump-probe experiments employing a visible pump and an X-ray probe are possible[173]. In this kind of experiments, X-ray Absorption (XAS) and X-ray Emission (XES) spectroscopies can be performed by the probe X-ray pulse. The spectra are measured with the pump switched on and off and the difference on-off can be measured as a function of the time delay between pump-probe while keeping the probe photon energy constant, or as a function of the probe energy while keeping the pump-probe time delay constant[174].

2.5 APE beamline at Elettra Synchrotron

The Advanced Photoelectric Effect (APE) experiment is a beamline operating at the Elettra Synchrotron in Trieste[175]. SR photons are emitted by two collinear undulators and sent to two separate branches, which are able to work independently[175]. The first one employs Low Energy (LE) photons with an energy between 10 and 100 eV and is called APE-LE, while the second one uses higher energy (HE) photons with an energy between 140 and 1500 eV and is called APE-HE. Figure 2.16 shows a scheme of the two branches at APE beamline

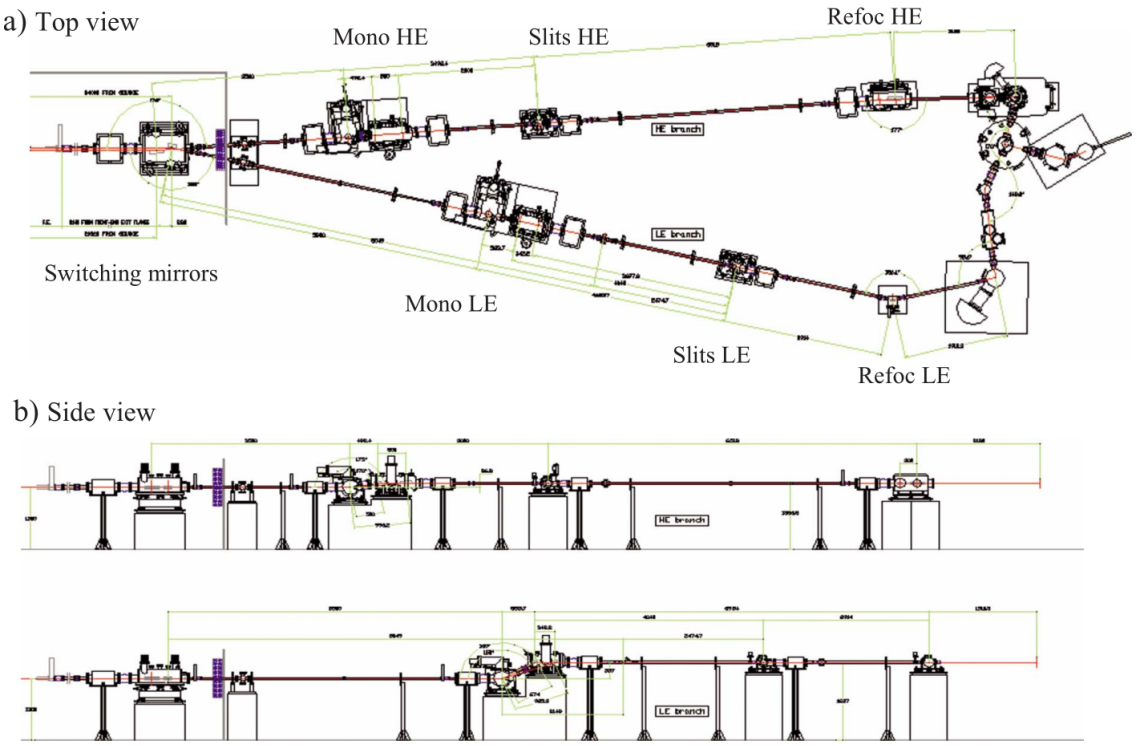

Figure 2.16: *a) top and b) side view of the APE beamline showing the two branches APE-HE and APE-LE, together with their optics[175].*

The experiment that will be described in this thesis was performed at the APE-HE branch. The photons used in the branch are generated by an APPLE-II type undulator which can provide both linearly and circularly polarized light. The polarization can be modified by tuning the vertical gap and the longitudinal phase between the two magnetic arrays. APE-HE focuses mainly on XAS, XPS and X-ray magnetic circular dichroism (XMCD) experiments.

2.5.1 Reaction cell for ambient pressure XAS

In operando spectroscopies have the purpose to study chemical reactions in realistic conditions, i.e. catalysis in ambient pressure instead of in an UHV environment[176]. The first systems capable to provide these measurements used photons in the hard X-rays range, due to the high penetration of radiation in this energy range. Near ambient pressure X-ray Photoemission spectroscopy (NAP-XPS) equipments use electron analyzers with differential pumping, but were limited to pressures near the

sample in the mbar range[177]. In the late 90s the first equipments for near ambient XAS were developed, however they were limited to a pressure of few mbars[178, 179]. Nowadays, due to the development of high quality, few nms thick SiN membranes, setups for Ambient Pressure XAS (AP-XAS) are available at synchrotron radiation facilities[180].

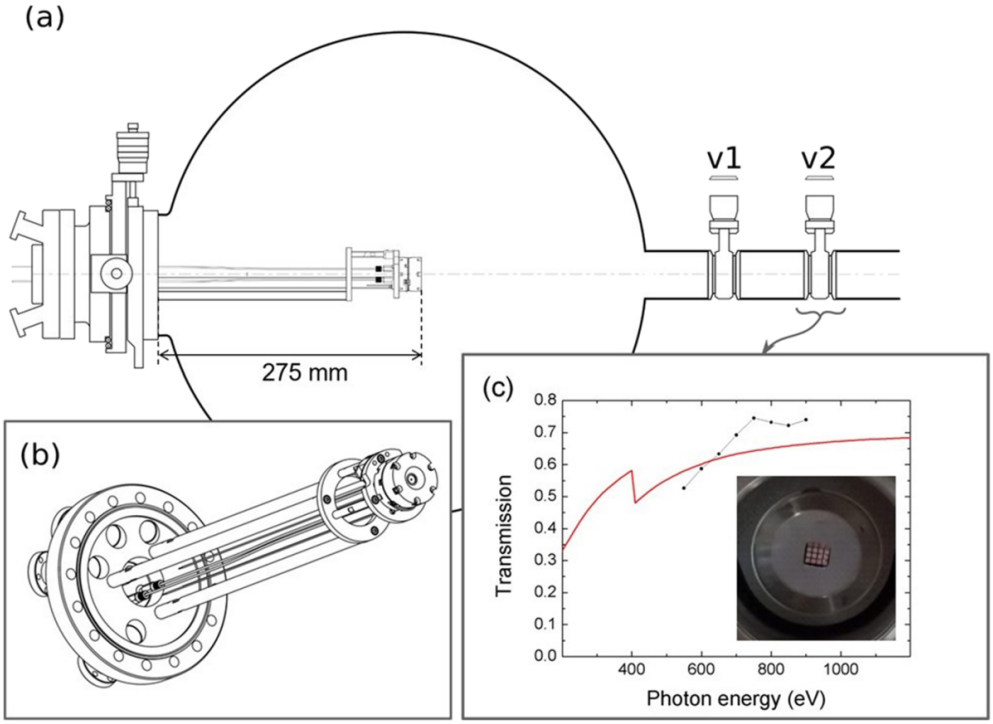

Figure 2.17: *a) Reaction cell placed inside the chamber showing the two valves V_1 and V_2, b) 3D render of the reaction cell and c) measured (black dots) and estimated (red line) X-ray transmission of the membrane arrays in V_2. The inset of the graph shows a picture of the membrane array[181].*

The reaction cell employed for the experiment at APE-HE beamline in Elettra was developed in 2018 and allows to perform AP-XAS measurements[181]. The ambient pressure reaction cell is inserted at the end of the UHV chamber at APE-HE. Figure 2.17 a) shows a schematic of the APE-HE end station and Figure 2.17 b) shows a 3D render of the reaction cell. As it can be seen from Figure 2.17 a), the cell is placed inside the chamber along the direction of the X-ray beam. Furthermore, the cell can be moved on the plane perpendicular to the X-ray beam to align the membrane with the X-ray beam. V_1 and V_2 in Figure 2.17 a) are two UHV gate valves that separates the chamber from the rest of the beamline. V_1 is a standard gate valve that is closed when the chamber is vented before the cell is inserted. V_2 has an X-ray window made of a 4×4 matrix of Si_3N_4 membranes, each membrane is 1 mm × 1 mm large and 50 nm thick. The X-ray transmission of the membranes array in V_2 is shown in Figure 2.17 c) and the graph inset shows a picture of V_2 with the membranes. The membranes in V_2 allows the X-ray beam to reach the sample while keeping the chamber and the rest of the beamline isolated, acting as a security measure in case the membrane in the photocatalytic cell is damaged.

Figure 2.18 shows a drawing of the cross section of the reaction cell. The sample is highlighted in green and is placed in a small volume enclosed by the Si_3N_4 membrane

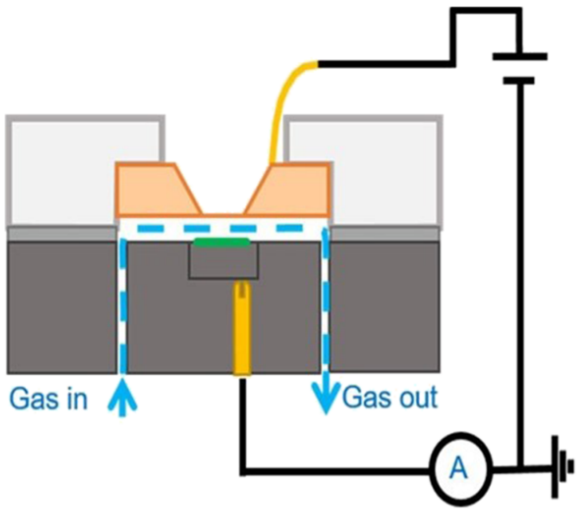

Figure 2.18: *Cross section drawing of the top part of the reaction cell, showing the interaction volume between sample and membrane and the electrical contacts. Adapted from [181].*

(colored in orange) where the photocatalytic reactions occur. The membrane is 500×500 μm in size and 100 nm thickness, is glued to the cell by the use of silver conductive paste together with an electrical contact. The contact allows to apply a potential bias between the membrane and the sample. A gas inlet can inject gases in the volume between the sample and the membrane and the produced gases are collected by an outlet, as shown by the light blue path in Figure 2.18. A 3D render of the top part of the reaction cell is shown in Figure 2.19 a), while a vertical section of the cell is shown in Figure 2.19 b). As it can be seen from Figure 2.19 a) the top part of the cell (containing the membrane) and the bottom part (containing the sample) are separated by ceramic spacers. As shown in Figure 2.19 b), the cell contains also a heater placed below the sample, which allows to increase the temperature in the reaction volume from room temperature up to 300°C.

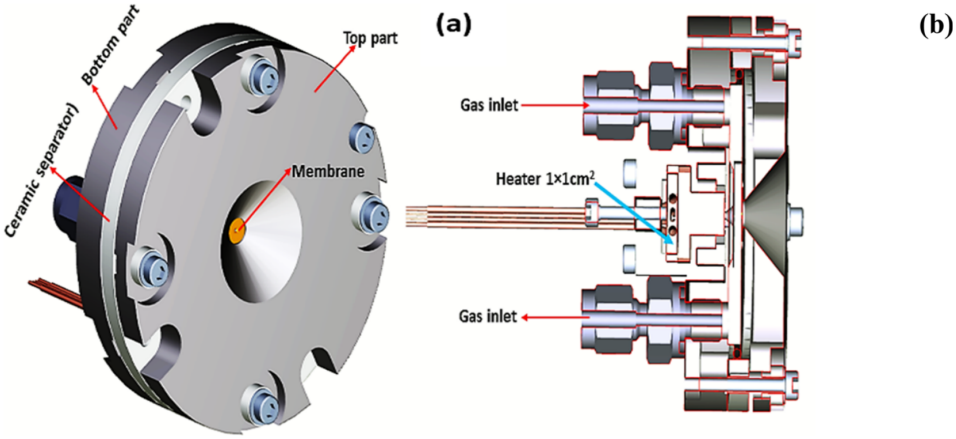

Figure 2.19: *a) 3D render of the reaction cell top part, showing the separator between the membrane and the sample. b) Cross section of reaction cell's top part, showing the gan inlets and the heater[182].*

When the cell is placed inside the chamber and aligned with the X-ray beam, the photons pass through the membrane and are absorbed by the sample. Secondary electrons (SE) are then emitted by the sample and their current is proportional to the X-ray absorption from the sample, this current is called Total Electron Yield (TEY). In order to measure the SE current, two electrodes are placed are shown in Figure 2.18: one on the membrane and one on the sample. The electrode on the membrane is used to apply a voltage bias between membrane and sample. The SE emitted during the experiment are accelerated by the bias towards the membrane. The electrode placed on the sample allows to measure the sample drain current, which then can be used to calculate the TEY.

Chapter 3

Results

3.1 Optimization of magnetron sputtering grown ceria films

As stated in the previous chapter, Magnetron Sputtering (MS) is a deposition technique used to grow films that can be relatively thicker with respect to those grown using other physical deposition techniques. Furthermore the material is deposited uniformly over a larger area. In order to perform pump-probe experiments on ceria, the CeO_2 film thickness needs to be larger and spread over a larger substrate area than what was achievable with the MBE apparatus in the Ragno-1 UHV chamber at SESAMo lab. For this reason, MS was chosen as the most suitable technique to obtain ceria films with a stoichiometry as close as possible to CeO_2, i.e. to 100% Ce^{4+} ions concentration.
The MS deposition studies are performed by growing 80 nm thick ceria films on Si and quartz substrates. The deposited thickness was measured by a quartz microbalance and then calibrated by measuring a test deposition with a profilometer. The Si substrates are (10x10) mm^2 square cut from a wafer made by a 0.3 mm thick Si (100) layer with a 600 nm thick SiO_2 thermal oxide layer on top. This substrate is used for the XPS, XRD and SEM measurements. The quartz substrates consist in (10x10) mm^2 substrates of UV-grade fused silica 0.3 mm thick used for optical absorption measurements. The samples for the pump-probe measurements were deposited on sapphire Al_2O_3 substrates with a diameter of 25.4 mm substrate 0.5 mm or 0.3 mm thick. Sapphire has been chosen because pump-probe measurements require a transparent substrate, which can transmit rapidly the heat generated from the beam. A sample with a large area is required in order to scan undamaged areas of the sample in case of beam damage.
The parameters changed during the different depositions were:

- The temperature T of the substrate during growth
- The flow ratio $\frac{O_2}{Ar + O_2}$ between oxygen and the sum between oxygen and argon flow inside the chamber
- The power P of the RadioFrequency (RF)

Table 3.1 shows the parameters used for each deposition.

The MS apparatus can accommodate multiple samples in its sample holder, so in each deposition a Si and a quartz substrate was used.

Sample	substrate T	$\frac{O_2}{Ar+O_2}$ flow	RF Power [W]
CeO_2#001	RT	0%	100
CeO_2#002	RT	50%	100
CeO_2#003	RT	75%	100
CeO_2#004	RT	75%	150
CeO_2#005	200°C	75%	150
CeO_2#006	300°C	75%	150

Table 3.1: *Deposition parameters for the MS-grown ceria samples*

Before inserting the substrates in the MS chamber for the deposition, it is necessary to clean them. This is achieved by putting each substrate in acetone bath for 5 minutes at 150°C on a hot plate, followed by a bath in an ultrasonic cleaner washer in acetone and then in isopropyl alcohol at 80°C for 3 minutes.
The substrates are then inserted into the MS apparatus and the chamber is pumped by a scroll and a turbomolecular pump until it reaches an internal pressure of 10^{-6} $mbar$. Then the deposition can start by flooding the chamber with Ar until it reaches an internal pressure of 5×10^{-6} $mbar$. If needed, O_2 can also be supplied in order to obtain more oxidized samples. The deposition can then be started by switching on the radiofrequency at the desired power.
As it will be explained later, the growth parameters that gave the best results are the ones used for the CeO_2#006 sample, for this reason the samples grown on sapphire discs used during the pump probe experiment were grown with the same growth parameters.

3.1.1 XPS measurements

Samples grown with different growth parameters were characterized by XPS in order to determine the oxidation state of the CeO_2 films.

XPS spectra qualitative analysis

Figure 3.1 shows Ce 3d XPS spectra of the different samples grown with a different ratio of oxygen flow over the total gas flow in the chamber. The spectra have been acquired in normal emission mode. The spectra were all shifted in binding energy due to sample charging, so in the following graphs the peak at higher binding energy of each spectrum was aligned at the binding energy of 916.9 eV. This energy corresponds to the one reported in [183] for a CeO_2 powder reference. After the first XPS measurement on CeO_2#001, the sample was annealed in a UHV chamber at 500°C at a partial oxygen pressure P=1.33×10^{-7} $mbar$ for 30 minutes, in order to verify if the oxidation state of the sample would be influenced by post-deposition annealing in an oxidizing environment.

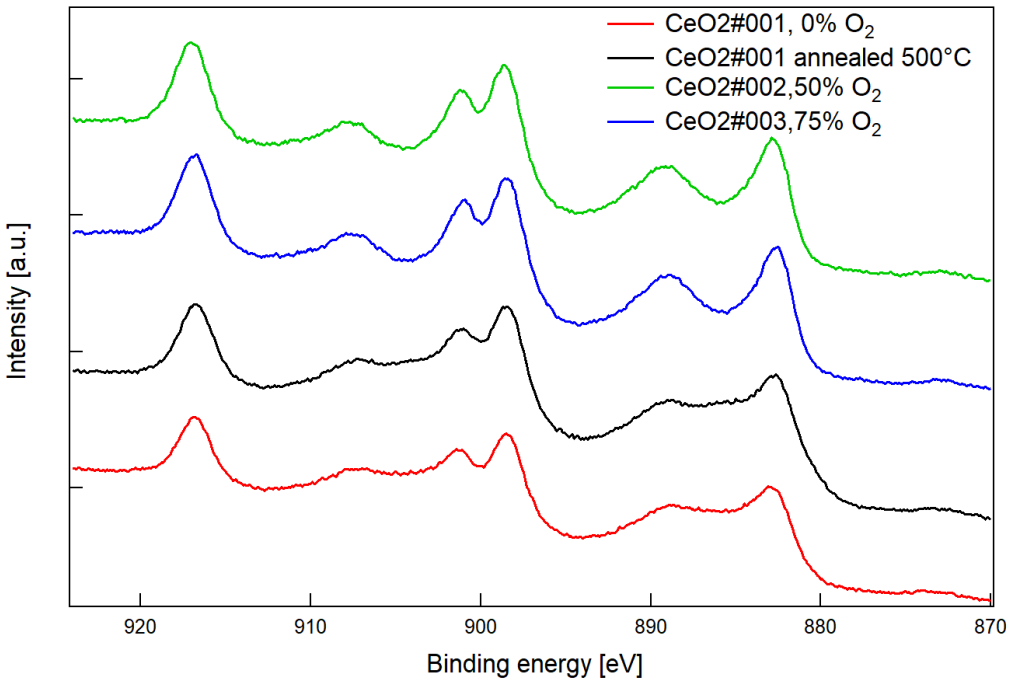

Figure 3.1: *Ce 3d XPS spectra of the MS-grown CeO_2 samples at different oxygen flow during deposition.*

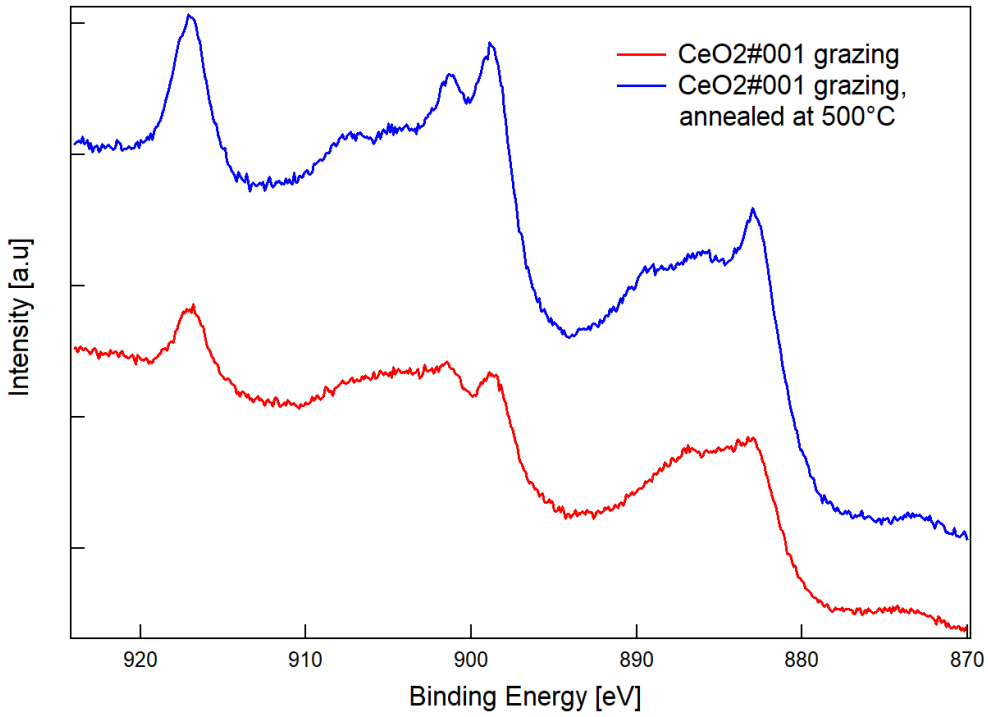

Figure 3.2: *Ce 3d XPS spectra of the MS-grown CeO_2 sample CeO_2#001 measured at grazing emission. The two spectra represent the samples as grown (red line) and after being annealed at 500°C in oxidizing environment (blue line).*

By looking at Figure 3.1, it can be seen that the annealing in oxygen has produced no changes in the XPS peak positions and intensities in the sample CeO_2#001, meaning that the annealing in oxygen is uneffective in changing the oxidation state of the sample. This is probably due to the thickness of the samples: an ultrathin film (few nm thickness) of CeO_2 can be easily oxidized or reduced by thermal treatments in an oxidizing or reducing environment[184], however these films are 80 nm thick and they possibly require much more time or a higher oxygen partial pressure in order to obtain the same result as the ultrathin films.
In order to verify if the first atomic layers of the sample had changed their oxidation state due to the annealing in oxygen, XPS spectra have also been acquired at grazing emission. Figure 3.2 shows the Ce 3d spectra acquired at grazing emission of the sample CeO_2#001 as grown and annealed at 500°C.
By looking at Figure 3.2 it can be seen that the two spectra are indeed different. In particular, the annealed sample shows the peaks at 882 and 890 eV, which are related to Ce^{4+}[183, 185], more defined than the as-grown sample, suggesting that the surface of the sample has been oxidized by the annealing treatment.
Going back to Figure 3.1, the sample looks progressively more oxidized as the oxygen flow ratio $\frac{O_2}{Ar+O_2}$ increases, as the peaks related to Ce^{4+} ions appear more intense and defined. A quantification of the Ce^{4+} content in each sample will be given in the following section, where the Ce 3d XPS spectra will be fitted to obtain the Ce^{4+} concentration.

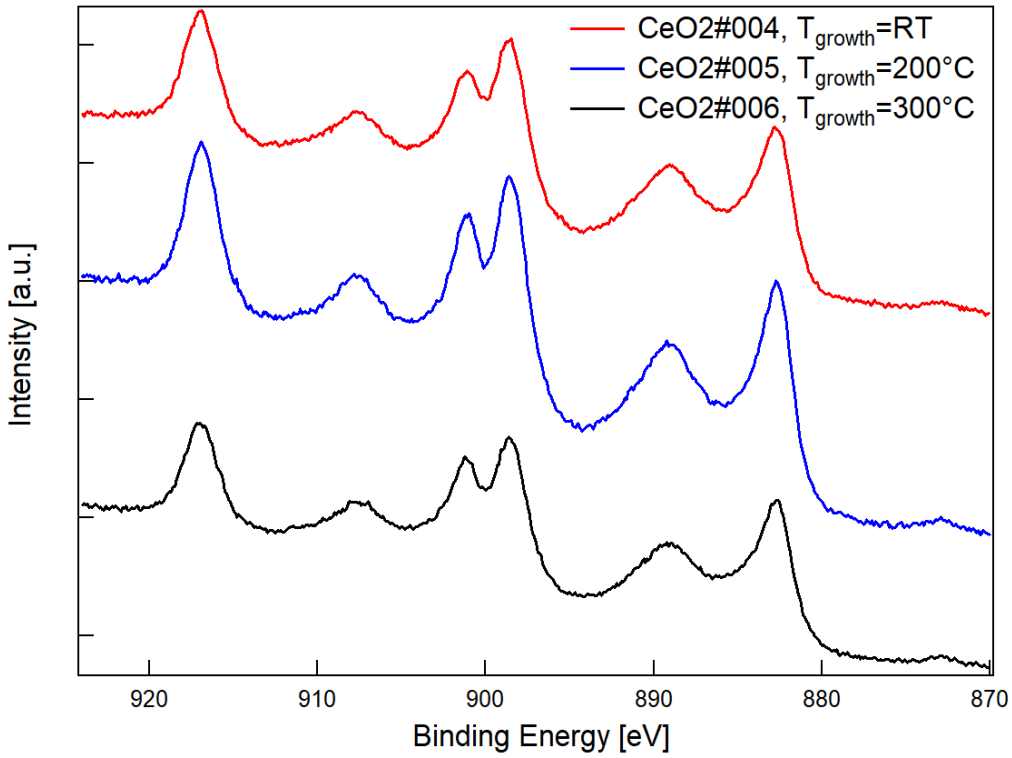

Figure 3.3: *Ce 3d XPS spectra of the MS-grown CeO_2 sample at different substrate temperature.*

Figure 3.3 shows the Ce 3d XPS spectra of samples grown at different temperatures of the substrate. As it can be seen in Figure 3.3, the overall shape of the spectra and the relative intensities of the peaks do not change between the spectra, suggesting that changing the substrate temperature during growth has no effect over the Ce^{4+}

concentration in the CeO_2 layer. Figure 3.4 shows Ce 3d XPS spectra of samples grown with a different RF power. In particular, CeO_2#003 has been grown with a RF power of 100 W, while CeO_2#004 with a RF power of 150 W. By looking at Figure 3.4, it can be seen that, as in the previous case, the two XPS spectra show no differences in peaks' positions or relative intensities, meaning that RF power has no impact over the oxidation state of ceria films. RF power has been increased in order to reduce time required for the deposition. In fact by increasing the RF power from 100 to 150 W, the deposition rate has doubled, passing from 0.08 Å/s to 0.16 Å/s.

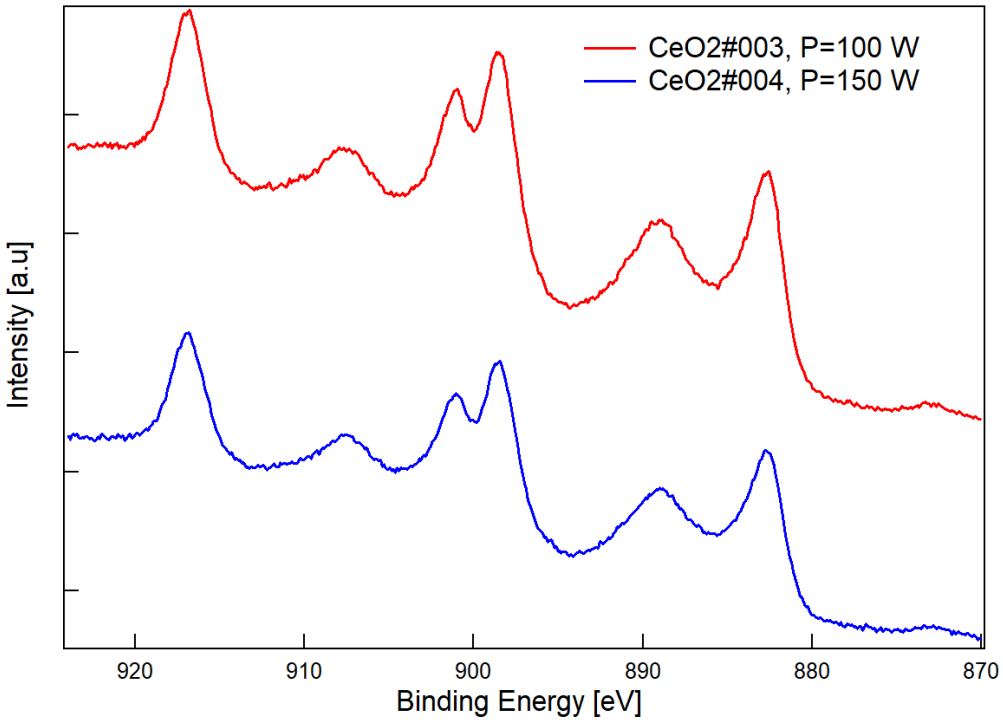

Figure 3.4: *Ce 3d XPS spectra of the MS-grown CeO_2 samples at different RF power.*

Ce 3d XPS spectra peak fitting

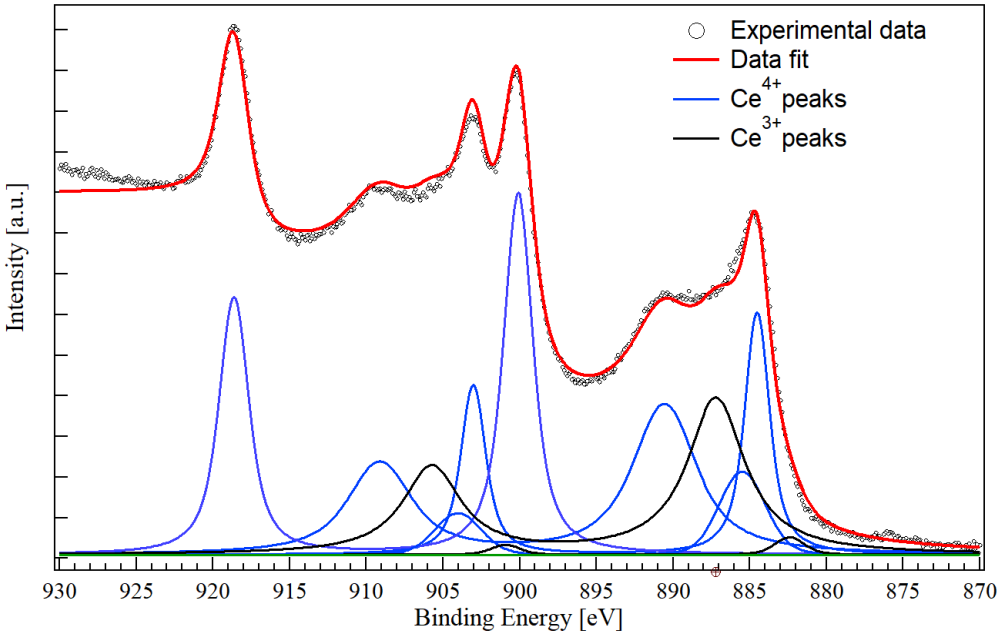

Figure 3.5: *Example of a fit performed on the Ce 3d XPS spectrum. the white circles represent the acquired data, while the red line is the fit result.*

The Ce 3d XPS spectra were then fitted by using a program that evaluates the concentration of Ce^{3+} and Ce^{4+} ions. The fit procedure and peak parameters are taken from the work by Skala et al. [186, 187]. Figure 3.5 shows an example of the fit perfromed on a Ce 3d XPS spectrum. The fit consists in six Doniach-Sunijch peak doublets, four of them are related to the Ce^{4+} phase (blue peaks in Figure 3.5), while two of them are related to the Ce^{3+} phase (black peaks in Figure 3.5).
For each peak doublet, the following parameters are considered:

- The doublet area
- The binding energy of one of the peaks in the doublet
- The Full Width at Half Maximum of the peaks
- The branching ratio, which represents the intensity ratio between the two peaks in the doublet
- The spin-orbit coupling, which represents the distance in binding energies between the two peaks.

Each parameter can be fixed or left free to be evaluated by the fitting procedure. The concentration of Ce^{3+} (or Ce^{4+}) is obtained by dividing the area of the peaks related to Ce^{3+} (or Ce^{4+}) by the total area.
Figure 3.6 shows the Ce 3d XPS spectra of the samples grown at different oxygen percentage in the MS chamber and the corresponding fit. The different components contributing to the fit are also shown.

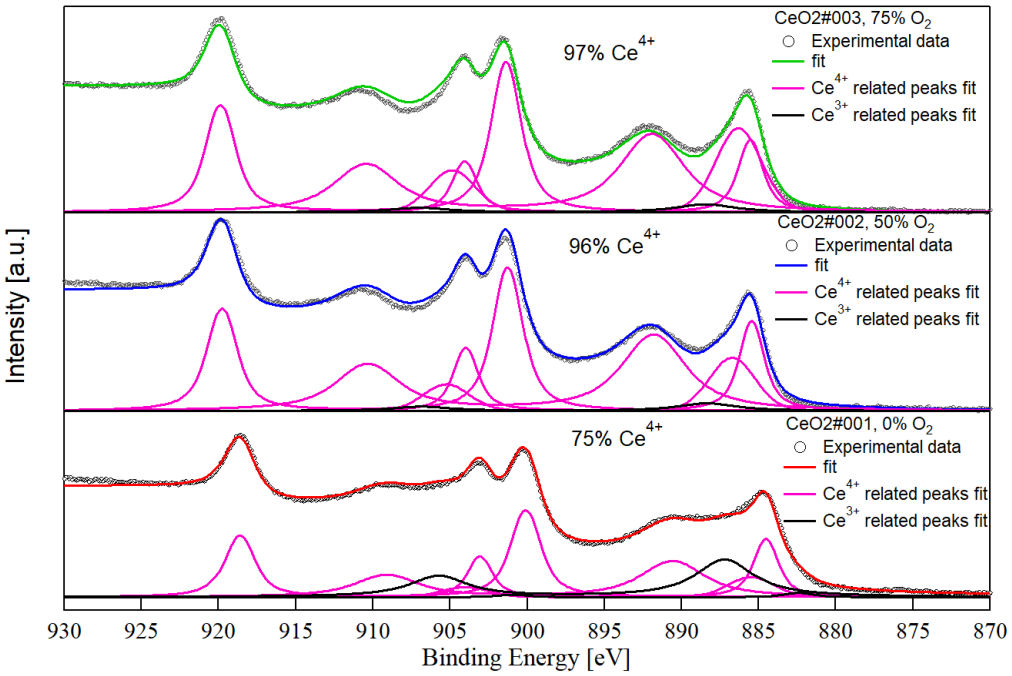

Figure 3.6: *Ce 3d XPS spectra peak fitting performed on the samples grown with a different O_2 relative flow in the chamber. For each spectrum, the fit for each peak and the total fit is shown, together with the obtained Ce^{4+} ions concentration*

As it can be seen in Figure 3.6, CeO_2#001 spectrum is quite different from the other two. In fact, by performing the fit, the Ce^{3+} related peaks (black line in the Figure) have an area comparable with one of the Ce^{4+} related peaks (magenta line in the Figure) and are clearly visible. Instead, the Ce^{3+} related peaks in CeO_2#002 and CeO_2#003 spectra cannot be seen in the Figure, due to their low intensity. The fit gave the following results: CeO_2#001 has $75 \pm 1\%$ of its Ce atoms in the Ce^{4+} oxidation state, while for CeO_2#002 and CeO_2#003 the Ce^{4+} concentration are $96 \pm 1\%$ and $97 \pm 1\%$ respectively.

Figure 3.7 shows the fits of the Ce3d spectra acquired on the samples grown at different temperatures. CeO_2#004 has a Ce^{4+} concentration of $98 \pm 1\%$, while CeO_2#005 and CeO_2#006 of $99 \pm 1\%$. The Ce^{4+} obtained for all samples is contained within the error range assigned to the fit, meaning that temperature increase has no relevant influence on the detected surface stoichiometry.

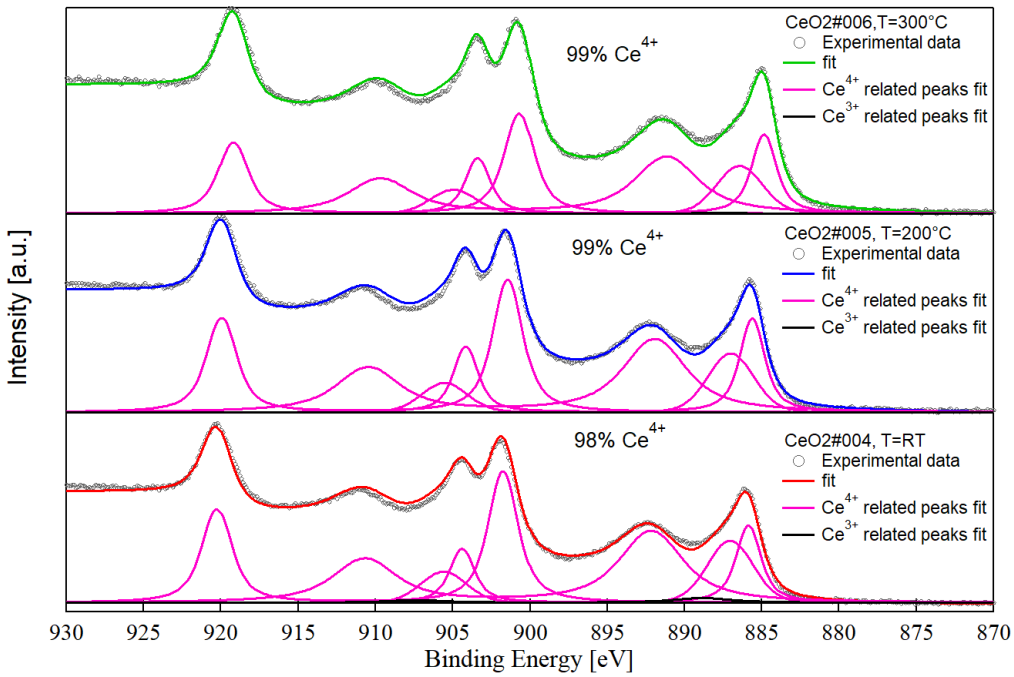

Figure 3.7: *Ce 3d XPS spectra peak fitting performed on the samples grown at different temperatures. For each spectrum, the fit components and the total fit are shown, together with the obtained Ce^{4+} concentration*

3.1.2 UV-Visible absorption measurements

CeO_2 layers grown on quartz and sapphire have been investigated by UV-Visible absorption spectroscopy in order to obtain the optical properties in the visible and near-UV range. It is important to know the band gap absorption wavelength of the samples because, during the pump probe experiments, the band gap of CeO_2 is excited. Furthermore, the study of optical properties is complementary to the study of surface stoichiometry, since light absorption in the optical range is influenced by the stoichiometry and defects in the bulk of the samples.
The UV-Visible absorptance spectra have been acquired in S polarization at an incidence angle between the light beam and the sample normal of 22°. The incident light wavelength was scanned from 275 to 750 nm with a resolution of 2 nm. In order to obtain the absorptance, a spectrum of the light impinging directly on the photodiode without the sample in between, called I_{tot} was initially measured. Then the sample is placed between the polarizer and the detector and the trasmitted light spectrum T_{sample} is measured. Then the detector is moved in correspondence to the reflected beam and the reflected light spectrum R_{sample} is measured.
After the data acquisition, the reflectance R and the transmittance T are calculated as:

$$R = \frac{R_{sample}}{I_{tot}} \qquad T = \frac{T_{sample}}{I_{tot}}$$

Finally the Absorptance A is calculated as:

$$A = 1 - T - R$$

Figure 3.8 shows the optical absorptance spectra of the samples CeO_2#001, CeO_2#002 and CeO_2#003 grown using different O_2 relative flows.
As it can be seen in Figure 3.8, all the absorptance spectra have a maximum in correspondence of the wavelength of $\sim 320\ nm$. The absorption peak becomes narrower

as the oxygen flow in the chamber increases. This can be explained by the fact that samples grown with lower oxygen flow contain a non-negligible quantity of Ce^{3+} ions. Figure 3.9 shows the optical absorbance spectra of the samples CeO_2#004, CeO_2#005 and CeO_2#006 grown at different temperatures. As shown in Figure 3.9, all the samples have the absorption peak at the same wavelength. The peak is slightly less intense for the samples grown at higher temperatures, probably due to small variations in thickness and morphology during deposition.

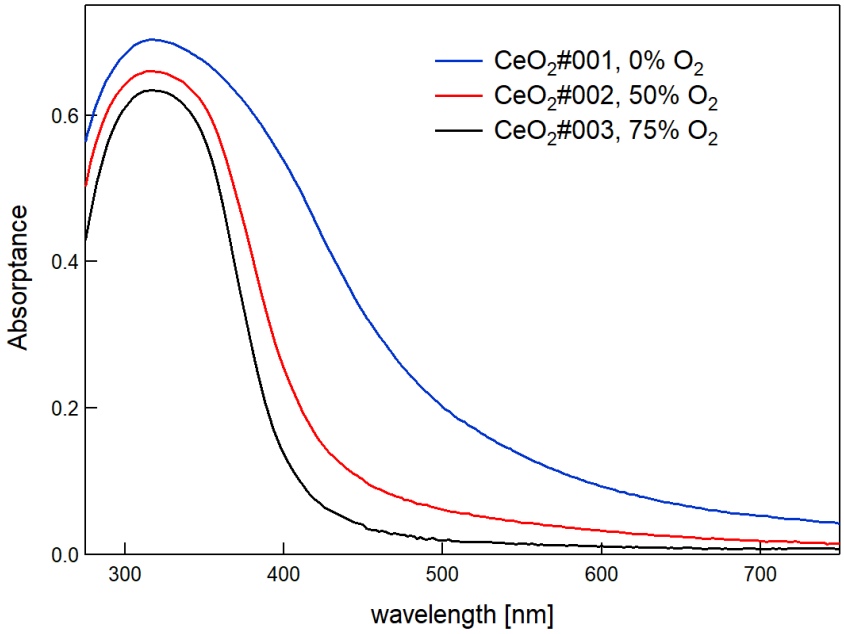

Figure 3.8: *Optical absorption spectra of the MS-grown CeO_2 samples grown in different oxygen flow during deposition.*

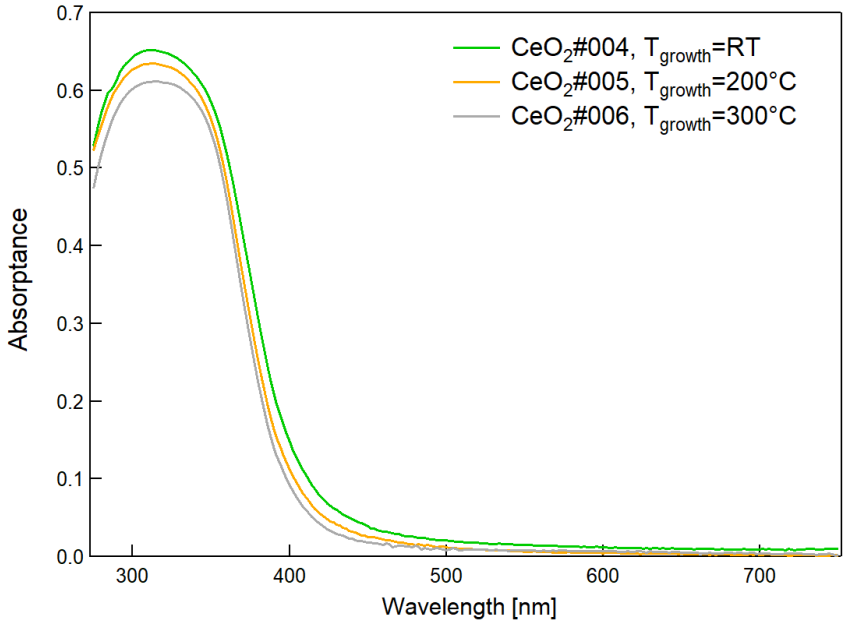

Figure 3.9: *Optical absorption spectra of the MS-grown CeO_2 samples at different substrate temperature during growth.*

Figure 3.10 shows the optical absorbance spectra of the samples CeO_2#003 and CeO_2#004. The spectra shown in Figure 3.10 show almost no differences: the absorption peaks have similar widths and intensities. This behaviour can be explained by the fact that the RF power simply increases the speed of deposition without altering the characteristics of the deposited sample, thus changing the RF power has no effect on the optical properties. Figure 3.11 shows the optical absorption spectra of CeO_2#006, which has a thickness of 80 nm and of two CeO_2 samples grown by MBE: one 8 nm thick and the other one 4 nm thick. From Figure 3.11 it can be seen that the absorption peak in the case of MBE-grown samples has a lower intensity than the one related to the MS-grown sample. This behaviour can be simply explained with the lower thickness of the MBE-grown samples with respect to the MS-grown ones. Furthermore, the absorption peak maximum is slightly shifted to lower wavelengths in the case of the MBE-grown samples, as the two samples grown by MBE have the maximum at 300 nm, while the MS-grown samples have the absorption maximum at 320 nm. This can be explained by the fact that films grown by magnetron sputtering are thicker, but contain more defects than the one grown by MBE. This causes the MS-grown samples to absorb light at higher wavelengths from electronic states related to defects.

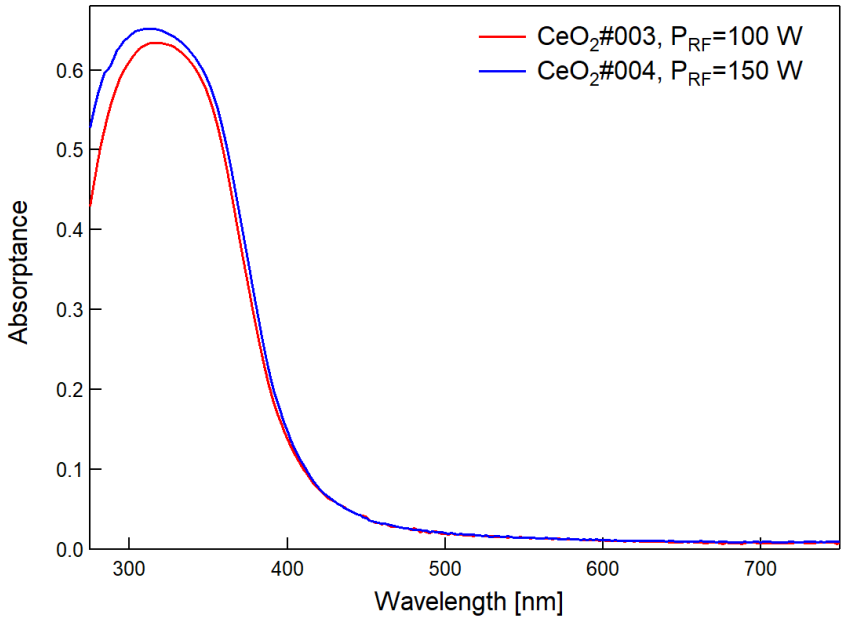

Figure 3.10: *Optical absorption spectra of the MS-grown CeO_2 samples at different Radio Frequency power used in the growth.*

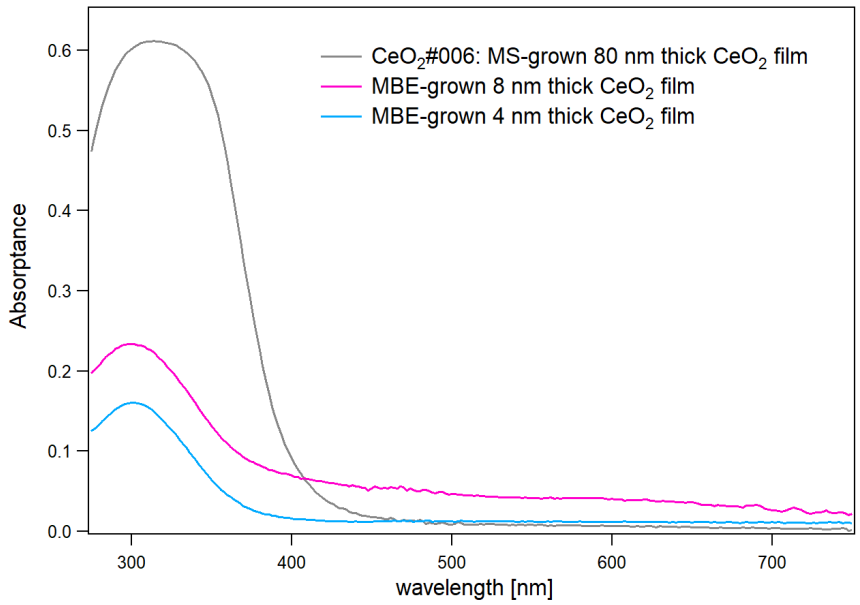

Figure 3.11: *Optical absorption spectra of the MS-grown sample CeO_2#006 and of two MBE-grown samples.*

In order to obtain an estimate of the band gap of the grown samples, the optical spectroscopy data have been used to build a tauc plot.
Tauc plot is a method to obtain the band gap of a semiconductor[188]. It is based on the assumption that the absorption coefficient α can be expressed as:

$$(\alpha\ h\nu)^{1/\gamma} = B\,(h\nu - E_g) \tag{3.1}$$

where $h\nu$ is the photon energy of the light in the optical spectrum, B is a constant and E_g is the band gap of the material[189, 190]. γ is a factor that is equal to 2 for direct and $\frac{1}{2}$ for indirect band gap transitions[191].
By using equation 3.1, it is then possible to obtain E_g by constructing a graph in which $(\alpha\ h\nu)^{1/2}$ is plotted as a function of $h\nu$. The obtained graph has a distinct linear region on the absorption edge, which can be fitted with a linear equation of the type:

$$y = a + bx \tag{3.2}$$

where in this case $y = (\alpha\ h\nu)^{1/2}$ and $x = h\nu$. For direct transitions, E_g is identified by the abscissa corresponding to $y = 0$ in equation 3.2, or by the point in which the line with equation 3.2 intersects the horizontal axis[192]. This means that, in order to obtain E_g from the tauc plot it is sufficient to calculate:

$$E_g = -\frac{a}{b} \tag{3.3}$$

where a and b are the fit coefficients from equation 3.2.
The absorption coefficient $\alpha(h\nu)$ has been obtained by using the Beer-Lambert law, which describes the attenuation suffered by light when it traverses a medium:

$$I_t = I_0 e^{-\alpha(h\nu)d} \tag{3.4}$$

where I_0 is the light intensity before traveling through the medium, I_t is the light intensity transmitted by the sample, $\alpha(h\nu)$ is the absorption coefficient as a function of the photon energy and d is the thickness of the sample[193, 194].

I_0 in equation 3.4 represents the total incoming radiation intensity if reflection doesn't occur. However, in the case of thin films measured through optical spectroscopy, reflectance isn't negligible in the photon energy range considered. This means that for ceria samples, I_0 represents:

$$I_0 = I_{tot}\,(1 - R) \tag{3.5}$$

By substituting equation 3.5 into equation 3.4 and remembering that:

$$T = \frac{I_t}{I_{tot}} \qquad I_t = T\ I_{tot}$$

Equation 3.4 can be rewritten as:

$$\begin{aligned} I_t &= I_{tot}\,(1 - R)\,e^{-\alpha(h\nu)d} \\ T\ I_{tot} &= I_{tot}\,(1 - R)\,e^{-\alpha(h\nu)d} \\ e^{-\alpha(h\nu)d} &= \frac{T}{1 - R} \qquad \alpha(h\nu)d = -\ln\left(\frac{T}{1 - R}\right) \\ \alpha(h\nu) &= -\frac{1}{d}\ln\left(\frac{T}{1 - R}\right) = \frac{1}{d}\ln\left(\frac{1 - R}{T}\right) \end{aligned} \tag{3.6}$$

Figure 3.12 shows the obtained tauc plot for the samples grown with different O_2 during deposition.

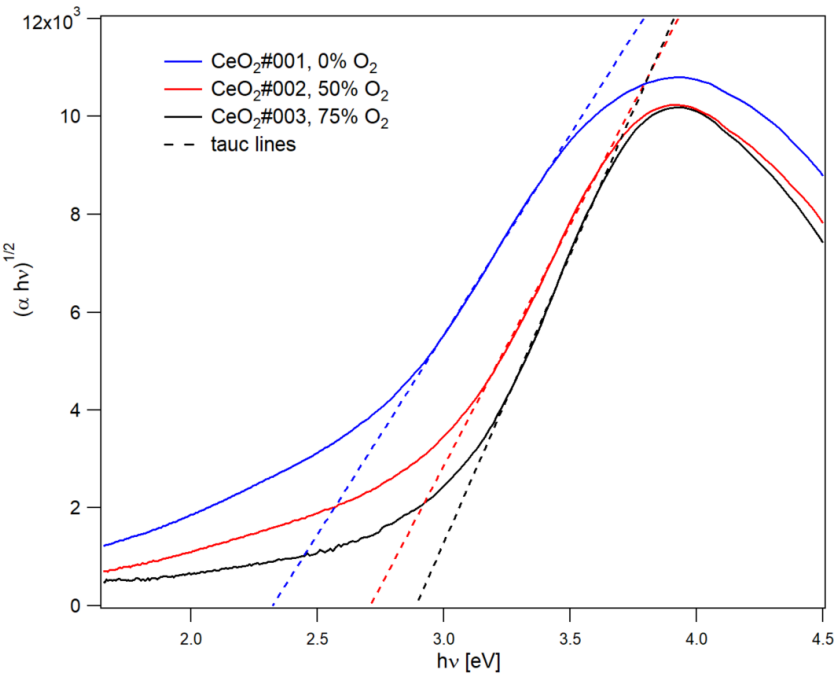

Figure 3.12: *Tauc plot of the MS-grown CeO_2 samples grown in different oxygen flow during deposition*

The obtained E_g are 2.3, 2.7 and 2.9 eV for the samples grown with 0%, 50% and 75% O_2 flow respectively. The band gap of Ce_2O_3 is 2.4 eV [195], while the CeO_2 one can vary between 2.9 to 3.5 eV [196]. This means that, as the O_2 flow during growth increases, the obtained sample has a band gap closer to the one of CeO_2. The XPS Ce 3d fit results showed before that CeO_2#001 has a non-negligible concentration of Ce^{3+}, the tauc plots provided another proof for the presence of a reduced phase of cerium oxide present in the sample.

3.1.3 X-ray Diffraction Measurements

Ceria samples grown by magnetron sputtering have been measured with X-ray Diffraction (XRD) in order to check the crystallinity of the deposited film and if preferential orientation were present.
Samples grown on quartz show no peaks and appear amorphous, even after the sample has been annealed. Figure 3.13 shows XRD measurements of samples CeO_2#004, CeO_2#005 and CeO_2#006 grown on silicon substrates. These samples differ only for the growth temperature, while all of them have been deposited with an O_2 ratio of 75% and a RF power of 150 W. CeO_2#004 has been deposited at RT, CeO_2#005 at 200°C and CeO_2#006 at 300°C.

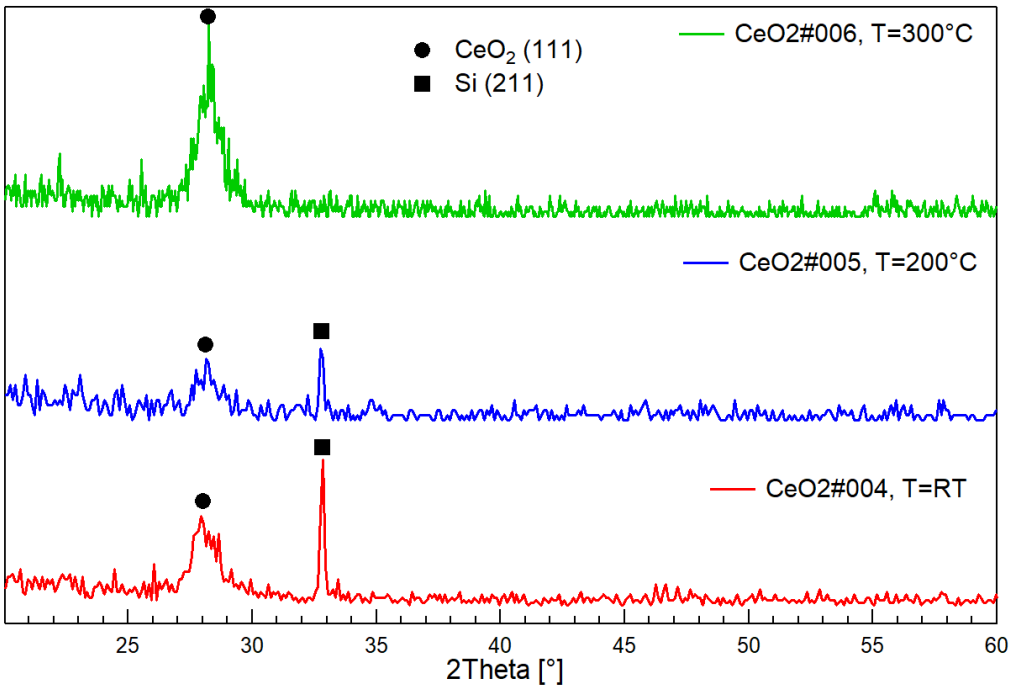

Figure 3.13: *XRD measurements on samples grown on Silicon substrates at different substrates deposition temperatures.*

The peaks position were taken by the POW_COD open diffraction database, in particular the card 00-721-7887. As it can be seen in Figure 3.13, samples CeO_2#004 and CeO_2#005 show the Si (211) diffraction peak at 33°, which is related to the substrate. For what concerns the peaks of the film, only the (111) CeO_2 peak at 28.5° is visible. The ceria peak is more defined and intense for the sample grown at 300°C.
From Figure 3.13 it can be concluded that ceria films grown by magnetron sputtering are polycrystalline, with the most intense peak being the CeO_2 (111).

3.2 Ultrafast dynamics of photoexcitations in cerium oxide films

Following the results obtained by the first experiment involving UV-visible pump-probe spectroscopy on ceria samples and described in Chapter 1 [99], the next step has been to further investigate the polaron formation and lifetime by using a pump and X-ray probe experimental setup. X-ray absorption and emission techniques

can probe the occupation of electronic states in ceria and Extended X-ray Absorption Fine Structure (EXAFS) can give information about the distance between the excited atom and its first neighbour, thus identifying the lattice distortion after photoexcitation.
Pump probe experiments involving X-ray pulses as a probe are performed at X-ray Free electron Lasers (XFELs) which, as explained in the Experimental Setup section, can produce coherent and ultrafast sinchrotron radiation X-ray pulses with high brightness. The experiment that is going to be described in this section has been performed at the FXE beamline at the European XFEL in Hamburg, Germany. FXE employs an ultrafast tunable laser as pump with a wavelength in the UV-visible range. Pump-probe X-ray absorption (XAS) and X-ray emission (XES) spectroscopies are available with a time resolution below 100 femtoseconds, in an energy range for the X-rays between 5 and 20 keV.
Two beamtimes have been performed at XFEL: one in February 2023, and the other one in February 2024.

Sample	CeO_2 thickness
XFEL2023#001	50 nm
XFEL2023#002	200 nm
XFEL2023#003	100 nm
XFEL2023#004	30 nm
XFEL2024#005	50 nm
XFEL2024#006	20 nm

Table 3.2: *CeO_2 deposited thickness for the MS-grown CeO_2 samples deposited on sapphire substrates*

Table 3.2 shows the film thickness of the CeO_2 samples deposited on sapphire substrates for the pump probe experiment. The samples used for the beamtimes are 50 nm and 200 nm ceria films. The 200 nm film has been employed for beam alignment and to check if the samples could withstand the damage caused by the pump and the high-energy X-ray FEL beam. The measurements were instead performed on the 50 nm sample. As explained before, the samples have been grown by reactive MS sputtering and their stoichiometry has been previously checked, so that they were in Ce^{4+} phase. The substrates are circular with a diameter of 25.4 mm and a thickness of 0.5 mm. These dimensions have been chosen in such a way that the surface area of the sample was large enough for the sample to be scanned during measurements, in order to reduce the damage caused by the X-ray laser beam. The measurements have been performed at a grazing angle of 10°, in order to further diminish the beam damage and to maximize the portion of the 50 nm ceria film that is being excited by the UV-visible laser.
The pump laser used to excite the ceria film has a wavelength of 267 nm, which corresponds to a photon energy above the band gap of CeO_2 of 4 eV. The laser carried an energy for every pulse of 5 μJ during the 2023 experiment and 20 μJ during the 2024 experiment. The sample was placed inside a transparent chamber in He gas flow.
The X-ray probe energy was scanned across the Ce L_3 absorption edge at 5.73 KeV, the energy was selected by using a double crystal monochromator. The X-ray beam intensity was attenuated to less than 1% of the one incoming from the SASE. By using this intensity no sample damage has been detected through the whole experiment, furthermore the sample surface was imaged after the experiment by using

an optical microscope and no beam trace was detected. The X-ray beam carried 20 pulses per train in the first experiment and 40 pulses per train in the second experiment, furthermore one every two train was pumped with the UV laser.

3.2.1 Pump-probe RXES

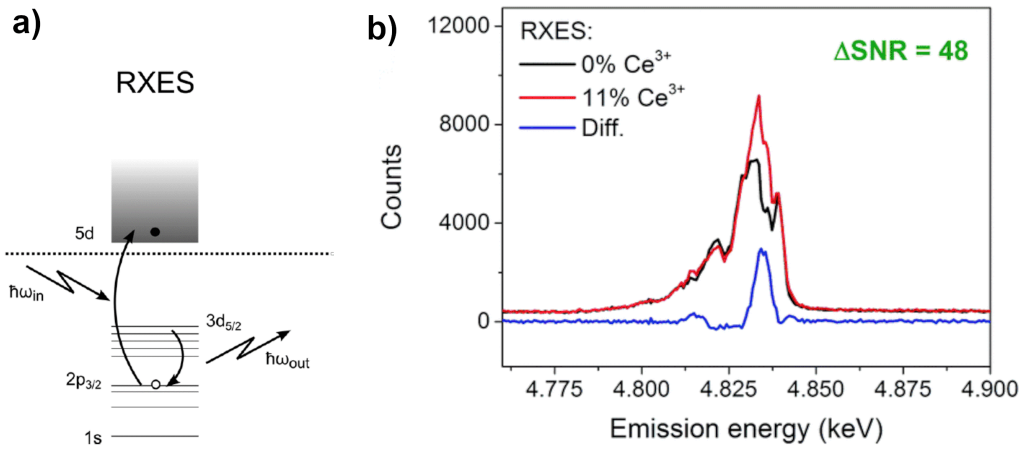

Figure 3.14: *a) Scheme of the L_α RXES process in the cerium atom and b) RXES spectra of a 100% Ce^{4+} sample and a ceria sample with a Ce^{3+} concentration of 11%, the difference between the spectra is also shown[197].*

X-ray Emission Spectroscopy (XES) is a technique in which an X-ray beam with a fixed energy illuminates the sample and the intensity of the emitted X-rays is plotted as a function of their energy. XES can take two different forms: it can be resonant (RXES) or non resonant (NXES). In the first case a core electron is excited by an X-ray beam into a bound state in the conduction band, while instead in the second case the electron is promoted to the continuum. In both cases the fluorescence that occurs when the atom relaxes is measured as a function of the emitted X-ray energy.

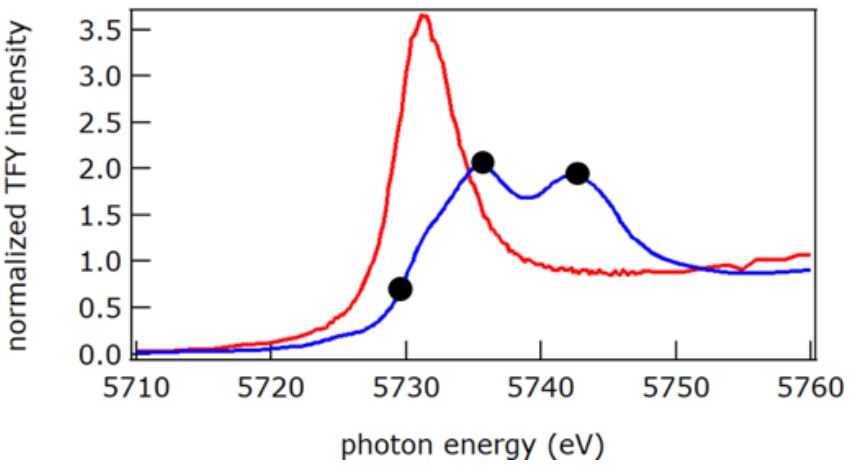

Figure 3.15: *Ce^{4+} (blue line) and Ce^{3+} (red line) Ce L_3 edge XANES spectra showing the X-ray beam energies that have been chosen to excite the ceria sample in the RXES measurements.*

A scheme of the Ce L_α RXES process is shown in Figure 3.14 a), while Figure 3.14 b) shows the reason why RXES has been used to study the excitation of ceria samples: this technique is very sensitive to even low differences in the concentration of Ce^{3+} in different samples [197], therefore it is expected to be sensitive also to differences in the electronic configuration of photoexcited Ce ions.
In the experiment, pump-probe RXES measurements have been performed at three different incoming X-ray photon energies: 5729, 5735 and 5742 eV. Figure 3.15 shows these energies on the Ce L_3 edge XANES spectra of Ce^{4+} near the Ce L_3 edge at the onset of absorption, on the first and the second absorption peaks respectively. Then, with the X-ray beam fixed at each one of these energies, the pump-probe time delay has been set to 300 fs, 1 ps and 10 ps. For each measurement, the difference between the spectrum acquired with the laser pump on and off has been computed. The difference RXES spectra for the measurements performed at different energies and time delays are shown in Figure 3.16.

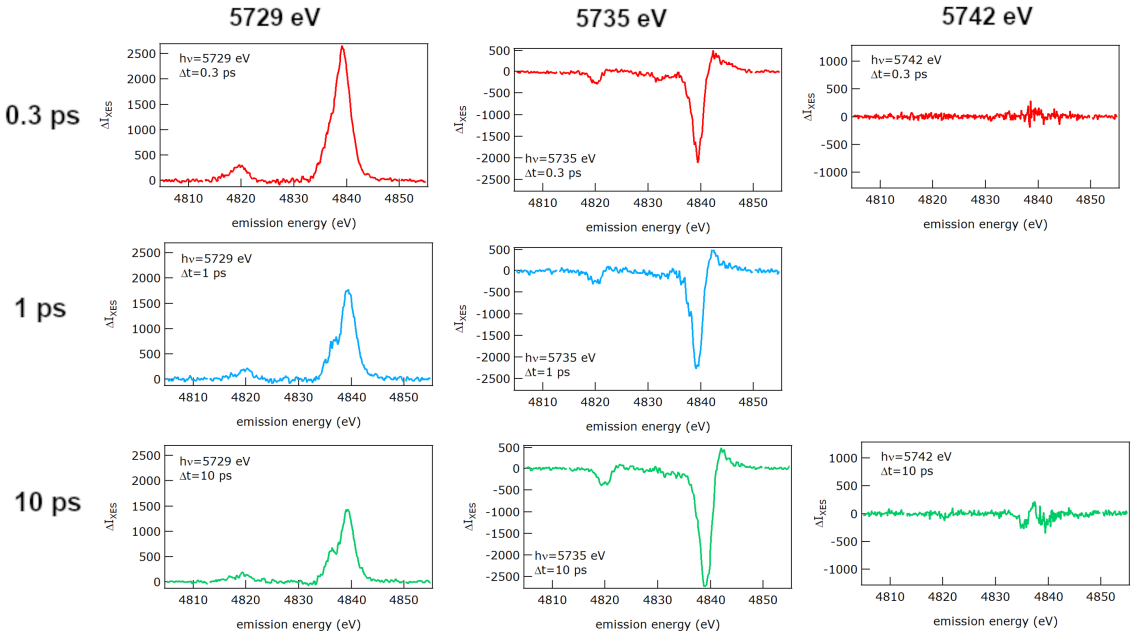

Figure 3.16: *RXES pump-probe difference spectra at different photon energies and at different delay times.*

By comparing the difference spectra in Figure 3.16 acquired with an incident X-ray beam energy of 5729 and 5735 eV and a time delay of 0.3 and 1 ps with the difference between the Ce^{3+} and Ce^{3+} RXES reference spectra in Figure 3.14, it can be seen that the shape of the measured difference spectra is the same in both cases. This hints that the excitation taking place in the ceria sample is related to an excited state that is Ce^{3+}-like. This state is present in the first picoseconds after the excitation and then decays, as it can be seen from the measurements acquired at 5729 eV, where the intensity of the signal decreases as the time delay between the pump and the probe increases.
Furthermore, the intensity of the RXES difference spectra at 5742 is almost zero, due to the fact that that this photon energy is 13 eV above the Ce L_3 absorption edge, and, being out of resonance, it is relevantly less sensitive to modifications of the electronic structure than the other two photon energies used to excite the film.

3.2.2 Pump-probe XANES

X-ray Absorption Near Edge Structure (XANES) is an X-ray spectroscopy, in which the X-ray absorption by the sample as a function of the incoming X-ray beam energy is measured in proximity of the absorption edge. During the experiment, the absorption has been measured by using a photodiode placed in front of the sample. The photodiode measures the total fluorescence yield, that is proportional to the absorption by the sample.
The ceria absorption edge is situated at about 5730 eV and so the spectra were acquired between 5710 and 5750 eV.
XANES spectra have been acquired at the following time delays between the pump and the probe of 100 fs, 230 fs, 500 fs, 1 ps and 10 ps.

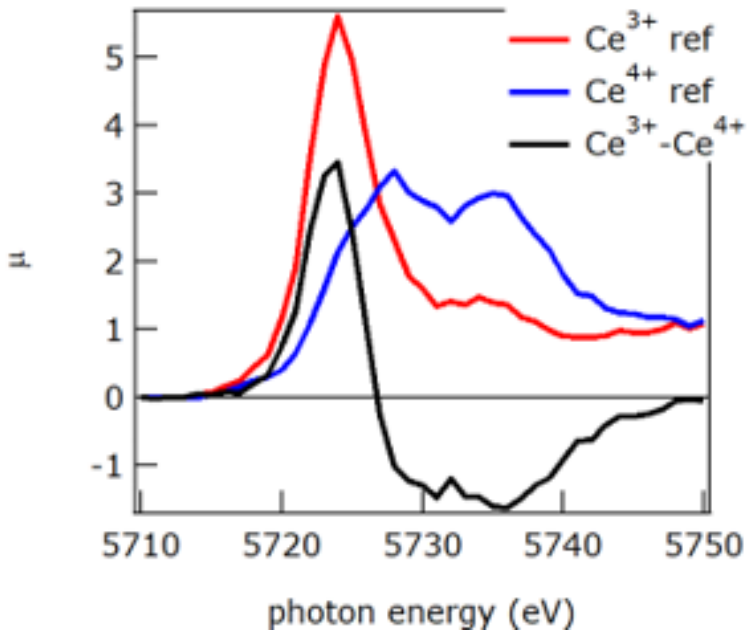

Figure 3.17: *Ce L_3 XANES spectra measured on Ce^{3+} and Ce^{4+} references, the difference between the two spectra is also shown).*

Figure 3.17 shows the XANES spectra of a Ce^{3+} and a Ce^{4+} references, together with their computed difference. The reference samples consist of cellulose pellets containing a small amount of reference compounds in the form of powder. The amount of powder to put in each pellet has been calculated in order to obtain an absorption below $\mu T = 0.1$. The absorption has to be kept low in order to ensure that only the FEL X-ray would excite the sample atoms and avoid that the photons emitted by the pellet atoms by fluorescence de-excitation would in turn excite other atoms in the pellet. By keeping the powder density in the pellet low, the probability for an X-ray photon emitted by fluorescence to being absorbed by another atom before it exits the pellet can be considered negligible. In this way, the X-ray absorption process by the pellet is a single step process. The Ce^{4+} reference pellet was made by using 150 μg of CeO_2 powder and 40 mg of cellulose, while for the Ce^{3+} reference pellet 340 μg of $Ce(NO_3)_3 \times 6H_2O$ powder has been combined with 40 mg of cellulose. Both pellets had a diameter of 7 mm and they were prepared at the chemistry lab of EuXFEL. The atomic background on both spectra has been substracted and they have been normalized to the edge step and their difference has been computed.

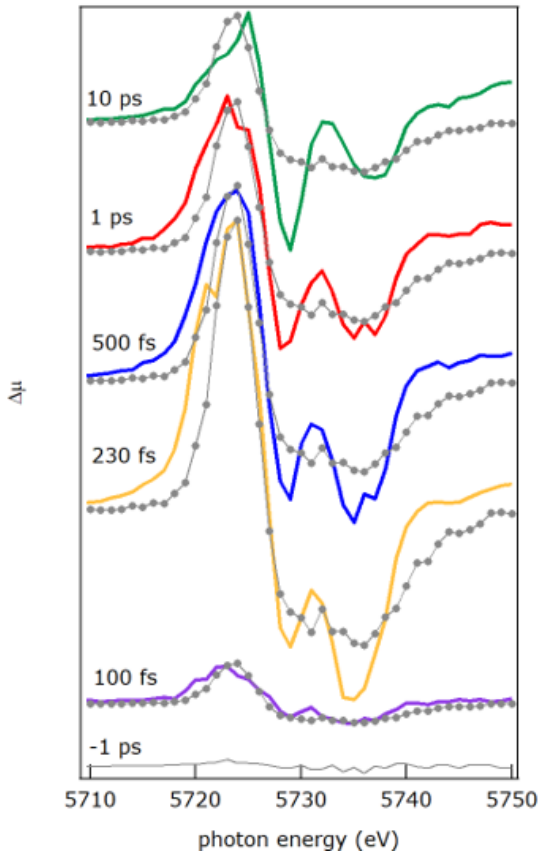

Figure 3.18: *XANES difference spectra obtained for each pump probe-probe time delay (colored solid lines), each spectrum is fitted with the Ce^{3+}-Ce^{4+} reference difference spectrum from Figure 3.17.*

Figure 3.18 shows the Ce L_3 XANES difference spectra recorded at different time delays as a function of X-ray beam photon energy, represented as colored solid lines. The grey dots instead represent the Ce L_3 XANES Ce^{3+}-Ce^{4+} difference spectrum in Figure 3.17, in which the positive peak intensity has been normalized to the one of the measured Ce L_3 XANES difference spectra. The acquired spectra are pump-probe XANES and they represent the difference between a spectrum acquired after the photoexcited at the shown time delay and the spectrum acquired without the pump excitation. This kind of measurements is useful to identify the characteristics of the pump excitation and its time evolution. As it can be seen from Figure 3.18, the pump-probe Ce L_3 XANES spectra for a time delay of 500 fs and below are fitted well by the Ce^{3+}-Ce^{4+} reference difference spectrum, while the discrepancy between the acquired XANES spectra and the Ce^{3+}-Ce^{4+} reference difference spectrum increases at longer time delays. This means that the excited state of CeO_2 caused by the pump laser is similar to the Ce^{3+} Ce L_3 XANES spectrum in Figure 3.17, while its ground state is the Ce^{4+} Ce L_3 XANES spectrum in Figure 3.17 and their difference Ce^{3+}-Ce^{4+} reproduces well the pump-probe XANES spectra measured on the CeO_2 sample. The excited state in CeO_2 caused by the pump is a Ce^{3+}-like excitation that lasts for $\sim$ 500 fs and then relaxes: this is proven by the fact that the discrepancy between the Ce^{3+}-Ce^{4+} reference difference spectrum and the measured pump-probe XANES spectrum increases for $\Delta t > 500$ fs.

3.2.3 Pump-probe EXAFS

Extended X-ray Absorption Fine Structure (EXAFS) is an X-ray absorption Spectroscopy technique in which the sample X-ray absorption is measured as a function of the impinging X-ray energy in a range that extends several hundreds of eV after the absorption edge. EXAFS spectra can give valuable information about the atoms surrounding the excited atoms and thus can identify if the excitation has caused a lattice distortion in the sample.

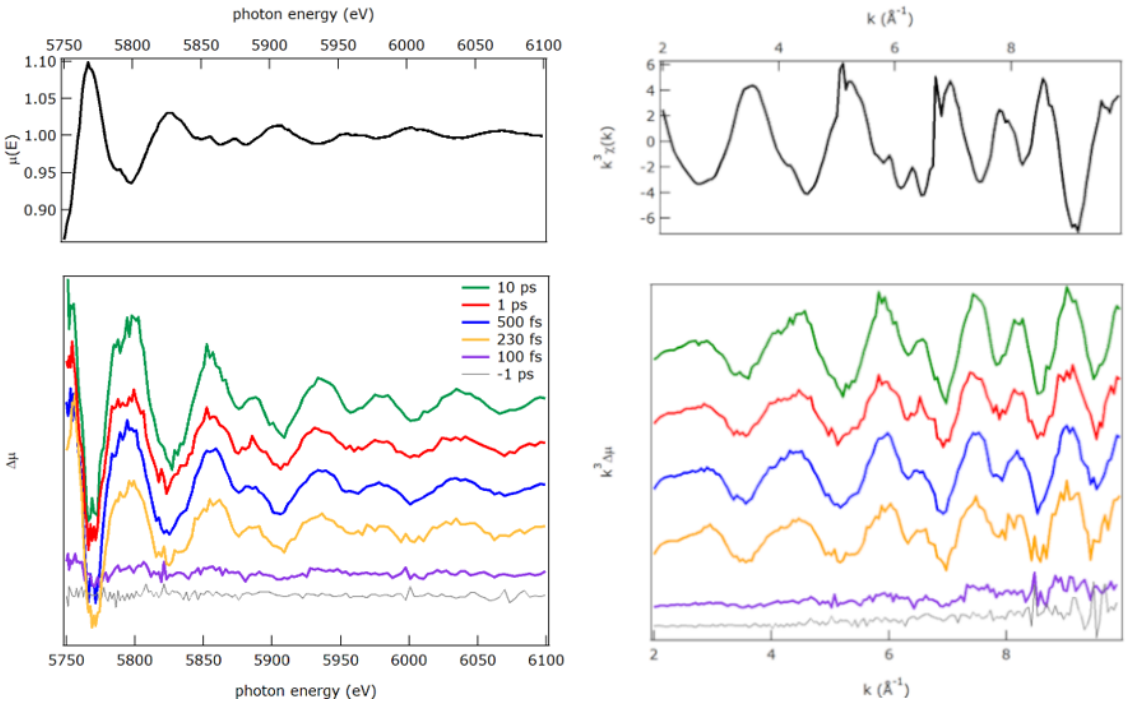

Figure 3.19: *Ce L_3 EXAFS spectra measured on the ceria samples. The left panel shows the EXAFS signal as a function of the photon energy, while the right panel shows the EXAFS signal weighted by k^3 as a function of the wavevector k. In both panels, on the top the graph of the ground state EXAFS absorption spectrum is shown, while on the bottom the graphs for the Ce L_3 EXAFS pump-probe difference spectra at different time delays are represented.*

The left panel of Figure 3.19 shows on the bottom the pump-probe EXAFS difference spectra acquired on the ceria sample at the different time delays, while on the top the EXAFS spectrum of unexcited Ce^{4+}. The right panel of Figure 3.19 shows the EXAFS signal $\chi(k)$ as a function of the wavevector k of the photoelectron obtained from:

$$k = \sqrt{\frac{2m_e}{\hbar^2}(E - E_0)}$$

where m_e is the electron mass, $\hbar$ is the reduced Planck constant and E_0 is the absorption edge energy. The EXAFS signal shown in the right panel is weighted by k^3 in order to better resolve the oscillations in the spectrum for high values of k. As in the right panel, the graph on top represents the unexcited EXAFS spectrum, while the one on the bottom shows the pump-probe difference spectrum at different time delays. The difference pump-probe EXAFS spectra in Figure 3.19 show almost no differences after a time delay of 230 fs both for the spectra measured as a function of the photon energy or k.

EXAFS data analysis

A quantitative analysis of the EXAFS data has been perfomed using the Demeter software package [198]. In order to perform the fit to find the structural distortion of the lattice caused by the excitation, a first shell analysis of $\Delta\mu$ as described in the article of Gawelda W. et al. has been used [199]. The fitting parameters used are:

- α, which represents the fraction of sample that has been excited by the pump laser
- dr and dr_{exc}, are the atom's positions displacement in absence and presence of the pump laser respectively
- $S0^2$, E_0 and σ, which are respectively the amplitude reduction factor, the absorption edge energy and the Debye-Waller factor.

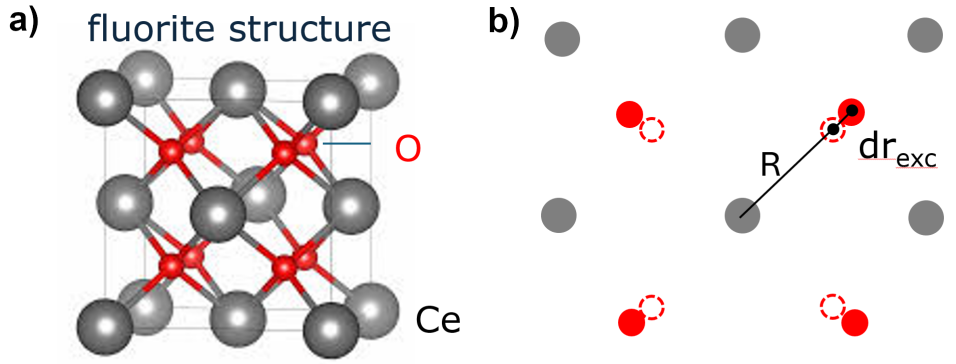

Figure 3.20: *a) Ceria fluorite structure and b) Ceria lattice distortion caused by the laser pump excitation.*

The difference absorption can be written as:

$$\Delta\mu = \mu_{on} - \mu_{off}$$
$$\mu_{on} = \alpha\mu_{exc} + (1-\alpha)\mu_{off} = \alpha\mu_{exc} + \mu_{off} - \alpha\mu_{off}$$
$$\Delta\mu = \mu_{on} - \mu_{off} = \alpha(\mu_{exc} - \mu_{off})$$

where μ_{on} is the sample X-ray absorption coefficient with the pump laser switched on, μ_{off} is the sample X-ray absorption with the pump laser switched off and μ_{exc} is the X-ray absorption in the fraction of the sample that has been excited by the pump laser.
In the μ_{off} state, the model system that has been been used is composed by 8 O atoms scatterers placed in cubic coordination at a distance R from the Ce absorber atom, with fitting parameters S_0^2, dr, E_0 and σ^2.
Instead, in the μ_{exc} state, the model system is composed by 8 O atoms scatterers at a distance $R + dr_{exc}$ and 4 O atoms scatterers at a distance $R - dr_{exc}$ from the considered Ce atom. The fitting parameters are α and dr_{exc}, while S_0^2, E_0 and σ^2 are fixed to their values obtained in the ground state. Figure 3.20 a) shows the fluorite structure of ceria, while Figure 3.20 b) depicts the distortion suffered by the O scatterers caused by the pump laser excitation.
Figure 3.21 shows the Fast Fourier Transform of the EXAFS signal, $|\chi(R)|$ as a function of the distance R[Å] from the excited Ce atom and their relative fits for

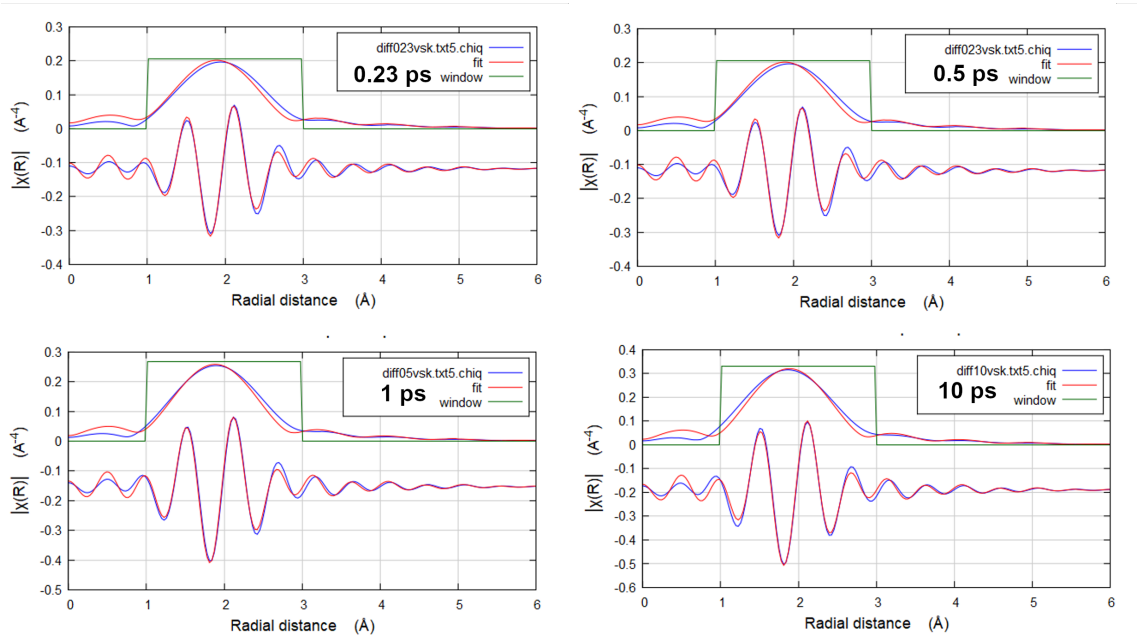

Figure 3.21: $|\chi(R)|$ *calculated from EXAFS for different pump-probe time delays together with their fit*

each pump-probe time delay.
The important coefficients are the percentage of excited sample α and the distortion caused by the excitation dr_{exc}, these results are shown in Table 3.3.

Δt	α [%]	dr_{exc} [Å]
0.23 ps	2.6 ± 0.4	0.21 ± 0.02
0.5 ps	2.7 ± 0.4	0.24 ± 0.03
1 ps	2.3 ± 0.4	0.24 ± 0.02
10 ps	3.8 ± 0.7	0.23 ± 0.02

Table 3.3: *Results for the α and dr_{exc} coefficients obtained from the EXAFS fit*

The fit coefficients listed in Table 3.3 do not vary for different delay times within the error range considered, furthermore the value of the structural distortion dr_{exc} is compatible with a photoinduced small polaron formation.

XANES and EXAFS dynamics

To study in detail the dynamic modifications of the electronic properties and of the structure, the X-ray absorption difference signals in various regions of the spectra have been measured as a function of the pump-probe delay times. Figure 3.22 shows the X-ray energies that have been selected for the time dynamics spectra. These energies are 5723 eV, which is located on the onset of the absorption edge, 5794 eV, located in the XANES region in correspondence of an oscillation maximum and 5825 eV, located in correspondence of an oscillation minimum.

The resulting kinetic traces have been fitted with a sum of exponential functions with their characteristic time τ. In the case of XANES, three τ have been used: τ_1 for the absorption edge, which corresponds to the Instruments Response Function (IRF) and the other two for the decay after the absorption: τ_2 for the first part of

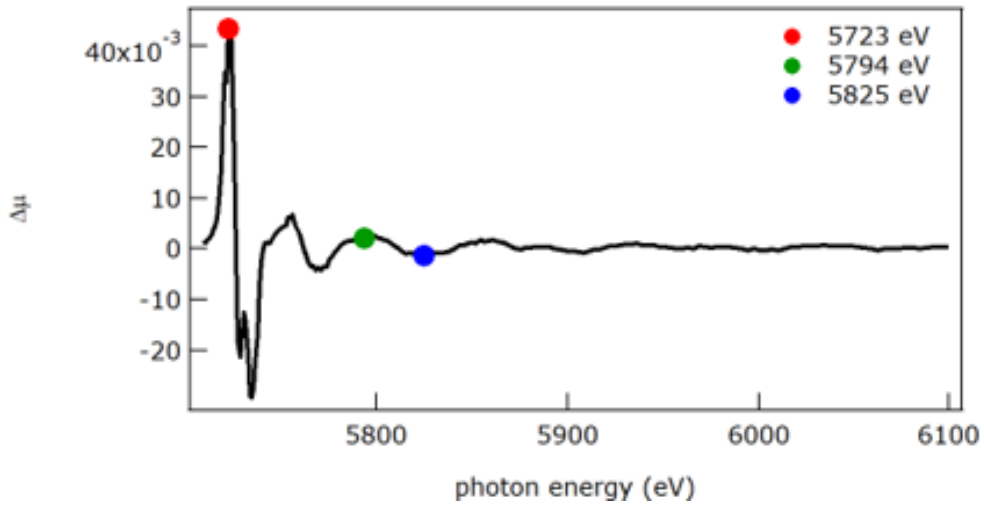

Figure 3.22: *EXAFS pump-probe spectrum showing the X-ray beam energies selected for the time dynamics measurements.*

the decay and τ_3 for the decay at longer times. The fit function has an expression:

$$A_1 e^{\frac{x-c}{\tau_1}} + A_2 e^{\frac{x-c}{\tau_2}} + A_3 e^{\frac{x-c}{\tau_3}}$$

Instead, in the case of EXAFS energies, they have been fitted with the expression

$$A_1 \left[1 + erf\left(\frac{(c+x)0.045}{\sqrt{2}}\right)\right] - \left\{A_1 e^{-\frac{(c+x)}{\tau_1}} e^{\frac{0.045^2\tau_1^2}{2}} \left[1 + erf\left(\frac{(c+x)0.045}{\sqrt{2}} - \frac{0.045\tau_1}{\sqrt{2}}\right)\right]\right\} + \text{offset}$$

where x is the delay time measured in ps, τ_1 is the exponential decay time, erf is the error function and c and A_1 are fit parameters.

Figure 3.23 a) shows the two curves corresponding to the kinetic traces acquired at 5723 eV for XANES and 5825 eV for EXAFS, with the τ obtained from the fits. From the coefficients shown in Figure 3.23 a), the most important ones are τ_2 for the XANES and τ_1 for the EXAFS, since those coefficients represent the lifetime of the Ce^{3+}-like excited state. For both these coefficients, a value of $\sim 500fs$ is obtained, meaning a characteristic time compatible with the change of the local atomic structure and a polaron formation.
Furthermore, as shown in Figure 3.23 b) where XANES and EXAFS spectra are graphed until the maximum time delay measured, the excitation-induced distortion persists up to 300 ps after the excitation.

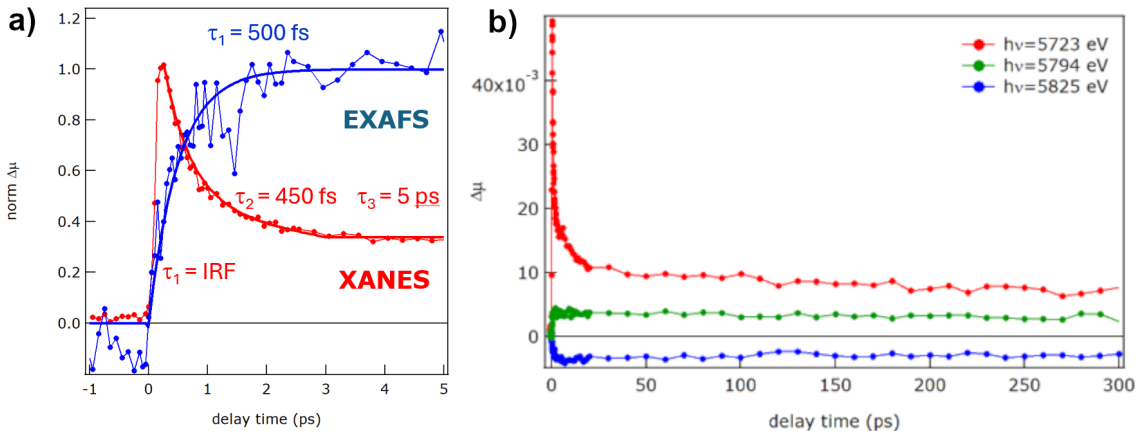

Figure 3.23: *a) Kinetic traces of the pump-probe difference absorption signals at 5723 eV (XANES region) and 5825 eV (EXAFS region) showing the τ coefficients obtained from the exponential fits and b) Kinetic traces of the pump-probe difference absorption signals at 5723, 5794 and 5825 eV as a function of the pump-probe delay time until 300 ps after the excitation.*

3.3 Study of Cu-doped cerium oxide films in water and under light exposure

In order to study the photocatalytic properties of CeO_2 doped with Cu, an experiment at the APE-HE beamline at the Elettra synchrotron in Trieste has been performed. In the experiment, the samples were placed inside a catalytic cell in a water environment while illuminated by a laser. XANES spectroscopy of the Ce $M_{4,5}$ absorption edge has been used to determine the modification suffered by the samples. In particular, a subsequent fit on XANES Ce $M_{4,5}$ spectra returned the concentration of Ce^{3+} ions inside the sample. In parallel, micro gas chromatography (MGC) have been acquired in order to detect the formation of gases produced by the photocatalytic reactions. The samples for the beamtime at the APE-HE beamline at Elettra have been grown on transparent MgO 10 mm square substrates.
The substrates were firstly cleaned by putting them in acetone bath for 5 minutes at 150°C on a hot plate, in a bath in an ultrasonic cleaner washer in acetone and then in isopropyl alcohol at 80°C for 3 minutes. The substrates were then cleaved, in order to obtain two samples for each deposition.
The samples were grown by MBE at the Ragno-1 apparatus at SESAMo laboratories in Modena. The samples consisted in CeO_2 thin layers (about 3 nm thick) doped with different concentrations of Cu. A CeO_2 undoped sample was also prepared. Table 3.4 contains a list of the deposited samples together with their composition and thickness. The doped samples are indicated with the names Cu:CeO_2 followed by the Cu atomic concentration in the samples.

Name	composition	layer thickness
APE#001	CeO_2 undoped	CeO_2: 3 nm
APE#002	Cu:CeO_2 5%	CeO_2: 3.6 nm
APE#003	Cu:CeO_2 11%	CeO_2: 3.3 nm

Table 3.4: *CeO_2 samples grown for the APE experiment, together with their composition and layer thickness*

The deposition procedure starts with the cleaning of the substrate in the UHV

chamber with a 15 minutes annealing at P=1 $\times$ 10^{-10} mbar and T=500°C, the substrate then undergoes sputtering with Ar gas for 30 minutes with an Ar pressure in the chamber of $P_{Ar} = 1 \times 10^{-6}$ mbar. This procedure ensures that the MBE grown films correctly adhere to the substrate. The CeO_2 doped and undoped samples were also annealed after the CeO_2 deposition for 45 minutes at 450°C in an oxygen pressure of $P_{O_2} = 1 \times 10^{-7}$ mbar to optimize the oxide stoichiometry.
Absorption spectroscopy measurements in the UV-Vis-IR have been performed on the deposited samples, in order to check the absorptance of the films and choose the wavelength of the laser to be used during the experiment at Elettra accordingly. The measurements have been performed with an incidence angle of 22° in S polarization. Figure 3.24 shows the UV-Vis-IR absorption spectra of the deposited samples. The wavelength of the laser chosen to be used during the experiment is 375 nm.

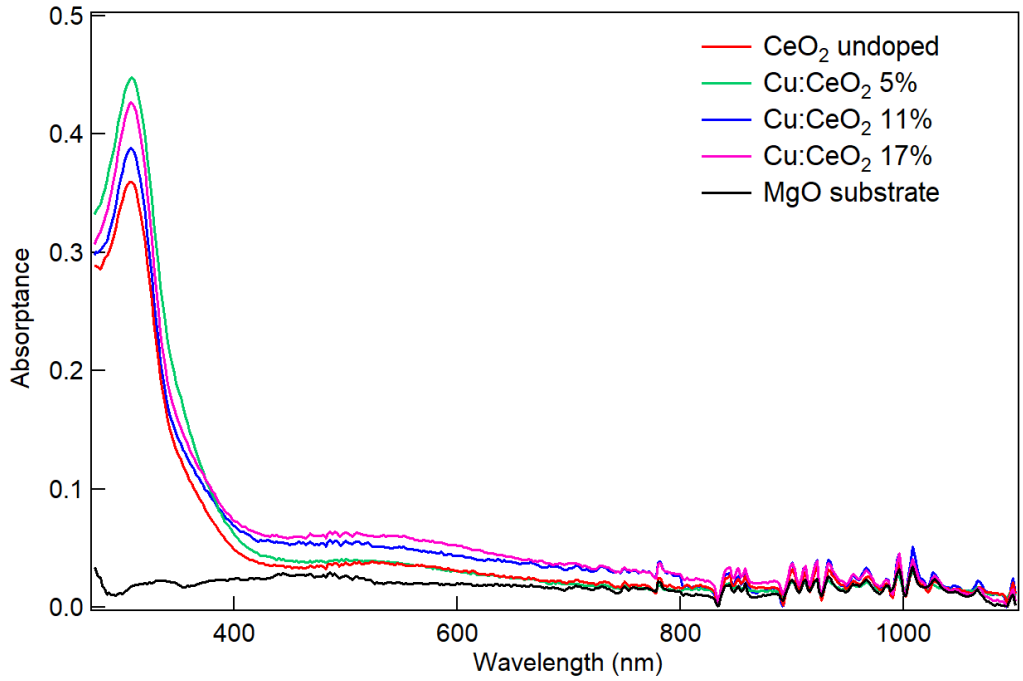

Figure 3.24: *Optical absorption spectra of the samples deposited for the beamtime.*

The experiment at the synchrotron consisted in XANES measurements at the Ce $M_{4,5}$ absorption edge of the samples when illuminated by a laser and exposed to water flux at different temperatures in order to study the modification of the samples during photocatalytic water splitting. In parallel with the XANES measurements, MGC data have been collected in order to identify H_2 production in the reaction cell as a function of temperature. Before starting the measurements in water flux, the films have been oxidized by filling the reaction chamber with a flux of 28 sccm O_2 and 2 sccm He.
During the measurements in water environment, the samples were exposed to 1 bar water flux which was provided by a bubbler in He carrier. The temperature of the sample was increased from 100°C to 300°C and the XANES measurements have been performed at temperature steps of 50°C both with the laser switched on and off. The laser has a wavelength of 375 nm, this value has been chosen in order to match the absorption peak of ceria in the optical spectra in Figure 3.24.
The XANES spectra have been fitted in order to obtain the concentration of reduced and oxidized phases for both Ce and Cu.

Ce $M_{4,5}$ has been fitted by using the function:

$$f(En) = A + B \cdot CeO_2^{ref} \cdot (En - E_0) + C \cdot Ce_2O_3^{ref} \cdot (En - E_0) + D \cdot En \quad (3.7)$$

where En is the photon energy of the incoming X-ray beam, CeO_2^{ref} and $Ce_2O_3^{ref}$ are respectively the CeO_2 and Ce_2O_3 XANES spectra measured from a reference powder sample and A, B, C, D and E_0 are the fit parameters.

From the fit of every XANES spectrum the concentration of Ce^{3+} ions $\frac{Ce^{3+}}{Ce^{3+} + Ce^{4+}}$ is calculated from:

$$\frac{Ce^{3+}}{Ce^{3+} + Ce^{4+}} = \frac{C}{C + B}$$

where B and C are the fitting parameters of equation 3.7.

Figure 3.25 shows an example for the fit of Ce $M_{4,5}$ XANES edge data, together with the references used.

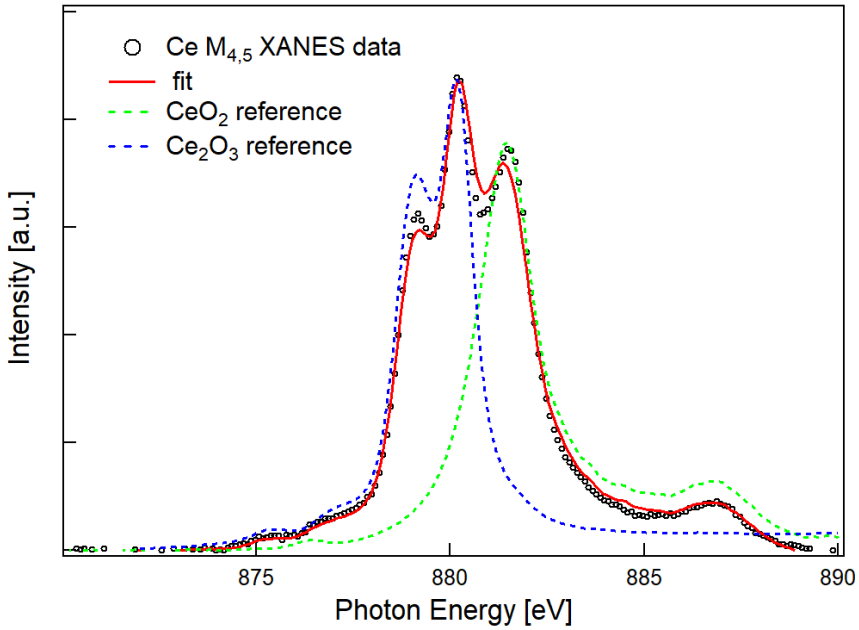

Figure 3.25: *Examples of fit for the Ce $M_{4,5}$. The references used for the fits are also shown.*

Figure 3.26 shows the XANES Ce $M_{4,5}$ edge spectra for the CeO_2 undoped sample acquired at different temperatures with and without illumination from the laser. The areas of the XANES Ce $M_{4,5}$ edge spectra from 872 to 892 eV in Figure 3.26, as well as the ones for the other samples, have been normalized to 1. The XANES spectra are compatible with the ones for Ce^{4+} and here the Cerium appears to be oxidized. The XANES spectra show little modifications as a function of the rising temperature. As it can be seen from Figure 3.27, the laser has no effect on the Ce^{3+} concentration for the sample. The sample undergoes a mild oxidation when water is added into the chamber at 150°C and mild reduction at 200°C, which are both not linked to photocatalysis reactions, due to the fact that the "laser on" and "laser off" trends show no differences.

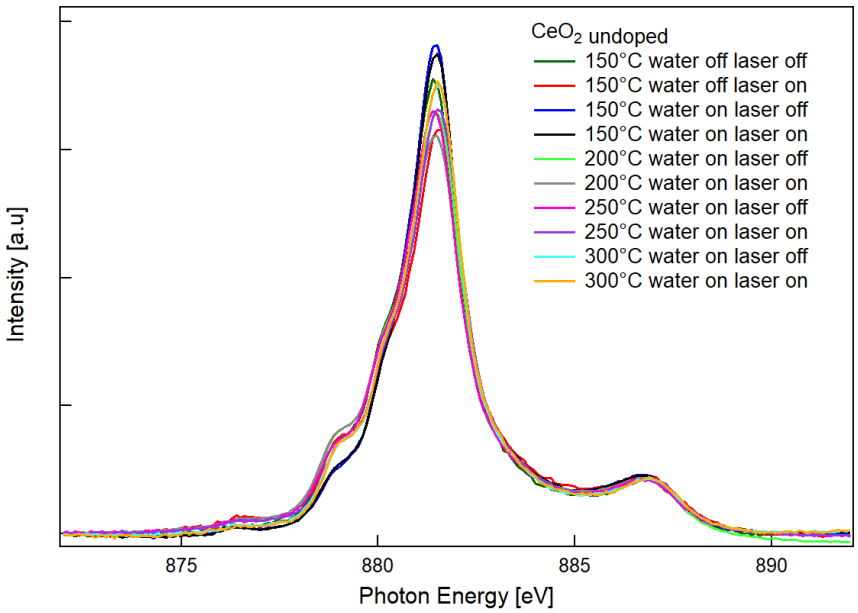

Figure 3.26: *Ce $M_{4,5}$ XANES edge spectra for the CeO_2 undoped sample at different temperatures with and without laser illumination.*

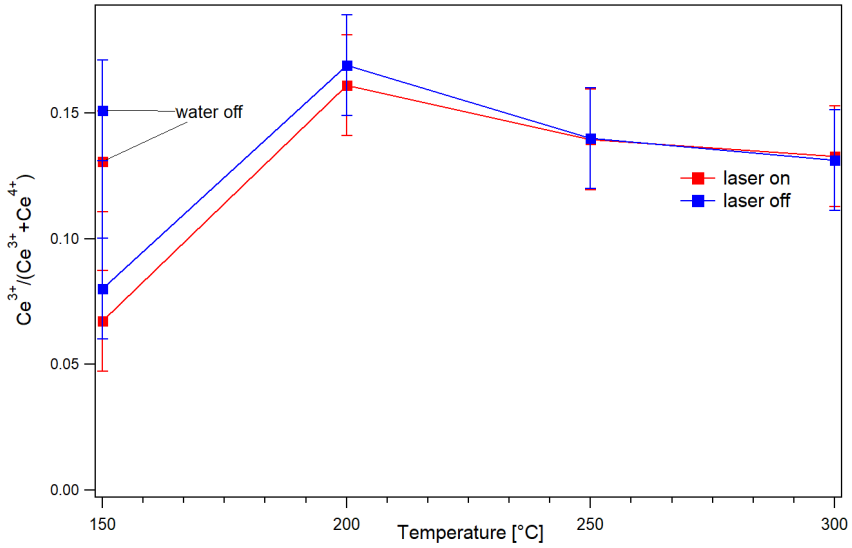

Figure 3.27: *Trends of Ce^{3+} ions concentration obtained from the fits of the spectra for the undoped sample shown in Figure 3.26 as a function of temperature.*

A possible explanation for the reduction is that oxygen vacancies are formed with increasing temperature. After 200°C, the Ce^{3+} concentration does not vary significantly.
Figure 3.28 shows the XANES Ce $M_{4,5}$ edge spectra for the CeO_2 Cu-doped 5% sample acquired at different temperatures with and without illumination from the laser. The spectra are also in this case compatible with the Ce^{4+} ones, they show a mild reduction when the laser is switched on at 100°C and then a mild oxidation at 250°C. This is clearly visible in the two bottom trends in Figure 3.29, which correspond to the Cu-doped 5% sample. There is little to no variation in the Ce^{3+} concentration as a function of temperature, and the spectra acquired with the laser switched on and off follow the same trend, meaning that the laser has no effect on the reduction or oxidation of Ce atoms.

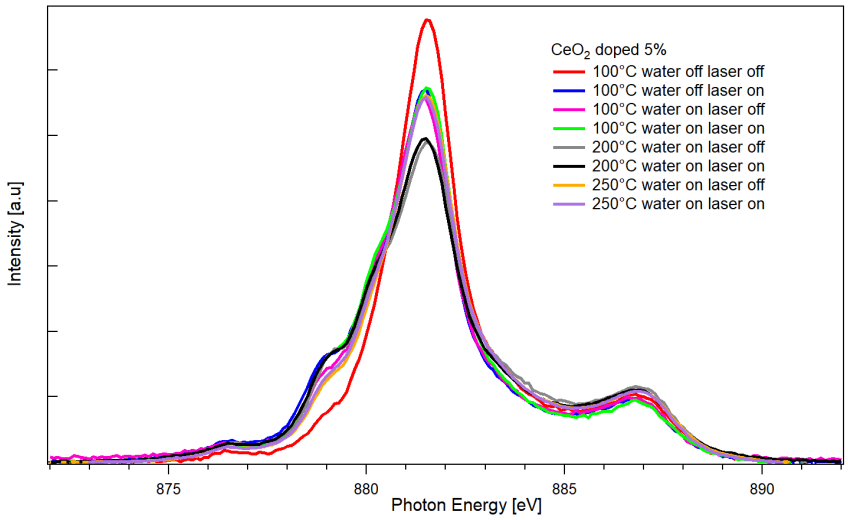

Figure 3.28: *Ce $M_{4,5}$ XANES edge spectra for the CeO_2 Cu-doped 5% sample at different temperatures with and without laser illumination.*

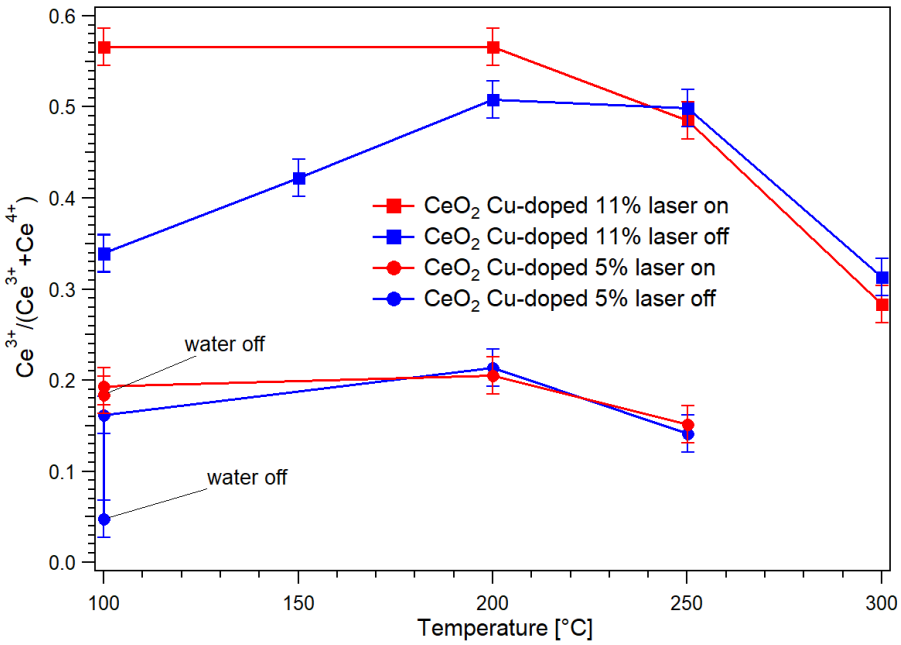

Figure 3.29: *Trends of Ce^{3+} ions concentration obtained from the fits of the spectra for ceria Cu-doped samples shown in Figure 3.28 and 3.30 as a function of temperature.*

Figure 3.30 shows the XANES Ce $M_{4,5}$ edge spectra for the CeO_2 Cu-doped 11% sample acquired at different temperatures with and without illumination from the laser. The XANES spectra are compatible with the Ce^{4+} ones until water is fluxed in the cell. Then, a peak at 880 eV and one at 879 eV start to appear. As it can be seen from the reference spectra of Ce_2O3 in Figure 3.25, these peaks are related to Ce^{3+}. The intensity of these peaks than increase until 250°C and then it decreases back at 300°C.

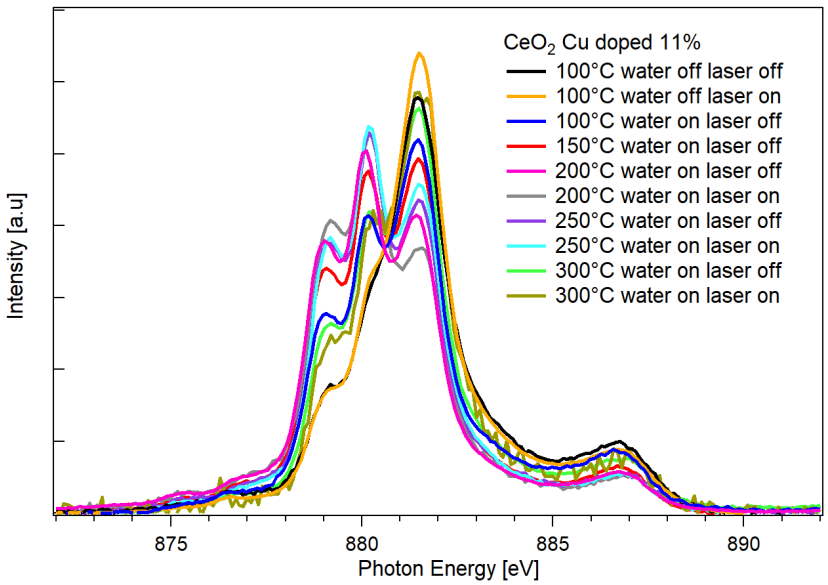

Figure 3.30: *Ce $M_{4,5}$ XANES edge spectra for the CeO_2 Cu-doped 11% sample at different temperatures with and without laser illumination.*

As shown in the two top trends in Figure 3.29, in this case the sample follow two different trends for the laser switched on and off for temperatures lower than 250°C. At 250°C the Ce^{3+} concentration show no variation with respect to the value at 200°C without the laser. However, for the spectra acquired under illumination, the Ce^{3+} concentration decreases when reaching 250°C.

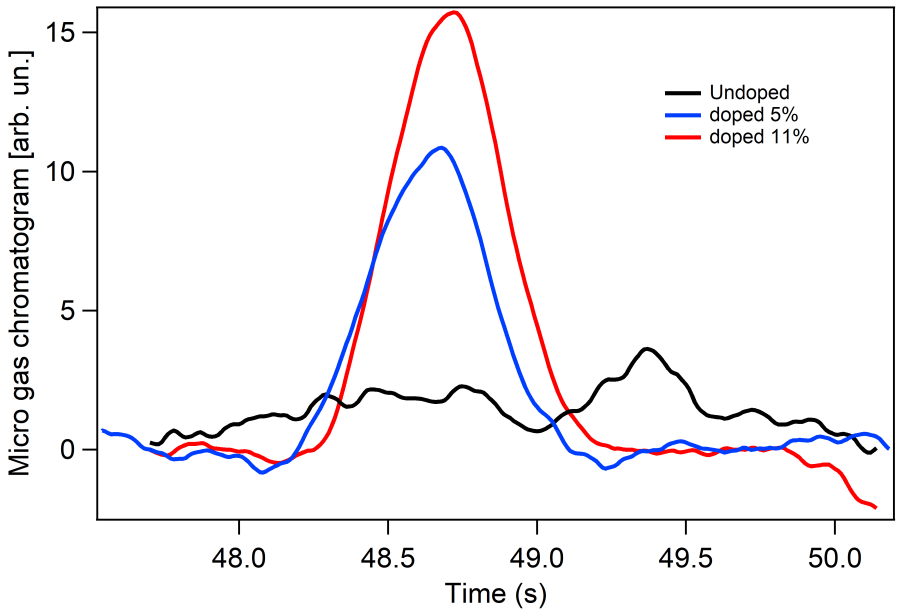

Figure 3.31: *H_2 GMC signal for the three different samples as a function of acquisition time.*

At 300° C the Ce^{3+} concentration keeps decreasing significantly and it reaches the value measured at 100° C without illumination. This can be explained by analyzing the MGC data shown in Figure 3.31. For the undoped sample, there's no production of H_2 meaning that, as stated before, the reduction of Ce atoms is only due to the formation of oxygen vacancies activated by the temperature increase and the

presence of water. The 5% doped sample shows no H2 production up to 300°C, while a slight reduction occurs when switching on the laser. The light then favors the O vacancies formation, as reported in literature. At 300°C H_2 production appears,which however happens for both the measurements with laser on and off. The mild oxidation at 250°C for the 5% sample can thus be explained by the filling of oxygen vacancies by the dissociated water, which however is not produced by photocatalytic reactions. In the 11% Cu-doped sample, H_2 production starts at 250°C and in the case of laser switched on, more H_2 is produced, this means that the laser light starts to cause H_2O dissociation. The increase of Ce reduction below 250°C is due to the formation of O vacancies due to water, temperature and favored by light illumination. When the temperature is sufficient to favor water dissociation on the ceria surface, a drop occur in Ce^{3+} concentration at 250°C, charges left on the reduced ceria act in the H^+ reduction and H_2 formation and compensate the O vacancies with OH leaving the surface more oxidized.

3.4 A procedure to obtain niobium oxide films with variable stoichiometry

As stated in the Chapter 1, it is difficult to obtain the different oxidation states of niobium oxide. This section presents a procedure, consisting of post-growth annealings and oxidations, capable of obtaining the Nb_2O_5, NbO and NbO_2 sample starting from Nb_2O_5 samples deposited by magnetron sputtering.

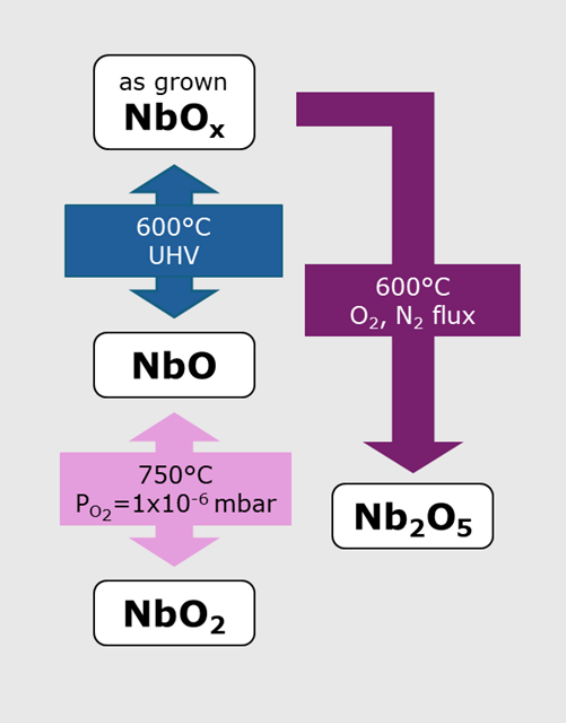

Figure 3.32: *Flow chart describing the procedures to obtain the three niobium oxide stoichiometries*

The substrates used for the growth of niobium oxide films are (100) Si wafers with a 600 nm surface thermal oxide film for X-ray photoemission spectroscopy (XPS) and X-ray diffraction (XRD) measurements. UV-grade fused silica substrates are

instead used for UV-Vis spectrophotometry measurements that require transparent supports. Both kind of substrates were cleaned with a bath in acetone at 150°C for 5 min, followed by an ultrasonic bath in acetone and an ultrasonic bath in isopropanol at 80°C for 3 min. The niobium oxide films were grown by reactive magnetron sputtering, using a 3″ metallic Nb target and a DC current at a power of 125 W in a flux of 1 sccm of O_2 and 20 sccm of Ar. The substrate was heated at a temperature of 500°C during the deposition. The thickness of the films was controlled during the growth by a quartz microbalance and calibrated by a stylus profilometer. The films here investigated have a thickness of 150 nm. The optimized procedures to obtain the different dominant stoichiometries are schematically shown in Figure 3.32. After deposition, to obtain a pure Nb_2O_5 film, the sample was annealed using a tube furnace at 600°C in 50% O_2 and 50% N_2 flux at 5 bar for 1 hour. To obtain NbO, the deposited samples were annealed in UHV at P=1×10^{-9} *mbar* at 600°C for 1 h. After reduction, to obtain NbO_2, the NbO samples were annealed at 750°C at P=1×10^{-6} *mbar* of oxygen for 1 h.

3.4.1 XPS measurements

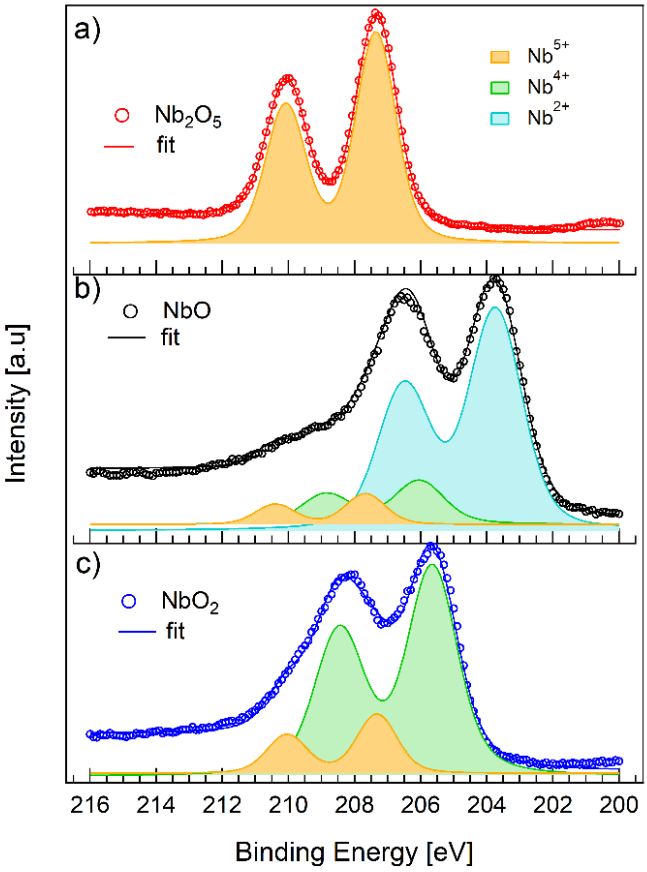

Figure 3.33: *Nb 3d XPS spectra of the niobium oxide film, after the thermal treatments detailed in Figure 3.32, and corresponding fit (solid lines).*

XPS was used to determine the stoichiometry of the samples after the growth and during the treatments by measuring the evolution of the Nb 3d lineshape. The XPS measurements were performed in the Ragno-1 UHV apparatus, which is equipped with a double-anode Mg/Al K_α X-ray source and a hemispherical electron analyzer.

For the present experiments Al K_α photons were used and the XPS spectra were collected at normal emission geometry. Quantitative information on the sample stoichiometry were obtained by fitting the Nb 3d spectra using Nb 3d Voigt shaped doublets with the same width and branching ratio and with different binding energy for each of the three oxide, as in references [200, 201].
The changes in stoichiometry induced in the niobium oxide films by the various thermal treatments can be identified by the modifications in shape of the Nb 3d XPS spectra, shown in Figure 3.33. After growth the films have a dominant Nb_2O_5 stoichiometry. To optimize the Nb_2O_5 stoichiometry the film was heated at 600°C in O_2 and N_2 flux in ambient pressure for 1h. The Nb 3d XPS spectrum (Figure 3.33 a) shows the presence of two well-defined peaks at 210.1 and 207.4 eV, characteristic of the Nb_2O_5 phase[202].
When the as-grown sample is annealed in UHV at 600°C for 1 h the Nb 3d XPS spectrum (Figure 3.33 b) shows a significant change of shape and the two peaks appear at lower binding energies, 205.5 and 203.7 eV, characteristic of the NbO phase [201]. A further annealing of the NbO film at 750°C in an O_2 pressure of $P=1 \times 10 - 6mbar$ for 1 h induces a further change of spectral shape (Figure 3.33 c) with peaks at 208.2 and 205.6 eV, characteristic of the NbO_2 phase[203]. If compared to the peaks of the Nb_2O_5 phase, the peaks of the NbO and NbO_2 films appear broader, they show a different branching ratio and a certain degree of asymmetry towards higher binding energies. These evidences suggest the presence of minority phases, besides the dominant one. The fit of the spectra shows that the Nb_2O_5 film has a 100% Nb^{5+} oxidation state, while the NbO film has a 77% Nb^{2+}, 15% Nb^{4+} and 8% Nb^{5+} concentration, with the minority phases possibly deriving from a non-complete reduction and/or from partial surface oxidation. The NbO_2 film actually has a 82% Nb^{4+} and 18% Nb^{5+} concentration, possibly due to some degree of surface oxidation also in this case as confirmed by XPS grazing spectra. It has to be noted that XPS is a very surface sensitive technique with a probing depth of only a few nm. Therefore, the concentration of the various phases measured by XPS may well be limited to the film surface.

3.4.2 XRD measurements

X-ray diffraction (XRD) was used to characterize the crystallinity of the films and the different structural phases present. The XRD measurements were acquired using a Bragg-Brentano $2\theta - \omega$ apparatus with Cu Kα photons. The radius of the diffraction circle was 240 mm and a proportional point detector was used.
XRD measurements were performed in order to assess the crystallinity of the films. Figure 3.34 reports $2\theta - \omega$ scans for the three different films. The Nb_2O_5 film (Figure 3.34 a) shows various peaks with a very small intensity, that can be related to the simultaneous presence of different crystallographic phases, a monoclinic, an orthorombic and a tetragonal phase, in agreement with the literature[203]. The NbO film (Figure 3.34 b) shows significantly more intense NbO-related peaks, as compared to the Nb_2O_5 phase, possibly deriving from a higher degree of crystallinity. The most intense peak at 41° can be ascribed to NbO (200), the intermediate intensity peak at 36° to NbO (111) and the low intensity peak at 61° to NbO (220) (JCPDS 00-043-1290). The XRD pattern of the NbO_2 film is shown in Figure 3.34 c. The most intense peak at 26° can be related to NbO_2 (400) (JCPDS 01-071-0020). The other peaks with a markedly lower intensity can be related to minority amounts

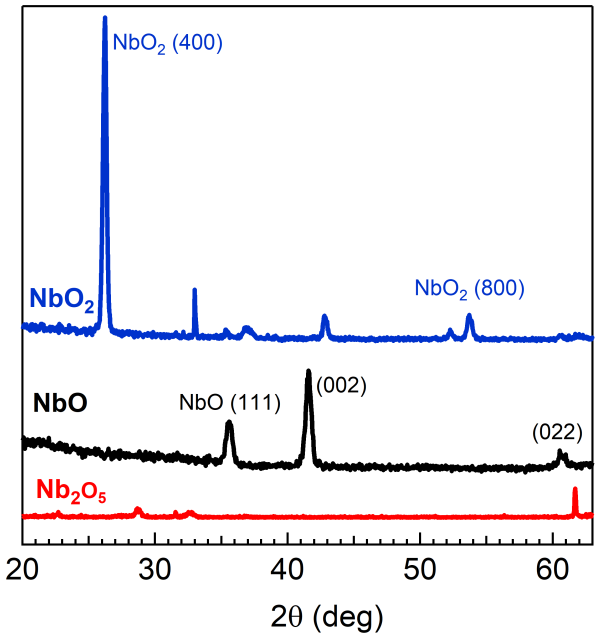

Figure 3.34: *XRD θ-2θ scans acquired on the niobium oxide film, after the thermal treatments detailed in Figure 3.32*

of NbO and Nb_2O_5 phases, the former possibly originating from a non-complete re-oxidation and the latter likely formed on the surface due to the short air exposure necessary to transfer the sample to the XRD apparatus. The XRD spectra confirm the expected polycrystalline nature of the films, and the absence of a preferential orientation except for the case of NbO_2 film, in which the microcrystals have a preferential (400) texturing.

3.4.3 UV-Visible absorption spectroscopy

UV-Vis spectrophotometry was used to assess the optical absorptance of the samples. In this study the optical properties of the samples are studied in a wavelength range from 250 to 800 nm. After the monochromator, a linear polarizer is used to select light with s polarization. A silicon photodetector is used to measure the intensity of the light transmitted or reflected by the sample. In the geometry used during the experiment, the sample normal forms an angle of 22° with the incident light. The transmittance T and reflectance R are measured and the absorptance A is obtained as $A = 1 - (T + R)$.
The UV-Vis absorptance spectra of the films are shown in Figure 3.35. The Nb_2O_5 film presents an absorptance peak in the near UV with a maximum at 300-350 nm, related to transitions from the O 2p valence band to the Nb 4d conduction band. At higher wavelengths the absorptance decreases reaching values below 0.2 at 800 nm. The overall behavior is consistent with the trend observed in the literature for Nb_2O_5 reference compounds[204]. The spectrum shows some additional oscillations that are ascribed to interference effects, often observed in slightly absorbing thin films[205]. The UV-Vis spectra of the NbO and NbO_2 films expectedly show a much higher absorptance in the visible range than the Nb_2O_5film.

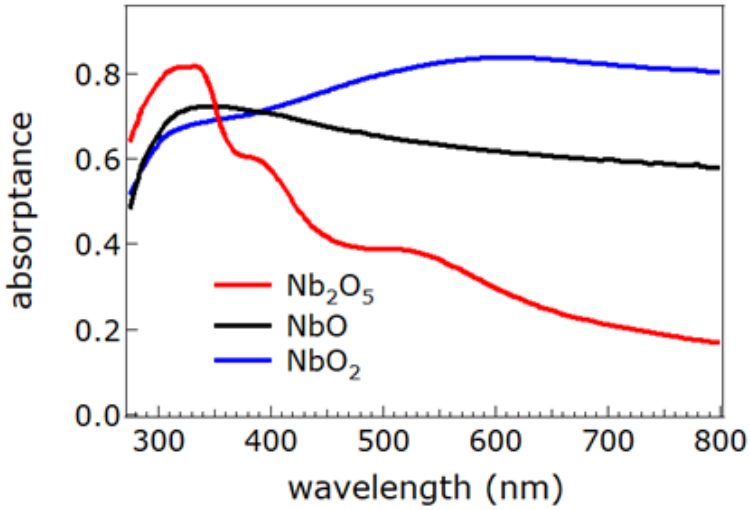

Figure 3.35: *UV-Visible absorptance spectra of the niobium oxide film, after the thermal treatments detailed in Figure 3.32*

In particular, the NbO film shows a maximum above 300 nm and a mild decrease of absorptance at higher wavelengths in the visible range. In the NbO_2 sample case the absorptance slightly increases in the 300-600 nm range and it decreases smoothly at higher wavelengths, in agreement with previous works on NbO_2 films[206].

3.4.4 SEM images

A Scanning Electron microscope (SEM) with a field emission gun was used to image the surface morphology of the samples.

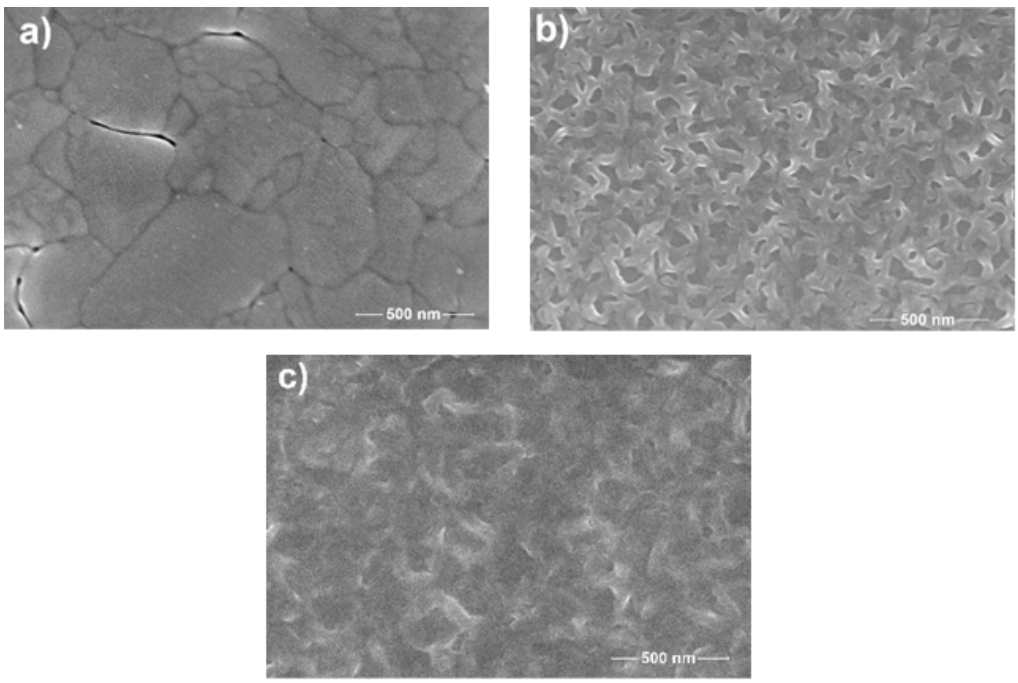

Figure 3.36: *SEM images acquired on the niobium oxide film, after the thermal treatments detailed in Figure 3.32: a) Nb_2O_5 b) NbO and c) NbO_2.*

Figure 3.36 shows the SEM images of the surface morphology of the three films. The Nb_2O_5 film (Figure 3.36a) shows a non-uniform granular surface morphology with grains having a lateral size largely variable from tens of nm to several hundreds of nm and an irregular shape, induced by the thermal treatment at 600°C in O_2 flow. The heat treatment at the same temperature in vacuum, that leads to NbO formation, instead leads to a significantly different surface morphology (Figure 3.36b), with regular interconnected maze-like domains with a width of the order of 100 nm and dense irregular holes of comparable size. The NbO_2 film (Figure 3.36 c) has a similar surface morphology as the NbO film, although the contrast of the SEM image is lower than in Figure 3.36 b, showing that the oxidation in UHV-compatible conditions at slightly higher temperatures (750° C) does not significantly alter the surface morphology.

3.4.5 XANES measurements at EuXFEL

The XANES measurements were performed at the FXE instrument of the European XFEL facility[207, 208]. The XFEL pulse was delivered in train mode, using 20 pulses per train at a repetition rate of 282 kHz and 10 trains per second, i.e., 200 pulses per second. The pulse energy was $\sim 450\ \mu J$. The two-bounce Si(111) monochromator provided a monochromatic beam with energy resolution $\Delta E/E \sim 10^{-4}$ and the incoming beam flux was $\sim 10^9$ photons/pulse. The photon energy was scanned across the near range of the Nb K-edge (18970-19040 eV). The beam was focused by compound refractive lens to a spot size of $\sim 20\ \mu$m. The incoming beam intensity was measured by monitoring the scattering signal from a thin Kapton film. The XANES measurements were performed at room temperature in total fluorescence yield. Biased PN diodes and digitizer (2 Gs/s, 12 bits) were employed as the detection system, and a Zr filter with uT ~ 3 was installed in front of the fluorescence diode sensor. The correlation between the incoming pulse intensity and fluorescence signal was checked before the XANES measurement. Due to the stochastics of XFEL pulses the monochromatic beam intensity fluctuates from pulse to pulse, so low and high thresholds were applied to process the XANES spectrum from the digitizer raw data.

Figure 3.37 shows the Nb K-edge XANES spectra of the film after oxidation in O_2/N_2 flux (Nb_2O_5) and after UHV reduction and reoxidation in UHV-compatible oxygen partial pressure (NbO_2). In the Nb_2O_5 spectrum a broad pre-edge feature (A in Figure 3.37) is visible at 18.995 keV, ascribed to dipole–forbidden 1s $\rightarrow$ 4d transitions that become allowed due to local structural distortions that break the inversion symmetry and by the hybridization between the Nb 4d and 5p levels and the O 2p levels[209] . The two relatively broad and intense edge features (B and C in Figure 3.37) are related to 1s $\rightarrow$ 4p transitions, in which the absorption coefficient of Nb is modulated by scattering effects involving the second and the first coordination shell of the Nb atom respectively[210, 211]. The overall shape of the spectrum shown in Figure 3.37 is compatible with the spectrum measured on reference Nb_2O_5 powders and with those reported in the literature for Nb_2O_5[212, 213]. In the XANES spectrum of the film obtained by UHV reduction and reoxidation in UHV-compatible oxygen partial pressure conditions, the A pre-edge feature, if present, is closer to the edge structures and it cannot be resolved from the B feature. Overall, the spectrum is compatible with those observed in the literature for NbO_2 films[212, 213]. The comparison between XANES and XPS spectra allows to have information

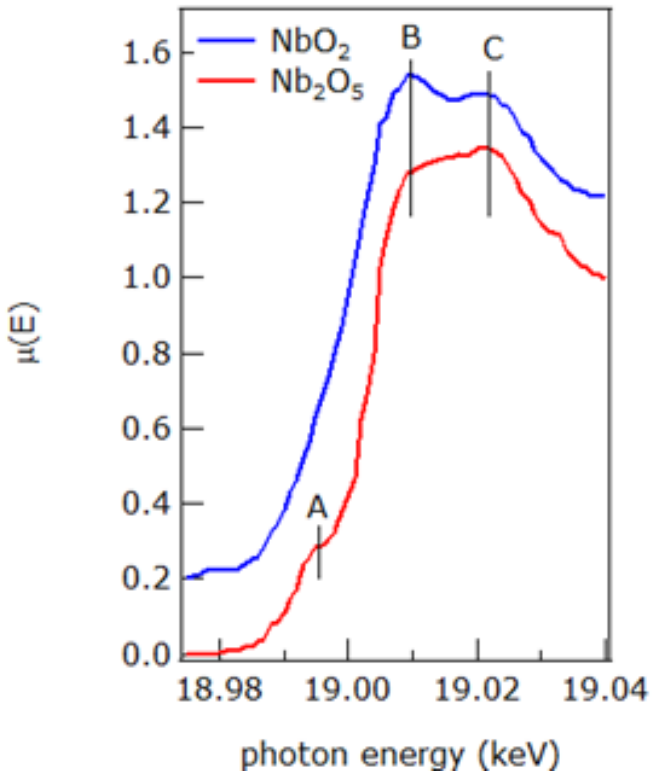

Figure 3.37: *Nb K-edge XANES spectra of the film after oxidation in O2/N2 flux (blue curve) and after UHV reduction and reoxidation in UHV-compatible oxygen partial pressure (red spectrum), as detailed in Figure 3.32.*

on the differences in composition of the film bulk and surface. XANES measurements at the Nb-K edge are in fact sensitive to the whole film thickness due to the large probing depth of high energy X-rays, while XPS with Al Kα photons is a very surface sensitive technique with a probing depth limited to a few nm. The XANES spectrum of the NbO_2 film, showing features related to Nb^{4+} ions, indicates that the non-negligible concentration of Nb^{5+} ions observed by XPS in the NbO_2 film is confined on the film surface and it has a negligible weight when the whole film is probed. The energy resolution of the XANES spectra shown in Figure 3.37 is limited by the short lifetime of the Nb K-edge core-hole. In spite of this limitation, the XANES spectra are sensitive to the electronic structure of Nb in the two different films. We underline that the spectra in Figure 3.37 have been acquired using ultrashort photon bunches in relatively short times, of the order of 10 min, achieving a signal-to-noise ratio of the order of 10^{-3}. This evidence opens up the possibility of performing pump-probe XANES studies of the dynamic modifications of the electronic structure in such films with sub-ps time resolution, in view for example of assessing the dynamics of photoexcitation in Nb_2O_5 or the light-induced phase transition in NbO_2.

Conclusions

This thesis presents an in-depth study of the properties of Niobium and Cerium Oxides and has provided important information in view of future applications of these materials in photocatalysis or in the production of memresistive electronic components. The samples were grown by magnetron sputtering and MBE and an in-depth study of the growth conditions and post-treatments was necessary to obtain samples with a precise oxidation state and stoichiometry. The samples were characterized by XPS, XRD, SEM and Optical Spectroscopy in order to verify their chemical, optical and morphological characteristics. Then, during experiments carried out at Free Electron Laser and Synchrotrons, X-ray absorption and emission spectroscopies such as EXAFS, XANES and XES were used both in static and pump-probe mode, in order to have information on the electronic properties and of the local atomic structure of the excited states that form when these materials are illuminated by light. The first part of the thesis focuses on the optimization of the growth of cerium oxide films by magnetron sputtering. The radio frequency power, the amount of oxygen in the deposition chamber and the substrate temperature during growth were varied in order to obtain a cerium oxide sample that was completely oxidized, i.e. containing cerium atoms in the Ce^{4+} state. In order to verify the oxidation state of the deposited samples, they were measured by XPS and the spectra thus obtained were fitted in order to measure the concentration of Ce4+ ions in the sample. It can be concluded that an oxygen concentration in the chamber of 75%, a substrate temperature of 300°C and a radio frequency power of 150 W are necessary to obtain a fully oxidized sample. The samples were also measured by UV-Visible spectroscopy, in order to measure their absorption in the optical range and by XRD in order to verify the degree of crystallinity of the grown samples. From the optical absorption spectra, Tauc plots were obtained, which show that the grown samples have a band gap compatible with cerium oxide in the Ce^{4+} oxidation state. Finally, diffraction measurements show that the grown samples are polycrystalline with a preferential orientation in the (111) direction.
The second part of the thesis focuses on the measurements at the European XFEL performed on the cerium oxide samples described in the previous section. The European XFEL is a unique facility for the study of materials properties that uses ultrafast X-ray beams to obtain an element-sensitive characterization of the dynamic evolution of samples upon photoexcitation by X-ray absorption and emission measurements in static and pump-probe mode. The experiment was performed at the FXE beamline and its aim was to study the evolution of the excited state in ceria samples caused by photoexcitation above the band gap. In order to study the excited state in ceria, pump-probe XES XANES and EXAFS measurements were performed. XES was measured at the Ce L_{α} absorption edge, while XANES and EXAFS at the Ce $L_{2,3}$ absorption edge. XES and XANES allowed us to conclude that after the interaction with light a Ce^{3+} type state initially forms; within a characteristic time of 500 fs it decays into a different state with a lifetime of more than

300 ps. The EXAFS measurements allowed, to demonstrate the onset of a local lattice distortion compatible with the one expected in the case of photoinduced polaron formation within a time of the order of a few hundreds of fs and a lifetime greater than 300 ps. The results obtained are important to understand the dynamics of excited states in cerium oxide, which are responsible for the catalysis of reactions such as hydrolysis. A better understanding of these dynamics can lead to the creation of efficient devices for photocatalysis that use cerium oxide as the main catalyst.
In the third part of the thesis, the optimization of a process for the growth of the three stable niobium oxides is presented. Niobium oxide occurs in three main stoichiometries: Nb_2O_5, NbO_2 and NbO, however non-stoichiometric forms also exist, so it is quite challenging to obtain the three phases separately. Samples of niobium oxide were grown by magnetron sputtering and then subjected to post-growth treatments to obtain the different phases of niobium oxide. The study allowed to formulate an optimized procedure for the stabilization of the three phases of the oxide. The growth by magnetron sputtering produces a sample that is mainly formed by Nb_2O_5, that can be completely oxidized to Nb_2O_5 state by a thermal treatment at 600°C for one hour in a tube furnace with a flow of 50% O2 and 50% N2 of 1 bar. Starting from the as-grown sample, it is possible to obtain a 77% NbO sample by annealing it at 600°C for one hour in ultra-high vacuum . Finally, starting from the NbO sample, it is possible to obtain a sample composed of 82% NbO_2 by annealing it at 750°C for one hour at an oxygen pressure $PO_2=1\times10^{-6}$ mbar. The stoichiometry of the obtained samples was obtained by fitting the XPS spectra, and UV-Visible absorption spectroscopy and XRD measurements were also carried out. The former concluded that Nb_2O_5 has an absorption peak in the UV and it is transparent in the visible range. Instead, both NbO and NbO_2 maintain a high light absorption throughout the UV-Visible range, that makes them interesting in view of applications for photocatalysis. From the diffraction measurements it was possible to conclude that Nb_2O_5 is presented in a form characterized by numerous crystallographic phases. Instead NbO_2 and NbO were found to be polycrystalline and to present a single crystallographic phase. NbO_2 presents an intense main (400) peak, while NbO has the most intense (200) and (111) peaks . Finally, the NbO_2 and Nb_2O_5 samples were measured at the European XFEL with XANES spectroscopy. XANES allows to obtain bulk information on the grown film, unlike XPS which instead provides information only on the surface of the sample. The XANES spectra are in agreement with those present in the literature, furthermore, as regards the NbO_2 sample, the measurements confirmed that the Nb_2O_5 phase is present only on the surface of the sample, while the bulk is mainly composed of NbO_2.
In the last part of the thesis, an experiment with a catalytic cell carried out at the APE beamline of the Elettra synchrotron in Trieste is described. For this experiment, samples of undoped and Cu-doped CeO_2 were grown by MBE. The experiment carried out at Elettra consisted in measuring the $M_{4,5}$ absorption threshold of Ce by XANES, while the samples were illuminated by a laser and exposed to a water environment while the temperature was increased from 100°C to 300°C. Furthermore, micro gas chromatography measurements were acquired, in order to measure the gases produced and identify the occurrence or not of photocatalytic reactions caused by the samples illuminated by the laser. The XANES spectra were then fitted using Ce^{3+} and Ce^{4+} references in order to obtain the concentration of Ce^{3+} ions in the sample. The results obtained show that for the undoped sample and the 5% Cu-doped one there is an increase in the Ce^{3+} concentrations but this does not depend on the presence of light illumination , indicating that in these samples pho-

tocatalytic reactions with the surrounding water are not activated. However, micro gas chromatography shows some H_2 production after 270°C, probably favored by oxygen vacancies and oxide reduction induced by the increasing temperature. The 11% Cu-doped sample instead shows different increasing Ce^{3+} concentrations with the laser on and off, indicating an effect of the laser together with temperature in the oxide reduction. Furthermore the production of H_2 begins at 250°C with laser on, which means that the laser causes the start of photocatalytic water dissociation and subsequent H_2 formation, correlated to the oxide oxidation due to charge transfer to the H and vacancies compensation with the O remaining on the surface.
To conclude I indicate some future perspectives of the experiments discussed in this thesis.
The XFEL experiment on cerium oxide films can be further extended using films coupled with different metal species such as Cu, both in form of doping and nanoparticles, comparing the lifetimes of the excited charges and of the polaron with those obtained with the undoped cerium oxide film. The aim is to try to correlate the dynamics with the photocatalytic activity of the films. In this direction it will be interesting to extend the study of the photocatalytic activity of ceria films also to the coupling with Cu nanoparticles, to increase the efficiency, improve the effect of light illumination and extend the active optical range to the visible-infrared range where the plasmonic resonance of Cu is excited.
As for the measurements performed on niobium oxides, dynamic XANES pump-probe measurements on NbO_2 and Nb_2O_5 will be performed in the future, to clarify the dynamics in Nb_2O_5 interesting for catalytic applications. In the case of NbO_2 it would be interesting to study the insulator-metal phase transition using the visible laser pump.

Acknowledgements

The work and the results described in this thesis wouldn't have been possible without the support and advices given to me by people in the SESAMo research group. Firstly, a special thank goes to my supervisor, Dr. Paola Luches for her continuous guidance and support and for being always available whenever I needed advices. I would also like to thank Dr. Stefania Benedetti and Dr. Alessandro Di Bona, for teaching me the magnetron sputtering deposition technique and X-ray Powder Diffraction and giving me helpful advices through the PhD. I want also to thank Eleonora Spurio, with whom I have performed the beamtimes at XFEL and APE and the sample fabrication and characterization at SESAMo, and Sergio D'Addato for his helpful advices.
During my PhD, I also collaborated with people from other research groups, whose help and support helped me in these years. I would like to thank Daniele, Patrick and Stefano from the "i romani" group. I want also to thank the people at APE beamline: Silvia, Piero and Mario.
A special thank goes to the people working at the FXE beamline at the European XFEL: Frederico, Yifeng, Xinchao, Chris, Yohei and many others. There I have performed two beamtimes and I was welcomed for three months for my period abroad to participate in numerous beamtimes and learn X-ray Absorption and Emission techniques at the Free Electron Laser.
I would like to thank my PhD colleagues and Post-Docs from CNR and UNIMORE in Modena for their support and help and for sharing numerous lunch breaks with me during my PhD. I want to also thank my friends who supported me in these three years.
Finally last, but not least, my parents Marco and Antonella and my brother Simone, for always supporting me and being by my side, in my studies as in any other moment of my life.

Bibliography

[1] William F Lamb et al. "A review of trends and drivers of greenhouse gas emissions by sector from 1990 to 2018". In: *Environmental research letters* 16.7 (2021), p. 073005.

[2] Stephane de la Rue du Can, Lynn Price, and Timm Zwickel. "Understanding the full climate change impact of energy consumption and mitigation at the end-use level: A proposed methodology for allocating indirect carbon dioxide emissions". In: *Applied Energy* 159 (2015), pp. 548–559.

[3] Jan C Minx et al. "A comprehensive dataset for global, regional and national greenhouse gas emissions by sector 1970–2019". In: *Earth System Science Data Discussions* 2021 (2021), pp. 1–63.

[4] IEA. *Energy Efficiency 2020*. 2020.

[5] Priyadarshi R Shukla et al. "Climate change 2022: Mitigation of climate change". In: *Contribution of working group III to the sixth assessment report of the Intergovernmental Panel on Climate Change* 10 (2022), p. 9781009157926.

[6] George Xydis. "On the exergetic capacity factor of a wind–solar power generation system". In: *Journal of Cleaner Production* 47 (2013), pp. 437–445.

[7] Seyed Hossein Madaeni, Ramteen Sioshansi, and Paul Denholm. "Comparing capacity value estimation techniques for photovoltaic solar power". In: *IEEE Journal of Photovoltaics* 3.1 (2012), pp. 407–415.

[8] Michael G Walter et al. "Solar water splitting cells". In: *Chemical reviews* 110.11 (2010), pp. 6446–6473.

[9] J Nowotny et al. "Solar-hydrogen: environmentally safe fuel for the future". In: *International journal of hydrogen energy* 30.5 (2005), pp. 521–544.

[10] Tehmeena Ishaq et al. "A perspective on possible amendments in semiconductors for enhanced photocatalytic hydrogen generation by water splitting". In: *international journal of hydrogen energy* 46.79 (2021), pp. 39036–39057.

[11] Michael G Walter et al. "Solar water splitting cells". In: *Chemical reviews* 110.11 (2010), pp. 6446–6473.

[12] Jin Hyun Kim et al. "Toward practical solar hydrogen production–an artificial photosynthetic leaf-to-farm challenge". In: *Chemical Society Reviews* 48.7 (2019), pp. 1908–1971.

[13] Akihiko Kudo and Yugo Miseki. "Heterogeneous photocatalyst materials for water splitting". In: *Chemical Society Reviews* 38.1 (2009), pp. 253–278.

[14] Kazuhiko Maeda. "Photocatalytic water splitting using semiconductor particles: history and recent developments". In: *Journal of Photochemistry and Photobiology C: Photochemistry Reviews* 12.4 (2011), pp. 237–268.

[15] Nianqiang Wu. “Plasmonic metal–semiconductor photocatalysts and photoelectrochemical cells: a review”. In: *Nanoscale* 10.6 (2018), pp. 2679–2696.

[16] Jin Hyun Kim et al. “Toward practical solar hydrogen production–an artificial photosynthetic leaf-to-farm challenge”. In: *Chemical Society Reviews* 48.7 (2019), pp. 1908–1971.

[17] Bahar Ipek and Deniz Uner. “On the limits of photocatalytic water splitting”. In: *Water Chemistry* (2019), pp. 1–23.

[18] Si Yin Tee et al. “Recent progress in energy-driven water splitting”. In: *Advanced science* 4.5 (2017), p. 1600337.

[19] Linxi Wang and Jiaguo Yu. “Principles of photocatalysis”. In: *Interface science and technology*. Vol. 35. Elsevier, 2023, pp. 1–52.

[20] Mohamed A Hassaan et al. “Principles of photocatalysts and their different applications: a review”. In: *Topics in Current Chemistry* 381.6 (2023), p. 31.

[21] Mohammad Mansoob Khan, Syed Farooq Adil, and Abdullah Al-Mayouf. *Metal oxides as photocatalysts*. 2015.

[22] Steven Y Reece et al. “Wireless solar water splitting using silicon-based semiconductors and earth-abundant catalysts”. In: *science* 334.6056 (2011), pp. 645–648.

[23] Nianqiang Wu. “Plasmonic metal–semiconductor photocatalysts and photoelectrochemical cells: a review”. In: *Nanoscale* 10.6 (2018), pp. 2679–2696.

[24] JunkoáN Kondo et al. “Cu 2 O as a photocatalyst for overall water splitting under visible light irradiation”. In: *Chemical Communications* 3 (1998), pp. 357–358.

[25] Yong-Jun Yuan et al. “Cadmium sulfide-based nanomaterials for photocatalytic hydrogen production”. In: *Journal of Materials Chemistry A* 6.25 (2018), pp. 11606–11630.

[26] Andebet Gedamu Tamirat et al. “Using hematite for photoelectrochemical water splitting: a review of current progress and challenges”. In: *Nanoscale horizons* 1.4 (2016), pp. 243–267.

[27] Lucas M Carneiro et al. “Excitation-wavelength-dependent small polaron trapping of photoexcited carriers in α-Fe2O3”. In: *Nature materials* 16.8 (2017), pp. 819–825.

[28] Akira Fujishima and Kenichi Honda. “Electrochemical photolysis of water at a semiconductor electrode”. In: *nature* 238.5358 (1972), pp. 37–38.

[29] Tomoji Kawai and Tadayoshi Sakata. “Conversion of carbohydrate into hydrogen fuel by a photocatalytic process”. In: *Nature* 286.5772 (1980), pp. 474–476.

[30] L Kavan et al. “Electrochemical and photoelectrochemical investigation of single-crystal anatase”. In: *Journal of the American Chemical Society* 118.28 (1996), pp. 6716–6723.

[31] Ruifeng Qian et al. “Charge carrier trapping, recombination and transfer during TiO2 photocatalysis: An overview”. In: *Catalysis Today* 335 (2019), pp. 78–90.

[32] Kazuhito Hashimoto, Hiroshi Irie, and Akira Fujishima. “TiO2 photocatalysis: a historical overview and future prospects”. In: *Japanese journal of applied physics* 44.12R (2005), p. 8269.

[33] Jacopo Stefano Pelli Cresi et al. “Lifetime of photogenerated positive charges in hybrid cerium oxide-based materials from space and mirror charge effects in time-resolved photoemission spectroscopy”. In: *The Journal of Physical Chemistry C* 126.27 (2022), pp. 11174–11181.

[34] Maria Chiara Spadaro et al. “Morphology, structural properties and reducibility of size-selected CeO2- x nanoparticle films”. In: *Beilstein Journal of Nanotechnology* 6.1 (2015), pp. 60–67.

[35] NV Skorodumova et al. “Quantum origin of the oxygen storage capability of ceria”. In: *Physical Review Letters* 89.16 (2002), p. 166601.

[36] Kisung Lee et al. “Strategies to improve the photocatalytic activity of TiO 2: 3D nanostructuring and heterostructuring with graphitic carbon nanomaterials”. In: *Nanoscale* 11.15 (2019), pp. 7025–7040.

[37] Hao-Bo Li et al. “Electronic structure and ferromagnetism modulation in Cu/Cu2O interface: impact of interfacial Cu vacancy and its diffusion”. In: *Scientific Reports* 5.1 (2015), p. 15191.

[38] Chunming Yang et al. “Defect engineering on CeO2-based catalysts for heterogeneous catalytic applications”. In: *Small Structures* 2.12 (2021), p. 2100058.

[39] Mohammad Mansoob Khan et al. “Defect-induced band gap narrowed CeO2 nanostructures for visible light activities”. In: *Industrial & Engineering Chemistry Research* 53.23 (2014), pp. 9754–9763.

[40] Du Ang Dao Channei et al. “Photocatalytic activity of Cu-doped cerium dioxide nanoparticles”. In: *Key Engineering Materials* 751 (2017), pp. 801–806.

[41] Mahdi Kazazi, Banafsheh Moradi, and Mehdi Delshad Chermahini. “Enhanced photocatalytic degradation of methyl orange using Ag/Sn-doped CeO 2 nanocomposite”. In: *Journal of Materials Science: Materials in Electronics* 30 (2019), pp. 6116–6126.

[42] RM Mohamed, DL McKinney, and WM Sigmund. “Enhanced nanocatalysts”. In: *Materials Science and Engineering: R: Reports* 73.1 (2012), pp. 1–13.

[43] D Channei et al. “Photocatalytic degradation of methyl orange by CeO2 and Fe–doped CeO2 films under visible light irradiation”. In: *Scientific Reports* 4.1 (2014), p. 5757.

[44] Tiziano Montini et al. “Fundamentals and catalytic applications of CeO2-based materials”. In: *Chemical reviews* 116.10 (2016), pp. 5987–6041.

[45] Zhengyi Hu et al. “Rare Earth Elements in Soils”. In: *Communications in Soil Science and Plant Analysis* 37.9-10 (2006), pp. 1381–1420. DOI: 10.1080/00103620600628680. URL: https://doi.org/10.1080/00103620600628680.

[46] Cedric Bouzigues, Thierry Gacoin, and Antigoni Alexandrou. “Biological Applications of Rare-Earth Based Nanoparticles”. In: *ACS Nano* 5.11 (2011). PMID: 21981700, pp. 8488–8505. DOI: 10.1021/nn202378b. eprint: https://doi.org/10.1021/nn202378b. URL: https://doi.org/10.1021/nn202378b.

[47] Jessica T Dahle and Yuji Arai. "Environmental geochemistry of cerium: applications and toxicology of cerium oxide nanoparticles". In: *International journal of environmental research and public health* 12.2 (2015), pp. 1253–1278.

[48] Xiaoyan Cao and Michael Dolg. "Theoretical prediction of the second to fourth actinide ionization potentials". In: *Molecular Physics* 101.7 (2003), pp. 961–969.

[49] David A Atwood. *The rare earth elements: fundamentals and applications*. John Wiley & Sons, 2013.

[50] Martyn V Twigg. "Catalytic control of emissions from cars". In: *Catalysis Today* 163.1 (2011), pp. 33–41.

[51] Masatomo Yashima et al. "High-temperature neutron powder diffraction study of cerium dioxide CeO2 up to 1770 K". In: *Chemical physics letters* 372.5-6 (2003), pp. 784–787.

[52] Alessandro Trovarelli and Paolo Fornasiero. *Catalysis by ceria and related materials*. 2nd. IMPERIAL COLLEGE PRESS, 2013. ISBN: 9781848169630 (print version).

[53] Paola Luches and Sergio Valeri. "Structure, morphology and reducibility of epitaxial cerium oxide ultrathin films and nanostructures". In: *Materials* 8.9 (2015), pp. 5818–5833.

[54] Y Su. "A quantum chemical study of environmental catalysis at the metal-ceria interface". In: (2019).

[55] JoséC Conesa. "Computer modeling of surfaces and defects on cerium dioxide". In: *Surface Science* 339.3 (1995), pp. 337–352.

[56] P Luches, F Pagliuca, and Sergio Valeri. "Morphology, stoichiometry, and interface structure of CeO2 ultrathin films on Pt (111)". In: *The Journal of Physical Chemistry C* 115.21 (2011), pp. 10718–10726.

[57] F Šutara et al. "Epitaxial growth of continuous CeO2 (111) ultra-thin films on Cu (111)". In: *Thin Solid Films* 516.18 (2008), pp. 6120–6124.

[58] Lap Hong Chan and Junji Yuhara. "Growth and structure of ultrathin cerium oxide films on Rh (111)". In: *The Journal of Chemical Physics* 143.7 (2015).

[59] Shuguo Ma, Jose Rodriguez, and Jan Hrbek. "STM study of the growth of cerium oxide nanoparticles on Au (1 1 1)". In: *Surface science* 602.21 (2008), pp. 3272–3278.

[60] Noemi Bosio, Andreas Schaefer, and Henrik Grönbeck. "Can oxygen vacancies in ceria surfaces be measured by O1s photoemission spectroscopy?" In: *Journal of Physics: Condensed Matter* 34.17 (2022), p. 174004.

[61] NV Skorodumova et al. "Quantum origin of the oxygen storage capability of ceria". In: *Physical Review Letters* 89.16 (2002), p. 166601.

[62] Zongxian Yang et al. "Atomic and electronic structure of unreduced and reduced CeO 2 surfaces: A first-principles study". In: *The Journal of chemical physics* 120.16 (2004), pp. 7741–7749.

[63] M Veronica Ganduglia-Pirovano, Juarez LF Da Silva, and Joachim Sauer. "Density-Functional Calculations of the Structure of Near-Surface Oxygen Vacancies¡? format?¿ and Electron Localization on CeO 2 (111)". In: *Physical review letters* 102.2 (2009), p. 026101.

[64] Hui-Ying Li et al. “Multiple configurations of the two excess 4 f electrons on defective CeO 2 (111): Origin and implications”. In: *Physical Review B—Condensed Matter and Materials Physics* 79.19 (2009), p. 193401.

[65] Jan-Frederik Jerratsch et al. “Electron localization in defective ceria films: A study with scanning-tunneling microscopy and density-functional theory”. In: *Physical review letters* 106.24 (2011), p. 246801.

[66] Michael Nolan. “Enhanced oxygen vacancy formation in ceria (111) and (110) surfaces doped with divalent cations”. In: *Journal of Materials Chemistry* 21.25 (2011), pp. 9160–9168.

[67] Zhenpeng Hu and Horia Metiu. “Effect of dopants on the energy of oxygen-vacancy formation at the surface of ceria: Local or global?” In: *The Journal of Physical Chemistry C* 115.36 (2011), pp. 17898–17909.

[68] Zhenpeng Hu et al. “Chemistry of doped oxides: the activation of surface oxygen and the chemical compensation effect”. In: *The Journal of Physical Chemistry C* 115.7 (2011), pp. 3065–3074.

[69] Matthew D Krcha, Adam D Mayernick, and Michael J Janik. “Periodic trends of oxygen vacancy formation and C–H bond activation over transition metal-doped CeO2 (1 1 1) surfaces”. In: *Journal of catalysis* 293 (2012), pp. 103–115.

[70] Zongxian Yang, Tom K Woo, and Kersti Hermansson. “Effects of Zr doping on stoichiometric and reduced ceria: A first-principles study”. In: *The Journal of chemical physics* 124.22 (2006).

[71] Zongxian Yang et al. “Oxygen vacancy formation energy in Pd-doped ceria: A DFT+ U study”. In: *The Journal of chemical physics* 127.7 (2007).

[72] Xiong-Shan Liu et al. “Effects of Fe doping on oxygen vacancy formation and CO adsorption and oxidation at the ceria (111) surface”. In: *Catalysis Communications* 63 (2015), pp. 35–40.

[73] Gabriele Gasperi et al. “Reducibility of Ag-and Cu-Modified Ultrathin Epitaxial Cerium Oxide Films”. In: *The Journal of Physical Chemistry C* 123.22 (2019), pp. 13702–13711.

[74] Giulia Righi, Sara Benedetti, and Rita Magri. “Investigation of the structural and electronic differences between silver and copper doped ceria using the density functional theory”. In: *Journal of Physics: Condensed Matter* 34.20 (2022), p. 204010.

[75] Zhansheng Lu et al. “Cu-doped ceria: Oxygen vacancy formation made easy”. In: *Chemical Physics Letters* 510.1-3 (2011), pp. 60–66.

[76] Avinash Vikatakavi et al. “Interaction of Hydrogen with Cu-Modified Cerium Oxide Surfaces”. In: *The Journal of Physical Chemistry C* 126.44 (2022), pp. 18652–18660.

[77] Botao Qiao et al. “Highly efficient catalysis of preferential oxidation of CO in H2-rich stream by gold single-atom catalysts”. In: *ACS catalysis* 5.11 (2015), pp. 6249–6254.

[78] Fabio R Negreiros, Matteo Farnesi Camellone, and Stefano Fabris. “Effects of thermal fluctuations on the hydroxylation and reduction of ceria surfaces by molecular H2”. In: *The Journal of Physical Chemistry C* 119.37 (2015), pp. 21567–21573.

[79] Eliza Hutter and Janos H Fendler. “Exploitation of localized surface plasmon resonance”. In: *Advanced materials* 16.19 (2004), pp. 1685–1706.

[80] Katherine A Willets and Richard P Van Duyne. “Localized surface plasmon resonance spectroscopy and sensing”. In: *Annu. Rev. Phys. Chem.* 58.1 (2007), pp. 267–297.

[81] César Clavero. “Plasmon-induced hot-electron generation at nanoparticle/metal-oxide interfaces for photovoltaic and photocatalytic devices”. In: *Nature Photonics* 8.2 (2014), pp. 95–103.

[82] Amanda J Haes et al. “Plasmonic materials for surface-enhanced sensing and spectroscopy”. In: *MRS bulletin* 30.5 (2005), pp. 368–375.

[83] Jennifer M Brockman, Bryce P Nelson, and Robert M Corn. “Surface plasmon resonance imaging measurements of ultrathin organic films”. In: *Annual review of physical chemistry* 51.1 (2000), pp. 41–63.

[84] Jian Zhao et al. “Localized surface plasmon resonance for enhanced electrocatalysis”. In: *Chemical Society Reviews* 50.21 (2021), pp. 12070–12097.

[85] Sungi Kim et al. “Nonnoble-metal-based plasmonic nanomaterials: recent advances and future perspectives”. In: *Advanced Materials* 30.42 (2018), p. 1704528.

[86] S Mohapatra et al. “Synthesis of gold-silicon core-shell nanoparticles with tunable localized surface plasmon resonance”. In: *Applied Physics Letters* 92.10 (2008).

[87] Scott K Cushing, Alan D Bristow, and Nianqiang Wu. “Theoretical maximum efficiency of solar energy conversion in plasmonic metal–semiconductor heterojunctions”. In: *Physical Chemistry Chemical Physics* 17.44 (2015), pp. 30013–30022.

[88] Harry A Atwater and Albert Polman. “Plasmonics for improved photovoltaic devices”. In: *Nature materials* 9.3 (2010), pp. 205–213.

[89] D Derkacs et al. “Improved performance of amorphous silicon solar cells via scattering from surface plasmon polaritons in nearby metallic nanoparticles”. In: *Applied Physics Letters* 89.9 (2006).

[90] Hao Zhang, Mohsin Ijaz, and Richard J Blaikie. “Recent review of surface plasmons and plasmonic hot electron effects in metallic nanostructures”. In: *Frontiers of Physics* 18.6 (2023), p. 63602.

[91] Kaifeng Wu et al. “Efficient hot-electron transfer by a plasmon-induced interfacial charge-transfer transition”. In: *Science* 349.6248 (2015), pp. 632–635.

[92] Calvin Boerigter et al. “Evidence and implications of direct charge excitation as the dominant mechanism in plasmon-mediated photocatalysis”. In: *Nature communications* 7.1 (2016), p. 10545.

[93] Cesare Franchini et al. “Polarons in materials”. In: *Nature Reviews Materials* 6.7 (2021), pp. 560–586.

[94] Alexander JE Rettie et al. “Unravelling small-polaron transport in metal oxide photoelectrodes”. In: *The journal of physical chemistry letters* 7.3 (2016), pp. 471–479.

[95] David Emin. *Polarons*. Cambridge University Press, 2012.

[96] Alex J Tanner and Geoff Thornton. “TiO2 polarons in the time domain: implications for photocatalysis”. In: *The Journal of Physical Chemistry Letters* 13.2 (2022), pp. 559–566.

[97] Fabio G Santomauro et al. “Femtosecond X-ray absorption study of electron localization in photoexcited anatase TiO2”. In: *Scientific reports* 5.1 (2015), p. 14834.

[98] Jordan E Katz et al. “Electron small polarons and their mobility in iron (oxyhydr) oxide nanoparticles”. In: *Science* 337.6099 (2012), pp. 1200–1203.

[99] Jacopo Stefano Pelli Cresi et al. “Ultrafast formation of small polarons and the optical gap in CeO2”. In: *The Journal of Physical Chemistry Letters* 11.14 (2020), pp. 5686–5691.

[100] Juarez LF Da Silva et al. “Hybrid functionals applied to rare-earth oxides: The example of ceria”. In: *Physical Review B—Condensed Matter and Materials Physics* 75.4 (2007), p. 045121.

[101] HL Tuller and AS Nowick. “Small polaron electron transport in reduced CeO2 single crystals”. In: *Journal of Physics and Chemistry of Solids* 38.8 (1977), pp. 859–867.

[102] M Veronica Ganduglia-Pirovano, Juarez LF Da Silva, and Joachim Sauer. “Density-Functional Calculations of the Structure of Near-Surface Oxygen Vacancies¡? format?¿ and Electron Localization on CeO 2 (111)”. In: *Physical review letters* 102.2 (2009), p. 026101.

[103] Matthias G Barth, William F McDonough, and Roberta L Rudnick. “Tracking the budget of Nb and Ta in the continental crust”. In: *Chemical geology* 165.3-4 (2000), pp. 197–213.

[104] Norman Neill Greenwood and Alan Earnshaw. “Chemistry of the Elements”. In: Elsevier, 2012, p. 1138.

[105] Wendell S Williams. “Transition metal carbides, nitrides, and borides for electronic applications”. In: *Jom* 49.3 (1997), pp. 38–42.

[106] AJ DeArdo. “Niobium in modern steels”. In: *International Materials Reviews* 48.6 (2003), pp. 371–402.

[107] Friedrich Heisterkamp and Tadeu Carneiro. “Niobium: future possibilities–technology and the market place”. In: *Proceedings of the International Symposium, Niobium, Orlando, FL, USA*. Citeseer. 2001, pp. 2–5.

[108] Hironobu Matsuno et al. “Biocompatibility and osteogenesis of refractory metal implants, titanium, hafnium, niobium, tantalum and rhenium”. In: *Biomaterials* 22.11 (2001), pp. 1253–1262.

[109] ISWE Lindau and William E Spicer. “Oxidation of Nb as studied by the uv-photoemission technique”. In: *Journal of Applied Physics* 45.9 (1974), pp. 3720–3725.

[110] Claudio Nico, T Monteiro, and Manuel PF Graça. “Niobium oxides and niobates physical properties: Review and prospects”. In: *Progress in Materials Science* 80 (2016), pp. 1–37.

[111] K Kovacs et al. “Anodic oxidation of niobium sheets and porous bodies: heat-treatment of the Nb/Nb-oxide system”. In: *Journal of the Electrochemical Society* 150.8 (2003), B361.

[112] AL Bowman et al. “The crystal structure of niobium monoxide”. In: *Acta Crystallographica* 21.5 (1966), pp. 843–843.

[113] Koichi Momma and Fujio Izumi. “VESTA 3 for three-dimensional visualization of crystal, volumetric and morphology data”. In: *Journal of applied crystallography* 44.6 (2011), pp. 1272–1276.

[114] JK Hulm et al. “Superconductivity in the TiO and NbO systems”. In: *Journal of Low Temperature Physics* 7 (1972), pp. 291–307.

[115] Yongjian Qiu, Don Smyth, and Jon Kimmel. “The Stabilization of Niobium-Based Solid Electrolyte Capacitors”. In: *Active and passive electronic components* 25.2 (2002), pp. 201–209.

[116] Cláudio Nico et al. “NbO/Nb2O5 core–shells by thermal oxidation”. In: *Journal of the European Ceramic Society* 33.15-16 (2013), pp. 3077–3083.

[117] AK Cheetham and CNR Rao. “A neutron diffraction study of niobium dioxide”. In: *Structural Science* 32.5 (1976), pp. 1579–1580.

[118] Adrian A Bolzan et al. “A powder neutron diffraction study of semiconducting and metallic niobium dioxide”. In: *Journal of Solid State Chemistry* 113.1 (1994), pp. 9–14.

[119] AX Gray et al. “Correlation-driven insulator-metal transition in near-ideal vanadium dioxide films”. In: *Physical review letters* 116.11 (2016), p. 116403.

[120] FJ Morin. “Oxides which show a metal-to-insulator transition at the Neel temperature”. In: *Physical review letters* 3.1 (1959), p. 34.

[121] RF Janninck and DH Whitmore. “Electrical conductivity and thermoelectric power of niobium dioxide”. In: *Journal of Physics and Chemistry of Solids* 27.6-7 (1966), pp. 1183–1187.

[122] Denis Music, Andreas M Krause, and Pär AT Olsson. “Theoretical and experimental aspects of current and future research on NbO2 thin film devices”. In: *Crystals* 11.2 (2021), p. 217.

[123] Melissa R Beebe et al. “Time-resolved light-induced insulator-metal transition in niobium dioxide and vanadium dioxide thin films”. In: *Optical Materials Express* 7.1 (2016), pp. 213–223.

[124] Rakesh Rana et al. “Nonthermal nature of photoinduced insulator-to-metal transition in NbO 2”. In: *Physical Review B* 99.4 (2019), p. 041102.

[125] Andrew O’Hara and Alexander A Demkov. “Nature of the metal-insulator transition in Nb O 2”. In: *Physical Review B* 91.9 (2015), p. 094305.

[126] Linsong Huang et al. “NbO2 electrocatalyst toward 32% faradaic efficiency for N2 fixation”. In: *Small Methods* 3.6 (2019), p. 1800386.

[127] K Sasaki, L Zhang, and RR Adzic. “Niobium oxide-supported platinum ultralow amount electrocatalysts for oxygen reduction”. In: *Physical Chemistry Chemical Physics* 10.1 (2008), pp. 159–167.

[128] Harald Schäfer, R Gruehn, and F Schulte. “The modifications of niobium pentoxide”. In: *Angewandte Chemie International Edition in English* 5.1 (1966), pp. 40–52.

[129] Georg Brauer. “Die oxyde des niobs”. In: *Zeitschrift für anorganische und allgemeine Chemie* 248.1 (1941), pp. 1–31.

[130] David Bach. “EELS investigations of stoichiometric niobium oxides and niobium-based capacitors”. In: (2009).

[131] Kaupo Kukli, Mikko Ritala, and Markku Leskelä. “Development of dielectric properties of niobium oxide, tantalum oxide, and aluminum oxide based nanolayered materials”. In: *Journal of the Electrochemical Society* 148.2 (2001), F35.

[132] Marjeta Maček and Boris Orel. “Electrochromism of sol–gel derived niobium oxide films”. In: *Solar energy materials and solar cells* 54.1-4 (1998), pp. 121–130.

[133] Izabela Nowak and Maria Ziolek. “Niobium compounds: preparation, characterization, and application in heterogeneous catalysis”. In: *Chemical Reviews* 99.12 (1999), pp. 3603–3624.

[134] Mei-Qiang Fan et al. “The catalytic effect of additive Nb2O5 on the reversible hydrogen storage performances of LiBH4–MgH2 composite”. In: *International journal of hydrogen energy* 33.1 (2008), pp. 74–80.

[135] Krishna Seshan. *Handbook of thin film deposition*. William Andrew, 2012.

[136] WD Westwood. “Glow discharge sputtering”. In: *Progress in Surface Science* 7.2 (1976), pp. 71–111.

[137] Peter J Kelly and R Derek Arnell. “Magnetron sputtering: a review of recent developments and applications”. In: *Vacuum* 56.3 (2000), pp. 159–172.

[138] Donald M Mattox and Vivienne Harwood Mattox. “50 Years of Vacuum Coating Technology and the growth of the Society of Vacuum Coaters”. In: Society of Vacuum Coaters. 2007.

[139] K Ellmer et al. “Low Temperature Plasmas. Fundamentals, Technologies and Techniques”. In: (2008).

[140] Klaus Ellmer and Thomas Welzel. “Reactive magnetron sputtering of transparent conductive oxide thin films: Role of energetic particle (ion) bombardment”. In: *Journal of Materials Research* 27.5 (2012), pp. 765–779.

[141] VV Felmetsger, PN Laptev, and SM Tanner. “Design, operation mode, and stress control capability of S-Gun magnetron for ac reactive sputtering”. In: *Surface and Coatings Technology* 204.6-7 (2009), pp. 840–844.

[142] John A Thornton. “Magnetron sputtering: basic physics and application to cylindrical magnetrons”. In: *Journal of Vacuum Science and Technology* 15.2 (1978), pp. 171–177.

[143] J Musil et al. “Reactive magnetron sputtering of thin films: present status and trends”. In: *Thin solid films* 475.1-2 (2005), pp. 208–218.

[144] Settimio Mobilio, Federico Boscherini, Carlo Meneghini, et al. *Synchrotron Radiation*. Springer, 2016.

[145] R Dingle et al. “Stimulated emission and laser action in gallium nitride”. In: *Applied Physics Letters* 19.1 (1971), pp. 5–7.

[146] George Brown et al. “Wiggler and undulator magnets—A review”. In: *Nuclear Instruments and Methods in Physics Research* 208.1-3 (1983), pp. 65–77.

[147] VA Solé et al. “Undulator QEXAFS at the ESRF beamline ID26”. In: *Journal of Synchrotron Radiation* 6.3 (1999), pp. 174–175.

[148] G Margaritondo and Primoz Rebernik Ribic. “A simplified description of X-ray free-electron lasers”. In: *Journal of synchrotron radiation* 18.2 (2011), pp. 101–108.

[149] Ian Robinson, Gerhard Gruebel, and Simon Mochrie. “Focus on X-ray beams with high coherence”. In: *New Journal of Physics* 12.3 (2010), p. 035002.

[150] Christopher Behrens et al. “Few-femtosecond time-resolved measurements of X-ray free-electron lasers”. In: *Nature communications* 5.1 (2014), p. 3762.

[151] Margherita Maiuri, Marco Garavelli, and Giulio Cerullo. “Ultrafast spectroscopy: State of the art and open challenges”. In: *Journal of the American Chemical Society* 142.1 (2019), pp. 3–15.

[152] European XFEL. *European XFEL timeline*. `https://www.xfel.eu/facility/overview/construction/timeline/index_eng.html`.

[153] Thomas Tschentscher et al. “Photon beam transport and scientific instruments at the European XFEL”. In: *Applied Sciences* 7.6 (2017), p. 592.

[154] R Brinkmann et al. *Design Report: First Stage of the TESLA XFEL Laboratory*. 2002.

[155] Yuhui Li et al. “Magnetic measurement techniques for the large-scale production of undulator segments for the European XFEL”. In: *Synchrotron Radiation News* 28.3 (2015), pp. 23–28.

[156] Winfried Decking and Torsten Limberg. “European XFEL post-TDR description”. In: *XFEL. EU TN-2013-004-01, European XFEL GmbH, Hamburg, Germany* (2013).

[157] Massimo Altarelli, Reinhard Brinkmann, and Majed Chergui. *The European X-ray free-electron laser. Technical design report*. July 2007.

[158] Andreas Galler et al. “Scientific instrument Femtosecond X-ray Experiments (FXE): instrumentation and baseline experimental capabilities”. In: *Journal of synchrotron radiation* 26.5 (2019), pp. 1432–1447.

[159] Guido Palmer et al. “Pump–probe laser system at the FXE and SPB/SFX instruments of the European X-ray Free-Electron Laser Facility”. In: *Journal of synchrotron radiation* 26.2 (2019), pp. 328–332.

[160] European XFEL. *Scientific Instrument FXE*. `https://www.xfel.eu/facility/instruments/fxe/index_eng.html`.

[161] Roberto Alonso-Mori et al. “A multi-crystal wavelength dispersive x-ray spectrometer”. In: *Review of Scientific Instruments* 83.7 (2012).

[162] Uwe Bergmann and Stephen P Cramer. “High-resolution large-acceptance analyzer for x-ray fluorescence and Raman spectroscopy”. In: *Crystal and Multilayer Optics*. Vol. 3448. SPIE. 1998, pp. 198–209.

[163] S Redford et al. “First full dynamic range calibration of the JUNGFRAU photon detector”. In: *Journal of Instrumentation* 13.01 (2018), p. C01027.

[164] Aldoa Mozzanica et al. “The GOTTHARD charge integrating readout detector: design and characterization”. In: *Journal of Instrumentation* 7.01 (2012), p. C01019.

[165] H Abraham and J Lemoine. “Disparition instantanée du phénomène de Kerr”. In: *CR Acad. Sci. Hebd Seances Acad. Sci. D* 129 (1899), pp. 206–208.

[166] Margherita Maiuri, Marco Garavelli, and Giulio Cerullo. "Ultrafast spectroscopy: State of the art and open challenges". In: *Journal of the American Chemical Society* 142.1 (2019), pp. 3–15.

[167] M Chergui. "1.19 ultrafast structural dynamics of biological systems". In: *Comprehensive Biophysics* (2012), pp. 398–424.

[168] Ahmed H Zewail. "Femtochemistry: Atomic-scale dynamics of the chemical bond". In: *The Journal of Physical Chemistry A* 104.24 (2000), pp. 5660–5694.

[169] Ferenc Krausz and Misha Ivanov. "Attosecond physics". In: *Reviews of modern physics* 81.1 (2009), pp. 163–234.

[170] Claude Rulliere et al. *Femtosecond laser pulses*. Springer, 2005.

[171] C Ruckebusch et al. "Comprehensive data analysis of femtosecond transient absorption spectra: A review". In: *Journal of Photochemistry and Photobiology C: Photochemistry Reviews* 13.1 (2012), pp. 1–27.

[172] Jacopo Stefano Pelli Cresi et al. "Highly efficient plasmon-mediated electron injection into cerium oxide from embedded silver nanoparticles". In: *Nanoscale* 11.21 (2019), pp. 10282–10291.

[173] Christian Bressler and Majed Chergui. "Ultrafast X-ray absorption spectroscopy". In: *Chemical reviews* 104.4 (2004), pp. 1781–1812.

[174] Majed Chergui. "Time-resolved X-ray spectroscopies of chemical systems: New perspectives". In: *Structural Dynamics* 3.3 (2016).

[175] G Panaccione et al. "Advanced photoelectric effect experiment beamline at Elettra: A surface science laboratory coupled with Synchrotron Radiation". In: *Review of Scientific Instruments* 80.4 (2009).

[176] Jian Dou et al. "Operando chemistry of catalyst surfaces during catalysis". In: *Chemical Society Reviews* 46.7 (2017), pp. 2001–2027.

[177] Miquel Salmeron and Robert Schlögl. "Ambient pressure photoelectron spectroscopy: A new tool for surface science and nanotechnology". In: *Surface Science Reports* 63.4 (2008), pp. 169–199.

[178] Axel Knop-Gericke et al. "New experimental technique: X-ray absorption spectroscopy detector for in situ studies in the soft X-ray range (250 eV $\leq$ hv $\leq$ 1000 eV) under reaction conditions". In: *Nuclear Instruments and Methods in Physics Research Section A: Accelerators, Spectrometers, Detectors and Associated Equipment* 406.2 (1998), pp. 311–322.

[179] Michael Hävecker et al. "High-Pressure Soft X-Ray Absorption Spectroscopy: A Contribution to Overcoming the "Pressure Gap" in the Study of Heterogeneous Catalytic Processes". In: *Angewandte Chemie International Edition* 37.13-14 (1998), pp. 1939–1942.

[180] Paw Toldbad Kristiansen et al. "Reaction cell for in situ soft x-ray absorption spectroscopy and resonant inelastic x-ray scattering measurements of heterogeneous catalysis up to 1 atm and 250° C". In: *Review of Scientific Instruments* 84.11 (2013).

[181] C Castán-Guerrero et al. "A reaction cell for ambient pressure soft x-ray absorption spectroscopy". In: *Review of Scientific Instruments* 89.5 (2018).

[182] Luca Braglia et al. “Understanding Solid–Gas Reaction Mechanisms by Operando Soft X-Ray Absorption Spectroscopy at Ambient Pressure”. In: *The Journal of Physical Chemistry C* 124.26 (2020), pp. 14202–14212.

[183] Eric Bêche et al. “Ce 3d XPS investigation of cerium oxides and mixed cerium oxide (CexTiyOz)”. In: *Surface and Interface Analysis: An International Journal devoted to the development and application of techniques for the analysis of surfaces, interfaces and thin films* 40.3-4 (2008), pp. 264–267.

[184] P Luches, F Pagliuca, and Sergio Valeri. “Structural and morphological modifications of thermally reduced cerium oxide ultrathin epitaxial films on Pt (111)”. In: *Physical Chemistry Chemical Physics* 16.35 (2014), pp. 18848–18857.

[185] Konstantin I Maslakov et al. “XPS study of ion irradiated and unirradiated CeO2 bulk and thin film samples”. In: *Applied Surface Science* 448 (2018), pp. 154–162.

[186] T Skála et al. “Palladium interaction with CeO2, Sn–Ce–O and Ga–Ce–O layers”. In: *Journal of Physics: Condensed Matter* 21.5 (2008), p. 055005.

[187] Tomáš Skála et al. “Cerium oxide stoichiometry alteration via Sn deposition: Influence of temperature”. In: *Journal of Electron Spectroscopy and Related Phenomena* 169.1 (2009), pp. 20–25.

[188] Jan Tauc. “Optical properties and electronic structure of amorphous Ge and Si”. In: *Materials research bulletin* 3.1 (1968), pp. 37–46.

[189] Patrycja Makuła, Michał Pacia, and Wojciech Macyk. *How to correctly determine the band gap energy of modified semiconductor photocatalysts based on UV–Vis spectra*. 2018.

[190] J Tauc, Radu Grigorovici, and Anina Vancu. “Optical properties and electronic structure of amorphous germanium”. In: *physica status solidi (b)* 15.2 (1966), pp. 627–637.

[191] Jacques I Pankove. *Optical processes in semiconductors*. Courier Corporation, 1975.

[192] Antonio Ricardo Zanatta. “Revisiting the optical bandgap of semiconductors and the proposal of a unified methodology to its determination”. In: *Scientific reports* 9.1 (2019), p. 11225.

[193] Donald F Swinehart. “The beer-lambert law”. In: *Journal of chemical education* 39.7 (1962), p. 333.

[194] Jean-Henri Lambert. *Photometria sive de mensura et gradibus luminis, colorum et umbrae*. Sumptibus viduae Eberhardi Klett, typis Christophori Petri Detleffsen, 1760.

[195] AV Prokofiev, AI Shelykh, and BT Melekh. “Periodicity in the band gap variation of Ln2X3 (X= O, S, Se) in the lanthanide series”. In: *Journal of alloys and compounds* 242.1-2 (1996), pp. 41–44.

[196] M Isik, S Delice, and NM Gasanly. “Temperature dependence of band gap of CeO2 nanoparticle photocatalysts”. In: *Physica E: Low-dimensional Systems and Nanostructures* 150 (2023), p. 115712.

[197] René Kopelent et al. “X-ray emission spectroscopy: highly sensitive techniques for time-resolved probing of cerium reactivity under catalytic conditions”. In: *Physical Chemistry Chemical Physics* 18.47 (2016), pp. 32486–32493.

[198] Bruce Ravel and MATHENA Newville. “ATHENA, ARTEMIS, HEPHAESTUS: data analysis for X-ray absorption spectroscopy using IFEFFIT”. In: *Journal of synchrotron radiation* 12.4 (2005), pp. 537–541.

[199] W Gawelda et al. “Structural analysis of ultrafast extended x-ray absorption fine structure with subpicometer spatial resolution: Application to spin crossover complexes”. In: *The Journal of chemical physics* 130.12 (2009).

[200] BR King et al. “Kinetic measurements of oxygen dissolution into niobium substrates: In situ X-ray photoelectron spectroscopy studies”. In: *Thin Solid Films* 192.2 (1990), pp. 351–369.

[201] M Grundner and J Halbritter. “XPS and AES studies on oxide growth and oxide coatings on niobium”. In: *Journal of Applied Physics* 51.1 (1980), pp. 397–405.

[202] Toyanath Joshi et al. “Preparation, characterization, and electrical properties of epitaxial NbO2 thin film lateral devices”. In: *Journal of Physics D: Applied Physics* 48.33 (2015), p. 335308.

[203] Nazmul Hossain et al. “Structural and physical properties of NbO 2 and Nb 2 O 5 thin films prepared by magnetron sputtering”. In: *Journal of Materials Science: Materials in Electronics* 30 (2019), pp. 9822–9835.

[204] Subia Ambreen et al. “Effect of chelation in alkoxide precursors of niobium oxide nanoparticles on photochemical degradation of rhodamine B”. In: *Journal of Sol-Gel Science and Technology* 98 (2021), pp. 319–334.

[205] Tatiana V Amotchkina et al. “Oscillations in spectral behavior of total losses (1- R- T) in thin dielectric films”. In: *Optics express* 20.14 (2012), pp. 16129–16144.

[206] Shoichiro Nakao et al. “Structural, electrical, and optical properties of polycrystalline NbO2 thin films grown on glass substrates by solid phase crystallization”. In: *physica status solidi (a)* 214.3 (2017), p. 1600604.

[207] Dmitry Khakhulin et al. “Ultrafast X-ray photochemistry at European XFEL: capabilities of the femtosecond X-ray experiments (FXE) instrument”. In: *Applied Sciences* 10.3 (2020), p. 995.

[208] Andreas Galler et al. “Scientific instrument Femtosecond X-ray Experiments (FXE): instrumentation and baseline experimental capabilities”. In: *Journal of synchrotron radiation* 26.5 (2019), pp. 1432–1447.

[209] Kendra Getty, Mario Ulises Delgado-Jaime, and Pierre Kennepohl. “Assignment of pre-edge features in the Ru K-edge X-ray absorption spectra of organometallic ruthenium complexes”. In: *Inorganica chimica acta* 361.4 (2008), pp. 1059–1065.

[210] Quentin Bollaert et al. “Atomic-scale environment of niobium in ore minerals as revealed by XANES and EXAFS at the Nb K-edge”. In: *European Journal of Mineralogy* 36.1 (2024), pp. 55–72.

[211] Quentin Bollaert et al. “Atomic-scale environment of niobium in ore minerals as revealed by XANES and EXAFS at the Nb K-edge”. In: *European Journal of Mineralogy* 36.1 (2024), pp. 55–72.

[212] Galo Jaime Páez Fajardo et al. “Structural phase transitions of NbO2: Bulk versus surface”. In: *Chemistry of Materials* 33.4 (2021), pp. 1416–1425.

[213] N Ichikuni et al. “Nb K-and L3-edges XAFS study on the structure of supported Nb carbide catalyst”. In: *Journal of Physics: Conference Series*. Vol. 712. 1. IOP Publishing. 2016, p. 012060.

Appendix A

Activity report

1. Conferences and Schools

(a) 28/06/2022-29/06/2022 **Hands-on Software**.
Modena, Italy

(b) 19/09/2022-30/09/2022 **XVI School on Synchrotron Radiation**.
Muggia, Italy

(c) 12/06/2023-16/06/2023 **Ultrafast X-Ray Summer School 2023**.
Hamburg, Germany

(d) 16/06/2024-21/06/2024 **Science@FELs 2024**.
Paris, France
Oral Contribution: *XFEL-based Pump-probe XAS and XES Characterization of Photoexcited States in* CeO_2

2. Teaching activities

(a) 2021-2022 **University teaching assistant** Università degli studi di Modena e Reggio Emilia. 20 hours for "Laboratorio di Fisica 2" of the bachelor degree in Physics

(b) 2022 **University teaching assistant** Università degli studi di Modena e Reggio Emilia. 20 hours for "Laboratorio di Fisica 1" of the bachelor degree in Physics

(c) 2022-2023 **University teaching assistant** Università degli studi di Modena e Reggio Emilia. 20 hours for "Laboratorio di Fisica 2" of the bachelor degree in Physics

(d) 2023 **University teaching assistant** Università degli studi di Modena e Reggio Emilia. 25 hours for "Laboratorio di Fisica 1" of the bachelor degree in Physics

3. Courses and seminars attended

(a) Course "Assessment of the Impact of the Energy transition on the production and market of materials" (M3ES-UNIMORE)

(b) Course "Crystallography sheds light on the fascinating world of perovskites" (M3ES-UNIMORE)

(c) Course "Introduction to experimental Design" (M3ES-UNIMORE)

(d) Course "Scientific communication in English" (e4ac)

(e) Course “Programming with Python” (M3ES- UNIMORE)

(f) Course “Ultrafast spectroscopies applied to functional materials” (PNS-UNIMORE)

(g) Seminar “A study on the surface reactivity of modified CeO_2 ultra-thin films towards H_2 dissociation”. Dott. Avinash Vikatakavi, NANO Colloquia – CNR Nano

(h) Seminar “What is the universe made of?” (Prof. Enrico Bertuzzo), Colloquium dipartimento FIM

(i) Seminar “Solution-processed semiconductor nanostructures for thin-film optoelectronics” (Enrico Della Gaspera), FIM-S3 SEMINAR

(j) Seminar “Dynamic nanophotonics with conducting oxides and metal nitrides: from all-optical switching to new phenomena” (Alexandra Boltasseva), FIM-S3 SEMINAR

(k) Seminar “New Horizons for Nonlinear Space-Time Optics with Near-Zero-Index Materials” (Vladimir M. Shalaev), FIM-S3 SEMINAR

(l) Seminar “Metal-oxide based systems for efficient visible light conversion” (Eleonora Spurio), Nano colloquia

(m) Seminar “Battery Materials Chemistry: New Trends and Perspectives” (Andrea Paolella), FIM-S3 SEMINAR

4. Experience in other laboratories

(a) 08/03/2022-14/03/2022 **Beamtime at APE-HE beamline at Elettra Synchrotron, Trieste**
“In operando NEXAFS study of the correlation between dopant oxidation state and structure in Cu- and Fe-modified CeO2 during H2 dissociation”

(b) 18/02/2023-27/02/2023 **Beamtime at FXE experiment at European XFEL, Schenefeld, Germany**
“Structure and electronic properties of excited states in CeO2”

(c) 10/03/2023-19/06/2023 **Scientific stage activity at the beamline FXE at the European XFEL, Schenefeld, germany**

(d) 12/09/2023-19/09/2023 **Beamtime at SPECIES beamline at MAXIV synchrotron Lund, Sweden**
“Operando combined AP-XPS/FTIR investigation on the catalytic CH4 activation and direct partial oxidation of Cu doped CeO2 thin films at low temperatures”

(e) 27/02/2024-02/03/2024 **Beamtime at FXE experiment at European XFEL, Schenefeld, Germany**
“Structural dynamics of photoinduced polarons in cerium oxide”

(f) 06/05/2024-12/05/2024 **Beamtime at the APE-HE beamline at Elettra synchrotron, Trieste**
“Role of Cu atoms in water splitting on stoichiometric and reduced CeO2 surface”

Appendix B

List of publications

Published

1. S. D'Addato, M. Lanza, A. Boiani, E. Spurio, S. Pelatti, G. Paolicelli, P. Luches.
"Morphology and optical properties of gas phase synthesized plasmonic nanoparticles: Cu and Cu/MgO".
Materials, 15, 4429. (2022) doi: 10.3390/ma15134429

Abstract:*In this paper, an investigation of the properties of Cu and Cu/MgO nanoparticles (NPs) is presented. The NPs were obtained with gas-phase synthesis, and the MgO shells or matrices were formed via the co-deposition method on inert substrates. SEM and AFM were used to investigate the NP morphology on Si/SiOx, quartz, and HOPG. The Cu NPs revealed flattening of their shape, and when they were deposited on HOPG, diffusion and formation of small chains were observed. The embedding of Cu NPs in MgO was confirmed by TEM and EDX maps. XPS showed that Cu was in its metallic state, regardless of the presence of the surrounding MgO. UV–Vis revealed the presence of an intense localized surface plasmon resonance (LSPR) for Cu/MgO and for "bare" NPs. These results confirmed the role of MgO as a protective transparent medium for Cu, and the wavelength position of the LSPR in the Cu/MgO system was consistent with calculations. The wavelength position of the LSPR observed for "bare" and post-oxidized Cu NPs was probably affected by the formation of copper oxide shells after exposure to air. This study paves the way for the use of Cu/MgO NPs as plasmonic nanomaterials in applications such as photovoltaics and sensor technology.*

2. E. Spurio, J. S. Pelli Cresi, G. Ammirati, S. Pelatti, A. Paladini, S. D'Addato, S. Turchini, P. O'Keeffe, D. Catone, P. Luches.
"Injecting Electrons into CeO2 via Photoexcitation of Embedded Au Nanoparticles".
ACS Photonics, 10, 5, 1566–1574. (2023) doi: 10.1021/acsphotonics.3c00184

Abstract:*The electron injection efficiency and the steady state absorptance at different photon energies for a composite system made of Au NPs embedded in a cerium oxide matrix are reported. Cerium oxide can be coupled with plasmonic nanoparticles (NPs) to improve its catalytic properties by visible-light absorption. The present work is a study of the ultrafast dynamics of excited*

states induced by ultraviolet and visible-light excitation in Au NPs combined with cerium oxide, aimed at understanding the excitation pathways. The data, obtained by femtosecond transient absorption spectroscopy, show that the excitation of localized surface plasmon resonances (LSPRs) in the Au NPs leads to an ultrafast injection of electrons into the empty 4f states of the surrounding cerium oxide. Within the first few picoseconds, the injected electrons couple with the lattice distortion forming a polaronic excited state, with similar properties to that formed after direct band gap excitation of the oxide. At subpicosecond delay times, we observed relevant differences in the energetics and the time dynamics as compared to the case of band gap excitation of the oxide. Using different pump energies across the LSPR-related absorption band, the efficiency of the electron injection from the NPs into the oxide was found to be rather high, with a maximum above 30%. The injection efficiency has a different trend in energy as compared to the LSPR-related static optical absorptance, showing a significant decrease in low energies. This behavior is explained considering different deexcitation pathways with variable weight across the LSPR band. The results are important for the design of materials with high overall solar catalytic efficiency.

3. A. Vikatakavi, S. Mauri, M. L. Rivera-Salazar, E. Dobovičnik, S. Pelatti, S. D'Addato, P. Torelli, P. Luches, S. Benedetti.
"Role of Metal Dopants in Hydrogen Dissociation on Cu:CeO2 and Fe:CeO2 Surfaces Studied by Ambient-Pressure X-ray Absorption Spectroscopy".
ACS Appl. Energy Mater., 7, 7, 2746–2754. (2024) doi: 10.1021/acsaem.3c03169

Abstract: *The doping of metal oxides is an interesting route to increase catalyst activity and lower activation temperatures in H_2 dissociation to replace Pt in catalysts for electrochemical devices. In this process, the roles of both the matrix and dopant cations are fundamental to understanding and designing more efficient catalysts. In this work, we have investigated the reduction process in pure and doped CeO_2 films. We followed the oxidation states of Ce and dopants (Cu and Fe) during H_2 exposure at ambient pressure by combining X-ray absorption spectroscopy and gas chromatography on 5 nm films in the temperature range of 300–620 K. We have observed that Cu doping (at concentrations of 5 and 14 at. %) promotes the ceria reduction, while the addition of Fe seems to have a limited impact on the oxide chemical reactivity only at low temperatures. Moreover, thanks to the chemical sensitivity of operando X-ray absorption spectroscopy, we were able to follow simultaneously the evolution of Ce and Cu oxidation states during the reaction, which has permitted to identify two distinct reduction processes taking place above and below 500 K. These measurements show that at low temperatures, the H_2 dissociation takes place at the Cu^{1+} sites, thus explaining the higher reactivity of the Cu-doped samples. The described mechanism can help in the design of Pt-free catalysts with enhanced performances.*

4. E. Spurio, S. Pelatti, S. D'Addato, P. Luches.
"Plasmonic properties and stability of Au and Cu nanoparticles embedded in cerium oxide".
J. Phys.: Condens. Matter 36 375003. (2024) doi: 10.1088/1361-648X/ad5633

Abstract: *With the aim of sensitizing cerium oxide—a very important cat-*

alytic material—to visible light, its coupling with Au and Cu nanoparticles is investigated. The samples are grown by physical synthesis by embedding a layer of nanoparticles between two cerium oxide films. The films are controlled in composition by in-situ x-ray photoemission spectroscopy and in morphology by ex-situ scanning electron microscopy. The optical properties as a function of the oxide thickness, investigated by spectrophotometry in the UV-Vis range, are interpreted based on the results of the morphological characterization and of simulations based on the Maxwell Garnett model. The stability of chemical and optical properties after air exposure is also investigated. The results, indicating that stable materials with tuneable optical properties can be obtained, are important in view of the potential application of the investigated systems in photocatalysis.

Submitted

1. S. Pelatti, S. Benedetti, G. Ammirati, P. O' Keeffe, D. Catone, S. Turchini, X. Huang, Y. Uemura, F. Lima, C. Milne, P. Luches.
   "Niobium oxide films with variable stoichiometry: structure, morphology and ultrafast dynamics".
   Journal of Physical Chemistry C special issue "Francesc Illas and Gianfranco Pacchioni Festschrift".

   Abstract:*Niobium oxide can be stabilized in three distinct stoichiometries, each exhibiting unique physicochemical properties relevant to various technological applications. This study presents a novel procedure for fabricating niobium oxide films and tuning their stoichiometry among the three most stable oxide phases. Starting with a magnetron-sputtered film predominantly composed of Nb_2O_5, its structure and stoichiometry are optimized through thermal treatment in an O_2/N_2 flux. A vacuum reduction treatment transforms the as-grown film into the NbO phase, which can then be re-oxidized under controlled oxygen partial pressure to achieve the NbO_2 phase. The films are characterized in terms of surface composition using X-ray photoemission spectroscopy, structure through X-ray diffraction, optical properties via UV-Vis spectrophotometry, and morphology using scanning electron microscopy. Additionally, we show that X-ray absorption near-edge spectroscopy at the Nb K-edge, performed with X-ray free-electron laser radiation, can provide insights into the electronic structure and subsurface stoichiometry of the films. The ultrafast mechanisms underlying photo-induced processes in NbO_2 are also discussed.*

In preparation

1. E. Spurio, S. Mauri, S. Pelatti, S. Benedetti, M. Rivera, S. D'Addato, P. Torelli, P. Luches, S. Benedetti.
   "Role of Cu atoms in water splitting on CeO_2 surface studied by Ambient-Pressure X-ray Absorption Spectroscopy" (tentative title).

2. S. Pelatti, E. Spurio, D. Catone, P. O'Keeffe, S. Turchini, G. Ammirati, S. Benedetti, A. di Bona, S. D'Addato, Y. Jiang, P. Zalden, Y. Uemura, H.

Wang, D. Vinci, X. Huang, F. Lima, M. Biednov, D. Khakhulin, C. Milne, F. Boscherini, P. Luches “ Ultrafast dynamics of photoinduced polaron formation in cerium oxide”.